Cell Reports

Resource

Proximity proteomics reveals UCH-L1 as an essential regulator of NLRP3-mediated IL-1β production in human macrophages and microglia

Graphical abstract

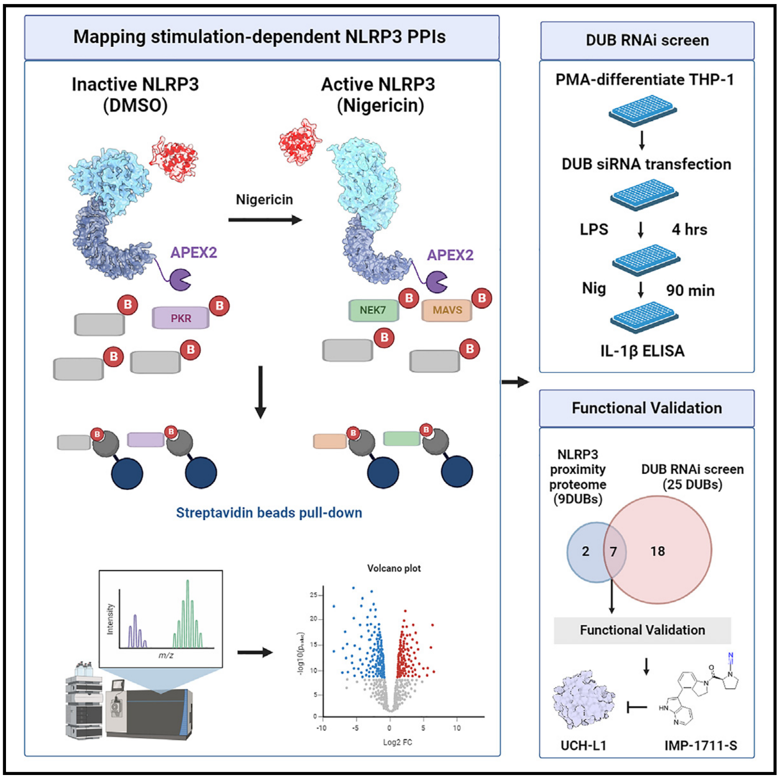

Highlights

- NLRP3-APEX2 proximity labeling combined with DUB siRNA screen as a discovery approach
- UCH-L1 interacts with the NACHT domain of NLRP3
- UCH-L1 chemical inhibition and deletion interfere with NLRP3 assembly and IL-1β production

Authors

Zhu Liang, Andreas Damianou, Iolanda Vendrell, ..., Edward W. Tate, Elena Di Daniel, Benedikt M. Kessler

Correspondence

zhu.liang@ndm.ox.ac.uk (Z.L.),
benedikt.kessler@ndm.ox.ac.uk (B.M.K.)

In brief

Liang et al. used the APEX2-based proximity labeling (APEX2 PL) approach to profile the NLRP3 inflammasome activation dynamics upon nigericin stimulation. Combined with affinity purification and RNAi screening, they discover UCH-L1 as a modulator of NLRP3 inflammasome assembly and IL-1β production.

Liang et al., 2024, Cell Reports *43*, 114152
May 28, 2024 © 2024 The Authors. Published by Elsevier Inc.
https://doi.org/10.1016/j.celrep.2024.114152

Cell Reports

CellPress
OPEN ACCESS

Resource

Proximity proteomics reveals UCH-L1 as an essential regulator of NLRP3-mediated IL-1β production in human macrophages and microglia

Zhu Liang,[1,2,12,*] Andreas Damianou,[1,2,12] Iolanda Vendrell,[1,2] Edward Jenkins,[3] Frederik H. Lassen,[4] Sam J. Washer,[5,6] Athina Grigoriou,[1,2] Guihai Liu,[1] Gangshun Yi,[7] Hantao Lou,[8] Fangyuan Cao,[9] Xiaonan Zheng,[1] Ricardo A. Fernandes,[1] Tao Dong,[1] Edward W. Tate,[9] Elena Di Daniel,[10,11] and Benedikt M. Kessler[1,2,13,*]

[1]Chinese Academy for Medical Sciences Oxford Institute, Nuffield Department of Medicine, University of Oxford, Roosevelt Drive, Oxford OX3 7FZ, UK
[2]Target Discovery Institute, Centre for Medicines Discovery, Nuffield Department of Medicine, University of Oxford, Roosevelt Drive, Oxford OX3 7FZ, UK
[3]Kennedy Institute of Rheumatology, University of Oxford, Oxford OX3 7FY, UK
[4]Big Data Institute, Li Ka Shing Centre for Health Information and Discovery, Nuffield Department of Medicine, University of Oxford, Old Road Campus, Oxford OX3 7LF, UK
[5]James and Lillian Martin Centre for Stem Cell Research, Sir William Dunn School of Pathology, University of Oxford, South Parks Road, Oxford OX1 3RE, UK
[6]Wellcome Centre for Human Genetics, Nuffield Department of Medicine, University of Oxford, Oxford OX3 7BN, UK
[7]Division of Structural Biology, Wellcome Trust Centre for Human Genetics, University of Oxford, Oxford OX3 7BN, UK
[8]Ludwig Institute for Cancer Research, University of Oxford, Oxford, UK
[9]Department of Chemistry, Molecular Sciences Research Hub, Imperial College London, London W12 0BZ, UK
[10]Alzheimer's Research UK Oxford Drug Discovery Institute, University of Oxford, Oxford OX3 7FZ, UK
[11]Present address: Astex Pharmaceuticals, 436 Cambridge Science Park, Milton Rd., Milton, Cambridge CB4 0QA, UK
[12]These authors contributed equally
[13]Lead contact
*Correspondence: zhu.liang@ndm.ox.ac.uk (Z.L.), benedikt.kessler@ndm.ox.ac.uk (B.M.K.)

https://doi.org/10.1016/j.celrep.2024.114152

SUMMARY

Activation of the NACHT, LRR, and PYD domains-containing protein 3 (NLRP3) inflammasome complex is an essential innate immune signaling mechanism. To reveal how human NLRP3 inflammasome assembly and activation are controlled, in particular by components of the ubiquitin system, proximity labeling, affinity purification, and RNAi screening approaches were performed. Our study provides an intricate time-resolved molecular map of different phases of NLRP3 inflammasome activation. Also, we show that ubiquitin C-terminal hydrolase 1 (UCH-L1) interacts with the NACHT domain of NLRP3. Downregulation of UCH-L1 decreases pro-interleukin-1β (IL-1β) levels. UCH-L1 chemical inhibition with small molecules interfered with NLRP3 puncta formation and ASC oligomerization, leading to altered IL-1β cleavage and secretion, particularly in microglia cells, which exhibited elevated UCH-L1 expression as compared to monocytes/macrophages. Altogether, we profiled NLRP3 inflammasome activation dynamics and highlight UCH-L1 as an important modulator of NLRP3-mediated IL-1β production, suggesting that a pharmacological inhibitor of UCH-L1 may decrease inflammation-associated pathologies.

INTRODUCTION

Innate immunity reflects a cornerstone of defense systems in living organisms that integrates with adaptive immune responses in the case of higher eukaryotes.[1] A major hallmark is the activation of inflammasome complexes, composed of ASC and nucleotide-binding oligomerization domain (NOD)-like receptors (NLRs), such as NACHT, LRR, and PYD domains-containing protein 3 (NLRP3),[2] involving cleavage of pro-interleukin-1β (IL-1β) by caspase-1 [3]. External stimuli, including lipopolysaccharide (LPS) as the first and nigericin, monosodium urate (MSU) monohydrate, alum, ATP, or cholesterol crystals as the second signal lead to the assembly and activation of the NLRP3 inflammasome complex, resulting in inflammatory responses.[4,5] Assembly of this supramolecular structure, featuring NLRP3 and ASC, is further regulated by associated factors, such as NEK7,[6] as well as multiple posttranslational modifications, including phosphorylation and ubiquitylation.[7–9] Particularly, the ubiquitin conjugation machinery has been emerging as a central modulator for NLRP3 itself and other inflammasome components via proteasomal or lysosomal degradation or by modulating protein-protein interactions. Ubiquitylation/deubiquitylation-dependent

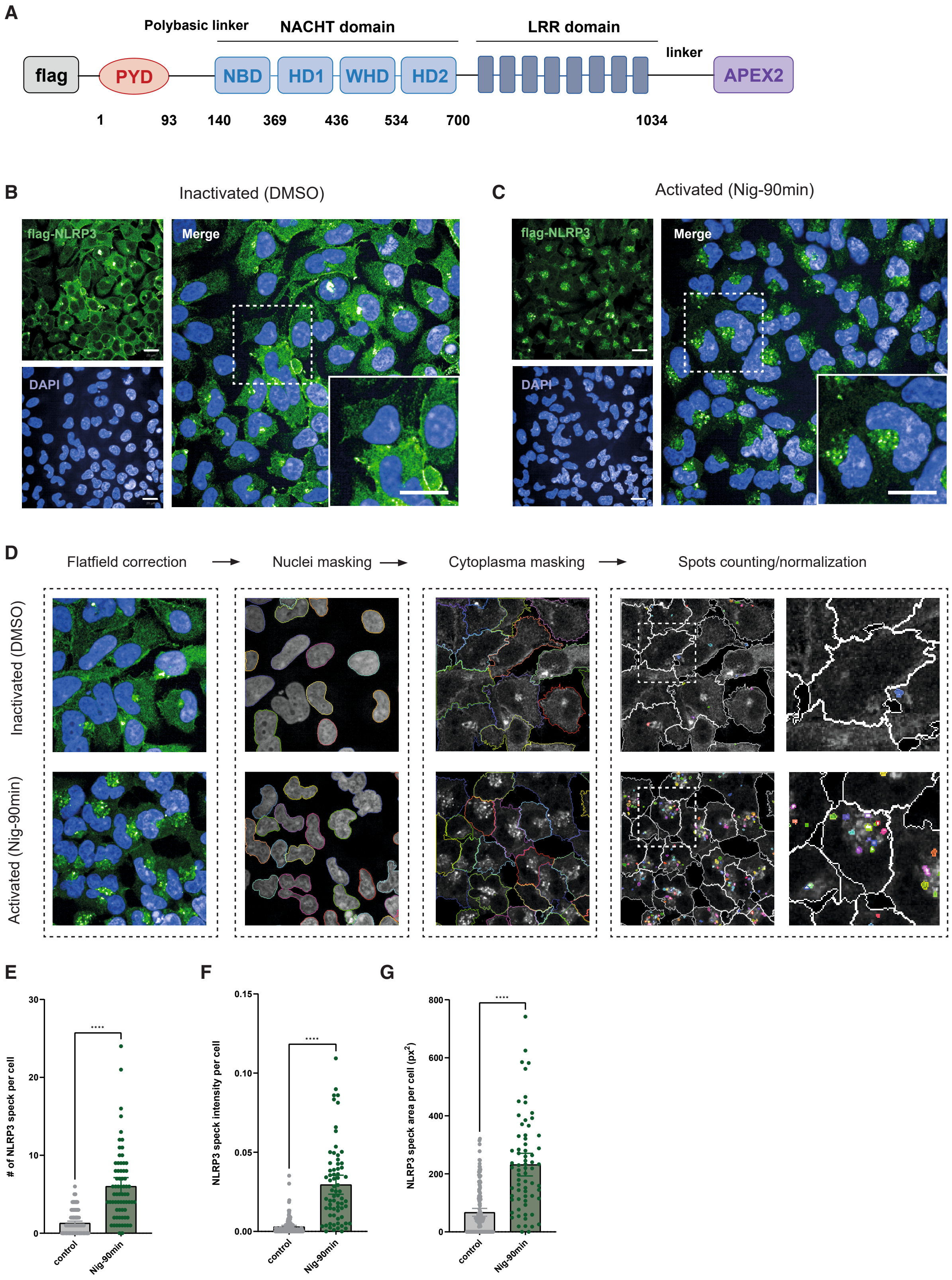

(legend on next page)

steps have been implicated in multiple phases of inflammasome priming and activation.[10] In addition to E1-E2-E3 enzymes, including TRIM31,[11] gp78/Insig-1.[12] MARCH7,[13] HUWE1,[14] and RNF25 and Cbl,[15] deubiquitylases (DUBs) also contribute to its turnover and higher-order assembly.[10,16,17] More specifically, ubiquitin protease 7 (USP7) and USP47 inhibition resulted in reduced inflammasome activation.[18] In addition, in mice, BRCC3, a DUB reflecting a component of the BRCC3 isopeptidase complex (BRISC), has been shown to deubiquitylate NLRP3, thereby regulating inflammasome activity.[19] Recently, increasing numbers of findings suggest a complex interplay between ubiquitylation and deubiquitylation mechanisms that modify components of the inflammasome complex. However, most studies of ubiquitin-mediated NLRP3 pathway were conducted in murine models, such as NG5, mouse peritoneal macrophages, and mouse bone marrow-derived macrophages (BMDMs).[19–21] Given the inter-species divergence between the human and mouse inflammasome regulatory mechanism, the role of ubiquitylation/deubiquitylation in human NLRP3 inflammasome activation remains largely unknown.

To gain a more comprehensive understanding of the ubiquitin-mediated regulation of the human NLRP3 inflammasome, we combined ascorbic acid peroxidase 2 (APEX2)-based proximity labeling, affinity purification, and RNAi screening to discover molecular factors involved in the primary and secondary signals of NLRP3 inflammasome activation and assembly. In both a reconstituted system and macrophages, we demonstrate that ubiquitin C-terminal hydrolase 1 (UCH-L1) interacts with the NACHT domain of NLRP3 and thereby interferes with ASC and NLRP3 assembly. Furthermore, UCH-L1 knockdown or chemical inhibition interferes with IL-1β production, particularly in microglia cells that exhibited elevated UCH-L1 expression as compared to peripheral monocytes or macrophages.

RESULTS

NLRP3-APEX2 captures the NLRP3 molecular proximity network

As the N terminus NLRP3 PYD domain has been reported to be responsible for initiating NLRP3 oligomerization, we inserted APEX2 at the C terminus (LRR domain) of NLRP3, including a flexible linker between these domains and a FLAG epitope at the N terminus (Figure 1A). To avoid unstable expression and mis-localization during transient transfection, we generated a NLRP3-APEX2 HEK293 stable cell line using the Flp-In T-REx system, allowing dose-dependent control of expression with tetracycline (Figures S1A and S1B). Fluorescence microscopy confirmed that both FLAG-NLRP3 and FLAG-NLRP3-APEX2 can form puncta in the perinuclear areas in response to nigericin stimulation, while the fusion proteins are diffused across the cytosol in the resting state (Figures 1B, 1C, S1C, and S1D). Quantitative analysis shows no morphological alterations between NLRP3 and NLRP3-APEX2 speck formation (Figures 1D–1G and S1E–S1H; Table S4). Furthermore, ASC oligomerization assays with co-expression of the adaptor protein ASC in stable cell lines proved that both FLAG-NLRP3 and FLAG-NLRP3-APEX2 are competent to recruit ASC and induce its polymerization upon stimulation with nigericin (Figures S2A and S2B). Taken together, these results indicate that APEX2 tagging fused to the C terminus of NLRP3 does not impede its ability to sense stimuli, particularly nigericin-induced potassium efflux, and recruit ASC to form oligomers.

We next investigated whether biotin labeling profiles are spatially restricted to the fusion bait. Live HEK293 cells expressing NLRP3-APEX2 were treated with or without nigericin. Subsequently, cells were treated with H_2O_2 in the presence of biotin-phenol, followed by rapid quenching, methanol fixation, and staining (Figure 2A). In contrast to the native control without H_2O_2 treatment, we observed robust biotinylation by streptavidin-Alexa Fluor 488 imaging. Under unstimulated conditions, NLRP3-APEX2 was diffused across the cytosol, with biotinylated proteins following a similar distribution pattern. Upon nigericin treatment, NLRP3-APEX2 oligomerized to form puncta close to the nucleus, and we also observed specks formed by biotin-labeled proteins (Figure 2B). This partially suggests the spatial specificity of NLRP3-APEX2-induced biotinylation.

The ability of APEX2 to efficiently label and capture the NLPR3 "proximitome" was assessed using streptavidin immunoblotting and Coomassie blue staining, confirming the robust biotin labeling activity of APEX2 fused to NLRP3 (Figures 2C and S3B). Initially, we investigated whether APEX2 is competent to capture the known NLRP3-interacting protein NIMA-related kinase 7 (NEK7). In contrast to the unlabeled negative control, we found that NLRP3-APEX2 specifically biotinylated NEK7. Additionally, a substantial increase in NEK7 protein sequestration was observed in association with activated NLRP3 (Figure 2C).

Given the rapid kinetic properties of APEX2 proximity labeling, we next sought to map the spatiotemporally resolved "proximitome" of NLRP3 upon stimulation by nigericin across various time intervals. Following mass spectrometry analysis, 3,478 proteins in total were detected across the DMSO control and nigericin treatment for 30 min, 60 min, and 90 min. To maximize the signal-to-noise ratio and discriminate the *bona fide* interacting partners from the background contaminants, the Bayesian model-based algorithm significance analysis of interactome (SAINTexpress)[24] was applied, yielding 800–1,100 NLRP3 proximal proteins (Figures 3A, 3B, and S3A). Unsupervised principal-component analysis (PCA) showed the clustering and patterns of

Figure 1. Quantitative analysis of NLRP3 puncta formation upon nigericin (Nig) stimulation

(A) Scheme of APEX2-tagging NLRP3. APEX2 was fused to the C terminus of full-length NLRP3 via a glycine-serine linker.

(B and C) Representative confocal images of FLAG-NLRP3-APEX2-expressing HEK293 stable cell lines treated with DMSO (B) or 10 μM nigericin (C) for 90 min. Cells were stained with an anti-FLAG antibody (green) and DAPI (blue). Scale bars, 10 μm.

(D) Image processing pipeline of NLRP3 puncta detection and quantitative analysis. Confocal images were first flat field corrected, followed by the segmentation of nuclei and cytoplasm. NLRP3 puncta were identified, counted, and analyzed using the Columbus Image Data Analysis System. Scale bars, 10 μm.

(E–G) Quantification of NLRP3 puncta per cell in FLAG-NLRP3-APEX2-expressing HEK293 stable cell lines treated with DMSO ($n = 141$) or 10 μM nigericin ($n = 69$) for 90 min. Error bars show the standard deviation of the mean. ****$p < 0.0001$ (unpaired two-sided t test).

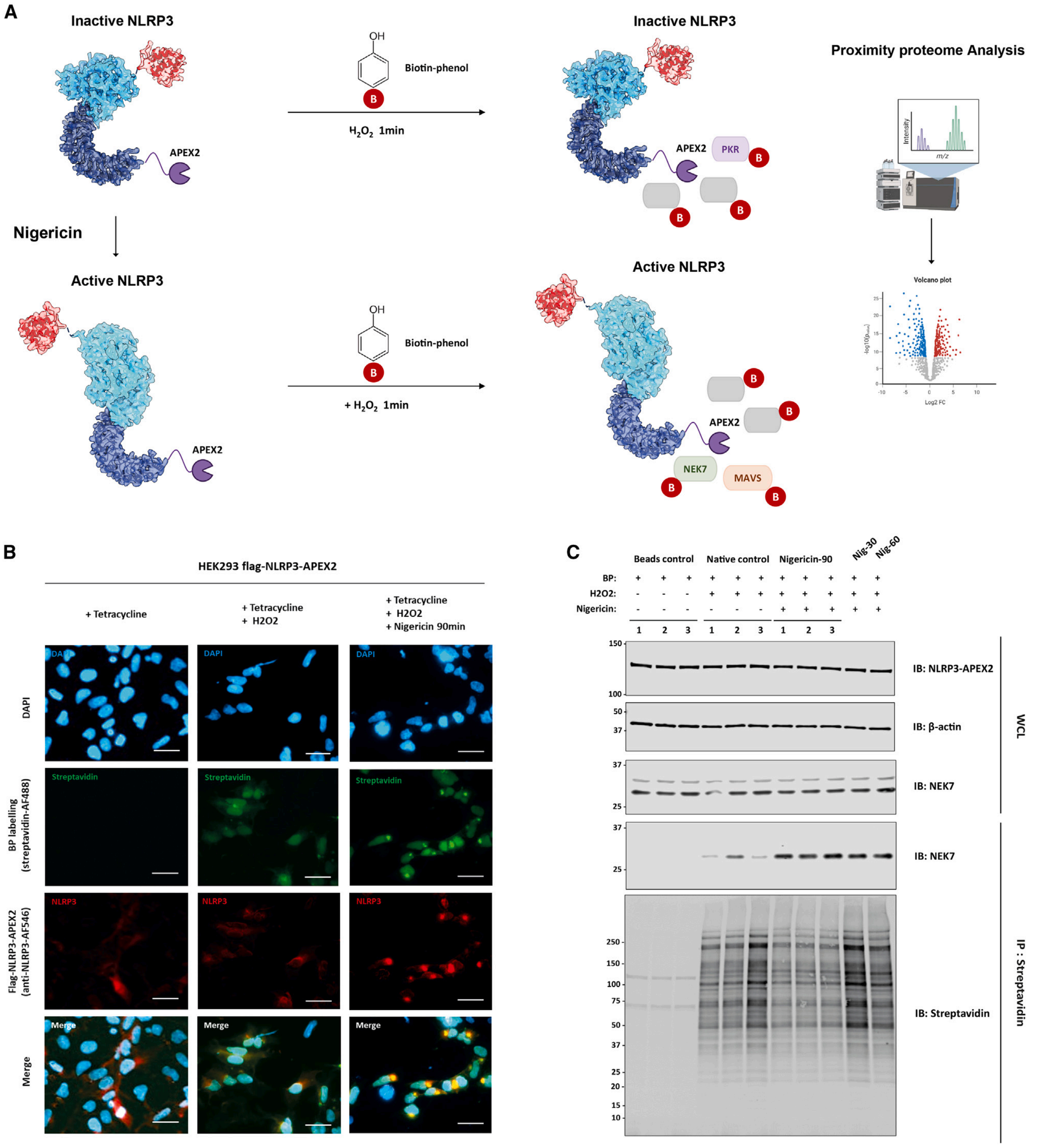

Figure 2. Proximity proteomics profiling of the NLRP3 inflammasome upon activation

(A) PL and MS analysis workflow for inactive (PDB: 6NPY) and active NLRP3 (PDB: 8EJ4).[22,23]

(B) Confocal fluorescence imaging of NLRP3 APEX2 labeling in HEK293 cell lines. NLRP3-APEX2 HEK293 stable cell lines were treated with tetracycline overnight, followed by treatment with nigericin (10 μM) or DMSO (control) for 90 min. Subsequently, cells were incubated with biotin phenol, followed by H_2O_2 as indicated. Afterward, cells were fixed and stained with streptavidin-Alexa Fluor 488 (AF488) conjugate to visualize biotinylated proteins and anti-NLRP3 antibody to visualize the localization of NLRP3-APEX2. BP, biotinylated protein. Scale bars, 50 μm.

(C) Immunoblot showing the biotinylated NEK7 captured by streptavidin beads in negative control, unstimulated, and nigericin-stimulated HEK293 Flp-In T-REx NLRP3-APEX2 cells. Cells were treated with tetracycline overnight and stimulated with nigericin for 30 min, 60 min, and 90 min before the APEX2 labeling. Whole-cell lysates and streptavidin pull-down were collected and blotted for NLRP3 and NEK7.

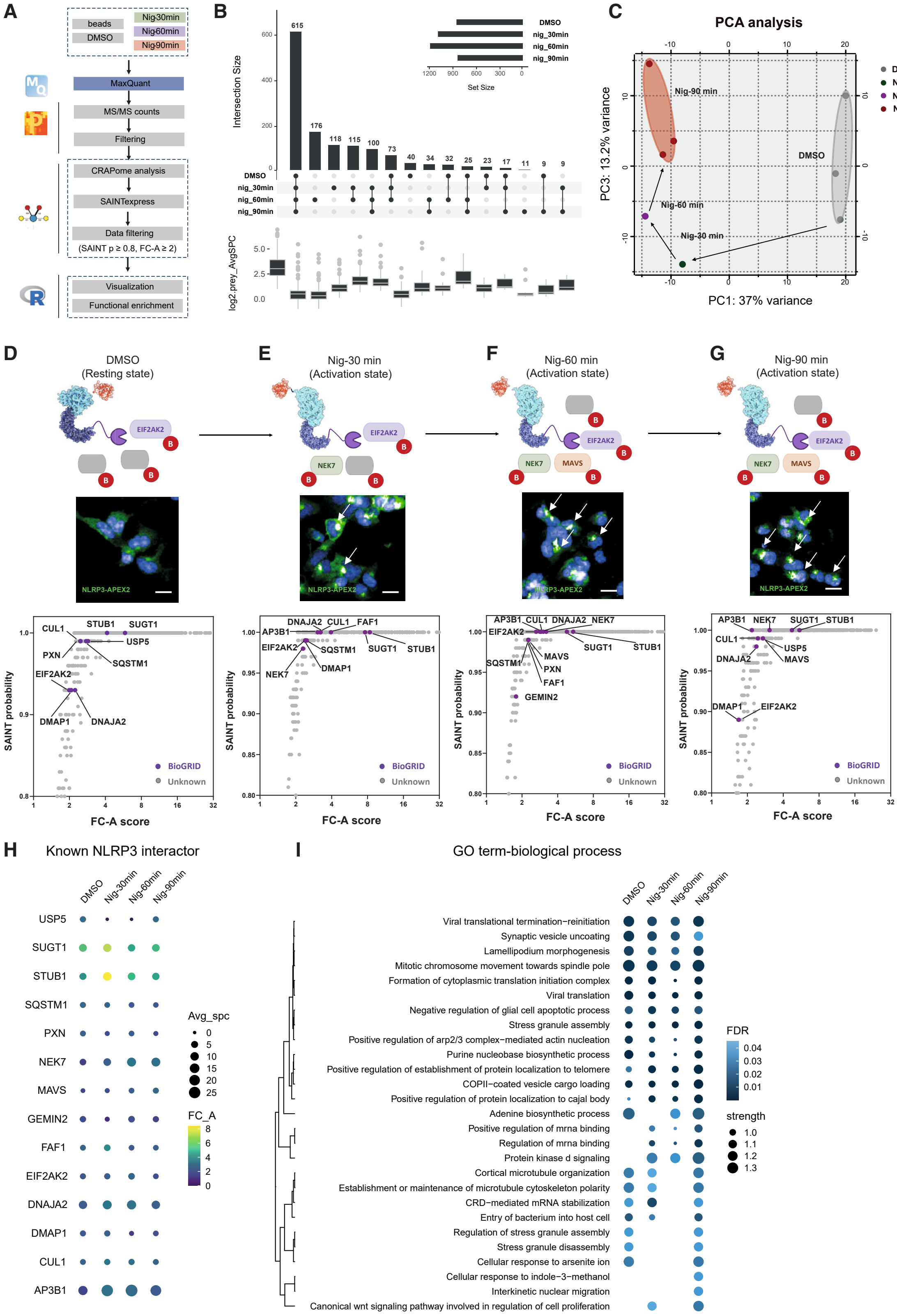

(legend on next page)

different protein subgroups (Figure 3C). A high correlation was observed between the three biological repeats within each group, confirming the low technical variation in this experiment (Figure S3C).

To assess the specificity of the NLRP3 proximity proteome, we next sought to check whether the known NLRP3 interactors or regulators are biotinylated and captured by APEX2. The SAINT probability scoring and simpler fold change (FC) were calculated by the comparison of prey protein abundance between the bait and negative bead control. Previously reported 83 human NLRP3 interactors, retrieved from the public interaction repository BioGRID (https://thebiogrid.org/, v.4.4.209) and the literature (Table S1),[25–27] were mapped and plotted with stringent thresholds [SAINT probability > 0.8, primary fold change score (FC-A) ≥ 1]. After filtering, 18 known NLRP3 interactors (35%) were discerned as high-confidence hits within the proximal proteomics data (Figures 3D–3H and S4), confirming the enrichment of NLRP3-associated proteins.

Temporal tracking of the NLRP3 proximity proteome

To gain mechanistic and functional insights into the NLRP3 proximity proteome following nigericin stimulation at various intervals, we conducted a Gene Ontology term-biological process (GOBP) enrichment analysis (Figure 3I). 13 shared terms, including viral translation, apoptotic cell death regulation, stress granule assembly, and mitosis-associated processes, were significantly enriched across all four groups. In contrast to the unstimulated control, pathways related to "protein kinase D signaling" and "mRNA binding regulation" were uniquely present after nigericin exposure, consistent with prior observations.[28] Intriguingly, the enrichment of "cellular response to arsenite ion" and "regulation of stress granule disassembly" terms suggest a potential functional association between inflammasome and stress granule formation. This connection was substantiated by previous reports of the stress granule protein DDX3X as a pivotal mediator, modulating between apoptotic ASC speck formation and pro-survival stress signaling.[29,30] In terms of GO term-molecular function (GOMF) enrichment analysis, "GTP-dependent protein binding" and "1-phosphatidylinostitol binding" were significantly enriched solely in the nigericin-60 min and nigericin-90 min groups, suggesting that nigericin treatment might induce the recruitment of proteins associated with the above two biological functions (Figures S5A–S5C). GO term-cellular component (GOCC) analysis identified 16 common subcellular compartments or complexes, including coat protein complex II (COPII) vesicle coat, endosomal sorting complex required for transport-0 (ESCRT-0) complex, and chaperone complex. Notably, three endocytic recycling-associated complexes, including the endosome-associated recycling protein (EARP) complex, endosome-to-plasma transport vesicle, and Golgi-associated retrograde protein (GARP) complex, were significantly enriched solely in the nigericin-60 min and nigericn-90 min groups, suggesting that the NLRP3 complex may translocate to the *trans*-Golgi network (TGN) or endosome upon stimulation (Figure S5D). Similarly, the compartment enrichment analysis identified another four complexes (Dcp1-Dcp2, signal recognition receptor, MAD1, and the cohesin I complex) that were only captured and enriched at the last two time points of nigericin treatment (Figures S6A–S6E). We also performed tissue enrichment analysis, and not surprisingly, poor tissue specificity was observed in either the unstimulated or stimulated group (Figure S5E). To further explore the physiological and pathological biological processes, a Reactome pathway analysis was performed on the proximity proteome. The top 20 significantly enriched pathways are shown in Figure S6F. Notably, several innate immunity- and virus infection-associated pathways, such as IL-6 signaling, major histocompatibility complex (MHC) class I, and PP2A-mediated dephosphorylation of key metabolic factors, were identified and enriched. Selected gene sets involved in the above pathways are plotted in Figures S6G and S6H.

Localization analysis reveals translocation of NLRP3 upon stimulation

As the subcellular relocalization of NLRP3 and its underlying mechanism remain controversial,[31] we performed a localization analysis to assess the spatial properties of the NLRP3 inflammasome during complex assembly. After filtering, normalization, and imputation, we compared the relative abundance of biotinylated proteins in the unstimulated (DMSO) and stimulated states (nigericin-90 min). The resulting volcano plot (Figure S3F) shows 103 proteins enriched in the right quadrant for the stimulated state and 104 proteins enriched in the left quadrant for the resting state, with a relatively stringent cutoff for FC and false discovery rate ($\log2[FC] \geq 0.5$ or ≤ -0.5, false discovery rate [FDR] ≤ 0.05). GO term-CC enrichment analysis was performed on the differentially enriched proteins under either

Figure 3. Temporal tracking of the NLRP3 proximity proteome

(A) Schematic of the data analysis for APEX2 PL-MS.

(B) Upset plot depicting the intersections of high-confidence NLRP3 proximal proteins across samples. The bars in the y axis represent the number of high confidence proximal proteins (SAINT probability score ≥ 0.8, FC-A ≥ 1) identified in each sample. The boxplot represents the log2 (average of spectral counts) of the proximal proteins identified in each group. The median and first and third quartiles of the data are displayed as the center line and the lower and upper boundaries.

(C) PCA of the 8 samples (3 unstimulated DMSO controls, 3 stimulated samples with 90-min treatment of nigericin, 30-min nigericin-stimulated samples, and 60-min nigericin-stimulated samples). Each dot represents an individual sample.

(D–G) SAINT probability scoring of the proteomics data for NLRP3-APEX2 compared to the negative bead control. Proteins passing the cutoff (SAINT probability score ≥ 0.8 and FC-A score ≥ 1) are considered high-confidence proximal proteins for NLRP3. Previously reported NLRP3-interacting proteins (BioGRID, v.4.4.213) are colored purple. All other proteins are shown in gray. Inactive (PDB: 6NPY) and active NLRP3 (PDB: 8EJ4) are shown as surface view with a model.

(H) Dot plot of previously reported NLRP3-interacting proteins that are detected in the NLRP3-APEX2 proximitome upon nigericin stimulation for different times (unstimulated, 30 min, 60 min, and 90 min). Sizes denote the average spectral counts, and colors denote the FC-A score.

(I) Dot plots displaying the GOBP enrichment analysis of high-confidence NLRP3 proximal proteins upon nigericin stimulation for different times as indicated.

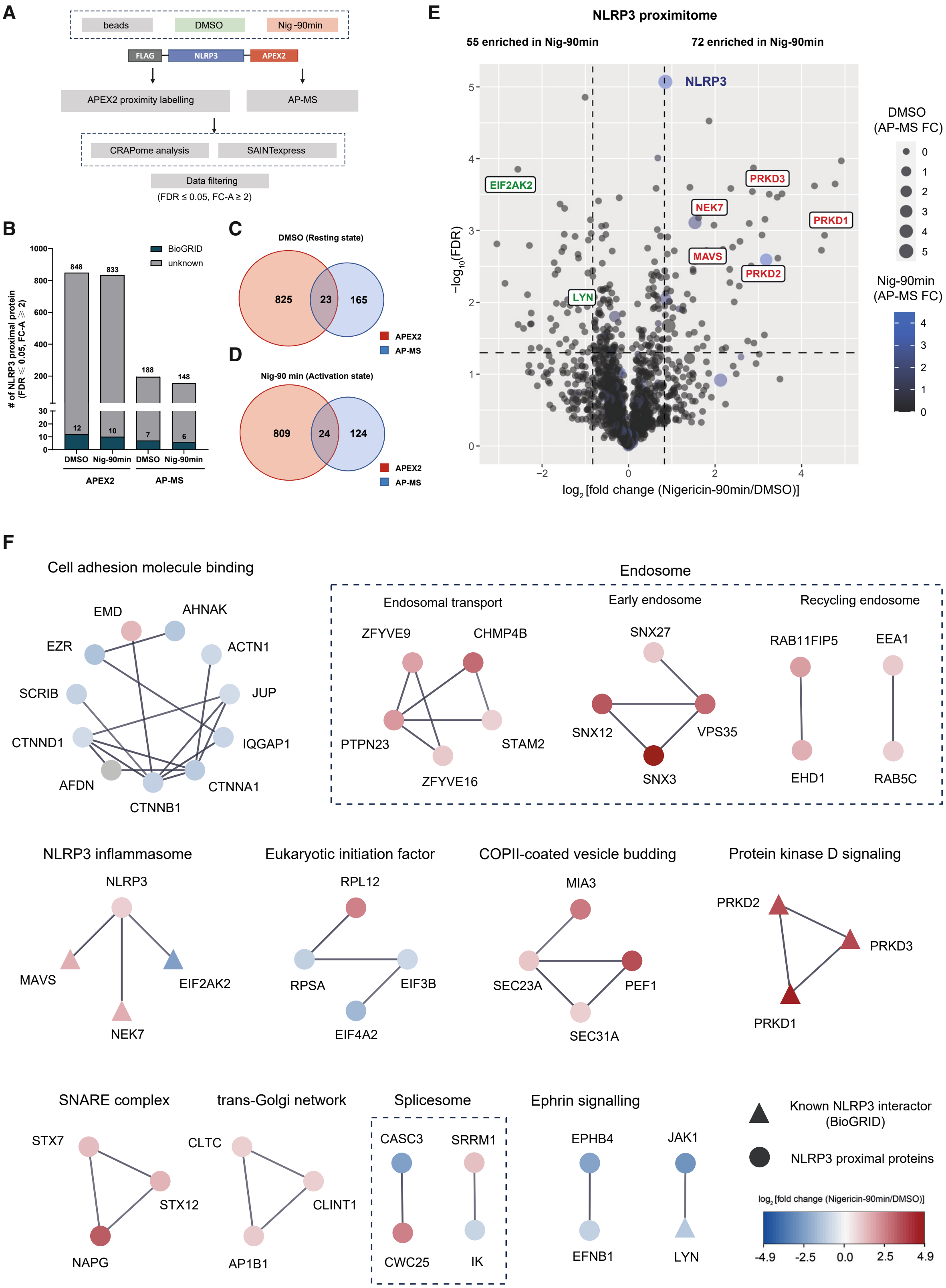

(legend on next page)

condition. The proximity proteome under stimulated condition showed high spatial specificity for the Golgi apparatus, with 24 proteins falling into the GO-CC term category ‘‘Golgi membranes’’ (Figures S3D–S3F; Table S2). This is consistent with the previous observation that NLRP3 is activated and recruited to dispersed TGN (dTGN) in response to diverse stimuli.[32,33]

Mapping stimulation-dependent NLRP3 interaction alterations using APEX2-PL and AP-MS

Modulation of the NLRP3 local milieu during the activation process was further examined using an integrated approach that combined APEX2 proximity labeling (PL) and affinity purification-mass spectrometry (AP-MS) (Figure 4A). For APEX2 PL-MS, the SAINTexpress analysis identified 848 (DMSO) and 833 (Nig-90 min) proximal proteins, while 188 (DMSO) and 148 (Nig-90 min) potential interacting proteins were captured using the AP-MS method (Figures 4A, 4B, and S7A–S7E). There was a relatively small number of overlapping proteins between PL-MS and AP-MS, possibly as a result of the complementary nature of these two techniques (Figures 4C and 4D) and consistent with the previous comparison between BioID and AP-MS.[34]

Additionally, we sought to compare the NLRP3 proximal proteome under resting and activation states. Stimulation-dependent NLRP3 interactors are expected to be differentially biotinylated upon nigericin treatment. To denoise the proximity proteome, we used receiver operating characteristic (ROC) analysis to determine the cutoff (Figure S8A). Based on the ROC analysis, the cutoff was set where the TPR (true positive rate)-FPR (false positive rate) was maximal (Figures S8B and S8C), and we obtained 72 NLRP3-associated proteins under the activated condition and 55 under the resting condition. Notably, seven known NLRP3-interacting proteins were differentially enriched. Of these, five (NEK7, MAVS, PRKD1, PRKD2, and PRKD3, highlighted in red) enriched in the right quadrant are established positive regulators of NLRP3, while EIF2AK2 and LYN (highlighted in green) in the left quadrant are previously characterized inhibitory mediators. Interestingly, we noticed increased labeling and capture of NLRP3 under activated conditions, likely due to oligomerization (Figure 4E).

To gain a visual understanding of the stimulation-dependent interaction networks and infer related biological insights, we performed a PPI network analysis (Figure 4F). As for the nigericin-stimulated condition, we identified protein complexes including the NLRP3 inflammasome (NEK7 and MAVS), the soluble N-ethylmaleimide-sensitive factor attachment protein receptor (SNARE) complex, COPII vesicle coat, *trans*-Golgi network (TGN) and the protein kinase D signaling complex. In the unstimulated state, complexes including the cell adhesion molecules, translational initiation factor, Ephrin signaling, and the Janus kinase (JAK)–signal transducer and activator of transcription (STAT) pathway were significantly enriched (Figure 4F).

NLRP3-associated DUBs identified by proximity proteome-guided RNAi screening

The proximity proteome enabled us to capture several ubiquitin system components, including 18 DUBs in total (USP9X, USP8, USP5, USP47, USP32, USP24, USP19, USP15, USP14, USP10, USP1, UCH-L1, PAN2, OTULIN, OTUID4, OTUB1, EIF3H, and CYLD), that passed the stringent filtering criteria (SAINT probability > 0.8, FC-A $\geq$ 1). Among the 18 enriched DUBs, 9 were consistently present in all four groups, and no marked difference was noted between the stimulated and unstimulated states (Figures 5A–5E). To complement this, we carried out a DUB library RNAi screen in phorbol 12-myristate 13-acetate (PMA)-differentiated THP-1 cells, aiming to assess their influence on NLRP3 inflammasome priming and activation, reflected by IL-1β production. In total, knockdown of 25 DUBs (outliers that surpass mean ± 1 standard deviation, Z score $\geq$ 1 or $\leq$ -1; Table S3) was found to alter IL-1β levels in THP-1 cells treated with LPS or LPS/nigericin (Figures 5F and 5G). A combination of proximity proteomics and RNAi screening revealed 7 DUBs showing effects in both assays (USP9X, USP8, USP14, USP10, UCH-L1, OTUB1, and OTUD4) (Figure 5H). USP9X, USP14, and OTUB1 have already been reported to modulate the NLRP3 inflammasome,[35,36] suggesting additional NLRP3-associated DUBs (USP8, USP10, OTUD4, and UCH-L1).

UCH-L1 interacts with the NACHT domain of NLRP3 and affects IL-1β production

Among these DUBs, UCH-L1 consistently affected IL-1β levels and showed high NLRP3 proximity scores. Notably, the knockdown of UCH-L1 did not alter pro-IL-1β mRNA expression, while it decreased protein levels and production of the mature form in THP-1 monocytes (Figures 5I and 5J) and human peripheral blood mononuclear cells (PBMCs) (Figures 5K and 5L). Expression of IL-6 and tumor necrosis factor alpha (TNF-α) was also slightly suppressed in the absence of UCH-L1 (Figures S9B and S9C), indicating that UCH-L1 might also play a role in the nuclear factor κB (NF-κB)-regulated priming stage. As UCH-L1 is highly abundant in cells associated with the CNS, we sought to investigate its role in brain-resident immune cells, such as microglia, which also express NLRP3 inflammasome components (Figure S10). Similarly to THP-1 cells and PBMCs, UCH-L1

Figure 4. Mapping stimulation-dependent NLRP3 protein-protein interaction (PPI) alterations using APEX2-PL and AP-MS

(A) Schematic of the integrated approach combining APEX2 PL and AP-MS.

(B) The number of known (BioGRID, blue) and newly discovered NLRP3-interacting proteins (gray) from APEX2 PL or AP-MS.

(C and D) Venn diagrams showing the number of NLRP3 proximal proteins identified in APEX2 PL or AP-MS.

(E) Volcano plot depicting the FC for relative protein quantification of NLRP3-APEX2 PL samples between unstimulated (DMSO) and stimulated conditions (Nig-90 min). Data are shown as means of three independent samples. Non-adjusted unpaired two-tailed t test was applied to the statistical analysis. Sizes denote the SAINT probability score for AP-MS during stimulation (Nig-90 min), and colors reflect the score in its unstimulated condition.

(F) Protein-protein interaction network for NLRP3-APEX2 PL proteins enriched after stimulation with nigericin (red) or unstimulated as control (blue). The Markov clustering (MCL) algorithm was performed with the PPI scores from the STRING database (confidence score threshold = 0.7). Gray lines denote the protein-protein interaction curated from the Reactome, CORUM, and IntAct databases. Cluster labels were added manually. n = 3 biological replicates.

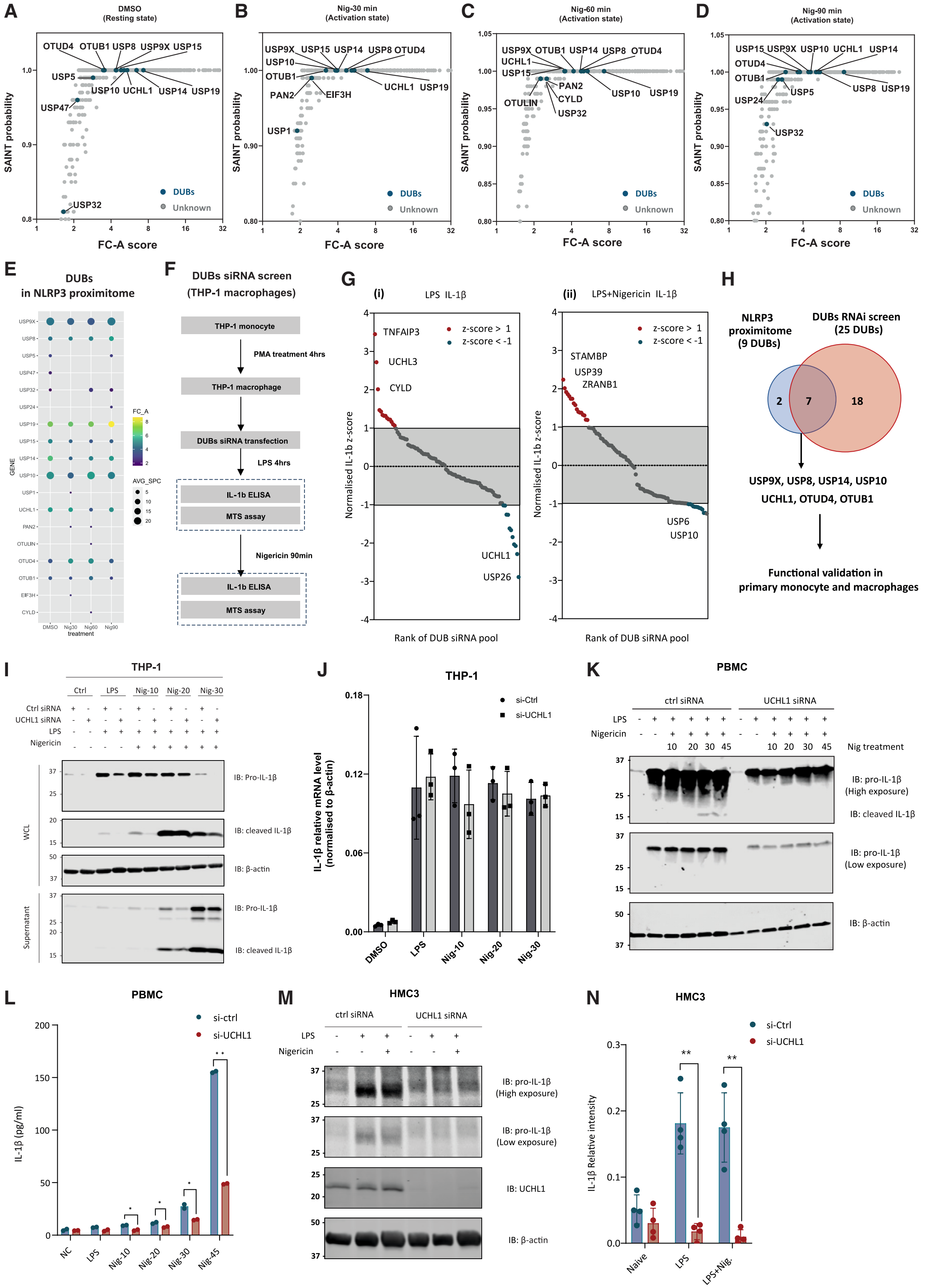

(legend on next page)

deficiency markedly suppressed IL-1β production in the human microglial cell line HMC3 (Figures 5M and 5N).

NLRP3-UCH-L1 association was identified through NLRP3-APEX2 PL (Figure 6A) and confirmed by immunoprecipitation in HEK293T (Figure 6B) and BV2 microglia cells (Figure 6C). Notably, levels of association between NLRP3 and UCH-L1 decrease upon nigericin stimulation (Figure 6B). To further determine which domain within NLRP3 interacts with UCH-L1, we overexpressed FLAG-tagged full-length and truncated NLRP3 in HEK293T cells. UCH-L1 interacted with the full-length NLRP3 and NACHT domain of NLRP3 (Figures 6D and 6E). These results imply that the NACHT domain of NLRP3 directly or indirectly provides a binding site for UCH-L1. Additionally, immunofluorescence revealed the colocalization of NLRP3 with UCH-L1 in human induced pluripotent stem cell (hiPSC)-derived microglial cells (Figures 6F and 6G).

UCH-L1 catalytic inhibition abrogates ASC assembly, NLRP3 inflammasome activation, and IL-1β processing

To investigate how UCH-L1 modulates IL-1β processing and release, we selected a potent inhibitor, IMP-1711-S (small molecule 27 in patent[37]; Figure 7A),[38,39] and tested its effect on NLRP3 inflammasome activation in THP-1 cells, human PBMCs, and hiPSC-derived microglial cells. Cells were primed with LPS, pre-treated with IMP-1711-S, and stimulated with the NLRP3 activator nigericin. We observed that the treatment with IMP-1711-S inhibited the production of IL-1β in a concentration-dependent manner in PMA-differentiated THP-1 cells (Figure 7B) and hiPSC-derived microglia (Figures 7K and 7L). Both caspase-1 p10 and cleaved IL-1β levels were reduced in supernatants from IMP-1711-S-treated THP-1 cells (Figures 7C–7E), suggesting that the inhibitor exerts its effect on activation of the caspase-1 and IL-1β processing stage. IMP-1711-S potently inhibited gasdermin D (GSDMD) cleavage, the release of lactate dehydrogenase (LDH), and blocked pyroptotic cell death induced by Nig (Figures 7F, 7G, and S11). Additionally, IMP-1711-S treatment did not affect pro-caspase-1 or pro-IL-1β expression in lysates in the priming stage with LPS stimulation (Figure 7C). Further investigation of ASC oligomerization in THP-1 cells through cross-linking of the insoluble lysate fraction revealed that, while IMP-1711-S had no impact on ASC expression in cell lysates, it substantially reduced oligomerized ASC levels post LPS and Nig stimulation (Figure 7H). Additionally, in HEK293 cells, IMP-1711-S markedly downregulated the formation of NLRP3 specks in a concentration-dependent manner (Figures 7I and 7J). Our findings underscore that UCH-L1 inhibition impedes NLRP3 inflammasome activation by disrupting NLRP3 assembly and speck formation, ultimately leading to decreased IL-1β production (Figure S20).

DISCUSSION

The NLRP3 inflammasome is central to innate immunity, and a detailed understanding of its molecular dynamics and interactome is highly sought after. We found that NLRP3 tolerates C-terminally tagged APEX2, retaining its competence to biotinylate and capture known interacting partners of endogenous NLRP3. Using complementary techniques, such as APEX2 PL-MS, AP-MS, and small interfering (siRNA) screening, we traced the time-resolved PPI networks local to the NLRP3 inflammasome upon stimulation. This approach offers a resource-rich map for further investigations of the molecular intricacies of NLRP3 inflammasome activation and revealed that UCH-L1 is involved in regulating IL-1β production.

Deconvolution of the NLRP3-APEX2 proximity proteome

A critical issue related to PL experiments is discrimination between true interactors and background noise. Proteins captured by NLRP3-APEX2 PL can be categorized into four groups. Type I proteins are true interacting proteins that physically interact with NLRP3 and or other components of the complex. Type II proteins are compartmental or proximal proteins in the local milieu of

Figure 5. Proximity proteome-guided RNAi screen identifies deubiquitinases that are involved in IL-1β production

(A–D) APEX2 PL identifies DUBs in the local milieu of NLRP3 upon nigericin stimulation. Shown is SAINT probability scoring of the proteomics data for NLRP3-APEX2 compared to the negative bead control. Proteins passing the cutoff (SAINT probability score ≥ 0.8 and FC-A score ≥ 1) are considered high-confidence proximal proteins for NLRP3. Deubiquitinases are colored blue, and all other proteins are shown in gray.

(E) Dot plots showing the DUBs in the NLRP3 proximity proteome upon nigericin stimulation for different times as indicated. Sizes denote the average spectral counts reflecting abundance, and colors denote the FC-A score (confidence of proximity to NLRP3).

(F) Schematic of the experimental design for the DUB siRNA library screen.

(G) Z score distribution of the IL-1β in the supernatant for individual siRNAs. The RNAi screen is carried out in PMA-differentiated THP-1 cells upon LPS (i) or LPS+nigericin treatment (ii), using ELISA for the measurement of IL-1β in the supernatant. Hits with a Z score ≤ -1 or ≥ 1 are chosen as candidates for further validation.

(H) Venn diagrams showing the intersection between the hits identified through APEX2-PL and the siRNA screen.

(I and J) Immunoblot and RT-qPCR analysis of whole-cell lysates and supernatants from THP-1 cells transfected with non-targeting control siRNA or UCH-L1-specific siRNA. Cells were differentiated with PMA and primed with LPS (1 μg/mL) for 4 h, followed by treatment with nigericin (10 μM) for different times as indicated. Error bars show the standard deviation of the mean.

(K and L) PBMCs were transfected with non-targeting control or UCH-L1-specific siRNA and stimulated with LPS for 4 h and nigericin for different times as indicated.

(K) Immunoblot of cell lysates from PBMCs.

(L) Production of IL-1β in the supernatants from PBMCs as measured by ELISA. Error bars show the standard deviation of the mean. $^*p < 0.05$, $^{**}p < 0.01$ (unpaired two-sided t test). The results are representative of 3 independent experiments.

(M and N) Immunoblot of cell lysates from HMC3 cells transfected with non-targeting control siRNA or UCH-L1-specific siRNA. Cells were primed with LPS (1 μg/mL) for 4 h, followed by treatment with nigericin (10 μM) for 45 min.

(N) IL-1β bands were quantified using GelAnalyzer and normalized using β-actin bands. Error bars show the standard deviation of the mean. $^{**}p < 0.01$ (unpaired two-sided t test).

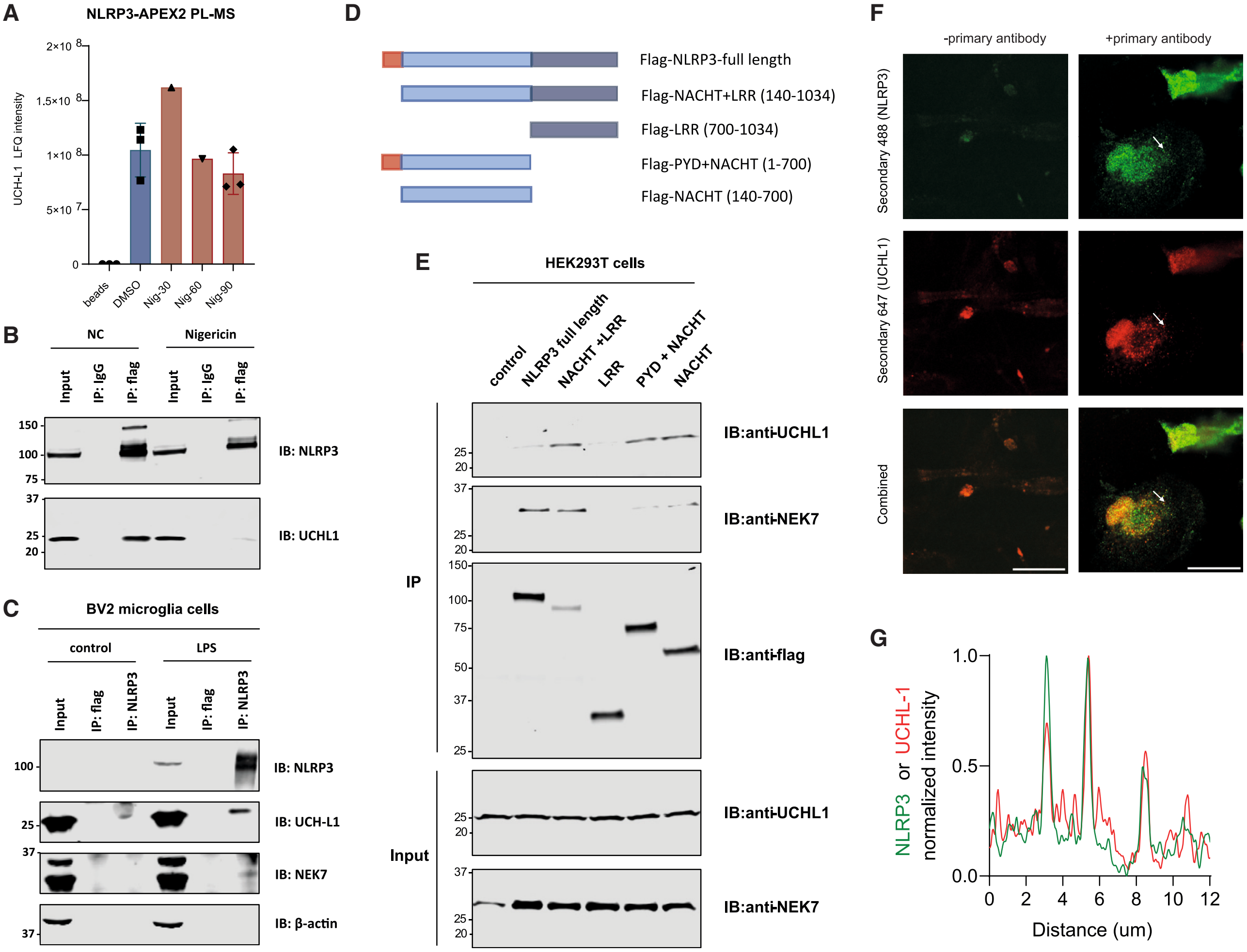

Figure 6. UCH-L1 interacts with the NACHT domain of NLRP3

(A) The raw label-free quantitation (LFQ) intensity of UCH-L1 protein identified in the APEX2 PL performed in this study across all samples, including bead control, DMSO control, and nigericin treatment at different time points. The experiment was performed in triplicate except for Nig-30 and Nig-60, where only 1 replication was performed.

(B) Flp-In T-Rex 293 NLRP3-FLAG stable cells were induced with tetracycline overnight. Afterward, cells were treated with DMSO or nigericin for 90 min. NLRP3-FLAG was pulled down using anti-FLAG antibody or immunoglobulin G (IgG) and immunoblotted with the indicated antibodies.

(C) BV2 microglia cells were treated with or without LPS (1 μg/mL) for 4 h, followed by co-immunoprecipitation with anti-NLRP3 antibody or isotype control and analysis by immunoblotting.

(D) Schematic of the N-terminal FLAG-tagged NLRP3 domain constructs: full-length NLRP3, NACHT and LRR domain NLRP3 (FLAG-NACHT+LRR, amino acids 140–1,034), LRR domain of NLRP3 (FLAG-LRR, amino acids 700–1,034), pyrin and NACHT domain of NLRP3 (FLAG-PYD+NACHT, amino acids 1–700), and NACHT domain of NLRP3 (FLAG-NACHT, amino acids 140–700).

(E) HEK293T cells were transfected with the appropriate NLRP3 plasmid using Lipofectamine 3000. Cells were cultured for 24 h before they were lysed. NLRP3 domain-FLAG was pulled down using anti-FLAG antibody and immunoblotted with the indicated antibodies.

(F) Fluorescence confocal images of hiPSC-derived microglial cells stained for UCHL-1 and NLPR3. UCHL-1 and NLRP3 show colocalization, but only when cells are stained with primary antibodies for UCHL-1 and NLRP3 (right column). No colocalization is shown when cells are not stained with primary antibodies against UCHL-1 and NLRP3 (left column).

(G) Line profile showing the min-max normalized intensity of UCHL-1 (red) and NRLP3 (green) along and in the direction of the white arrow indicated in (D). The peaks in normalized intensity indicate colocalization of NLRP3 and UCHL-1 in enriched areas (or “specks”) of NLRP3.

NLRP3, reflecting transient interactions. Type III proteins are non-specific proteins that stick to streptavidin beads. Type IV proteins are physically non-existing proteins detected in error. Type I and type II provide insights into the PPI network and local milieu of NLRP3, but type III and type IV are considered false positives. To establish a high-confidence proximity proteome resource for NLRP3, a variety of approaches were used to filter out type III and type IV contaminant proteins. A Bayesian model-based algorithm (SAINTexpress) was applied to analyze the PL data with a SAINT probability score threshold of 0.8 and FC $\geq$ 2, yielding 800–1,100 proximal proteins per group (Figures 3B and 3D–3H). Furthermore, the unstimulated state was used as a control, which

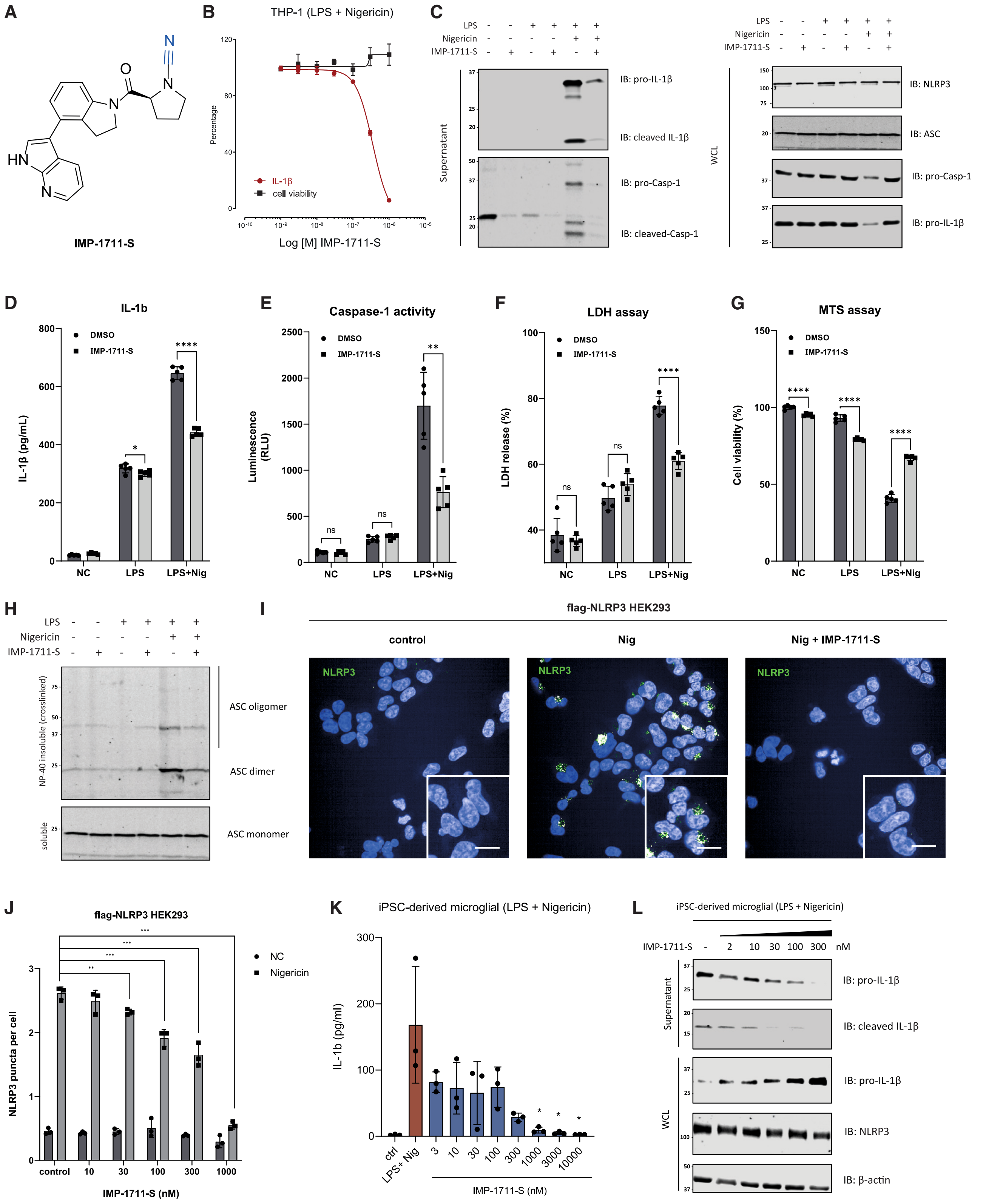

(legend on next page)

helped us distinguishing the differentially regulated interacting partners upon stimulation with nigericin, still yielding more than 800 proteins per biological condition, consistent with the APEX2 enzyme affording a biotin labeling radius of ∼10 nm in live cells.[40] With a stringent cutoff, our data identified 72 high-confidence putative NLRP3-associated proteins enriched under activated conditions and 55 proteins enriched under inactivated conditions. These included known interactors, such as NEK7, MAVS, PRKD1/2/3, LYN, and EIF2AK2 (Figure 4E). We note that spatial references have been shown to enhance the deconvolution of PL data. However, in our study, this was not applied, as NLRP3 resides in multiple compartments and translocates to distinct organelles upon activation.[31] By integrating PL data with AP-MS and siRNA screening, we established an alternative method for validating NLRP3-associated proteins.

UCH-L1 is an essential mediator of NLRP3/ASC assembly and IL-1β production

Ubiquitin modification controls multiple elements of the NLPR3 activation process and IL-1β production.[10] Through a DUB siRNA screen, we pinpointed four deubiquitylating enzymes (TNFAIP3, CYLD, USP7, and STAMBP) already linked to IL-1β signaling pathways (Figure 5G).[18,41–44] However, the intricate nature of IL-1β processing, spanning multiple regulatory stages, poses a challenge to precisely attribute the functional impacts of each DUB. For instance, UCH-L3 and L5 have been suggested to affect inflammasome activation and IL-1β production, although in the context of infection.[45–47] UCH-L3 may act in the priming stage, whereas UCH-L5's role may be less clear outside the context of pathogen-driven NLRP3 inflammasome activation, consistent with the former, but not the latter, being detected in our screen (Figure 5G).

Here, we identified UCH-L1 as an NLRP3-interacting modulator of the inflammasome. It is a member of the UCH family involved in neurodegeneration and cancer metastasis.[48–50] Single-cell and spatial transcriptomics show that UCH-L1 and NLRP3 inflammasome components are simultaneously expressed in multiple CNS-resident cells, including microglia in parenchyma, CNS-associated macrophages (CAMs), monocytes, and B cells (Figure S12). As these immune cell lineages play essential roles in CNS inflammation contributing to neuropathology, we postulate the potential involvement of UCH-L1 in several neurodegenerative and neuroinflammatory diseases. This is consistent with the genetic association of UCH-L1 with Parkinson's disease,[49] Alzheimer's disease[51,52] and amyotrophic lateral sclerosis.[53] Also, several studies have linked UCH-L1 to inflammation or innate immunity more generally. For instance, UCH-L1 deficiency markedly reduces the secretion of pro-inflammatory cytokines, notably IL-6 and TNF-α.[54] LDN57444, an isatin O-acyl oxime small-molecule inhibitor, has demonstrated efficacy in ameliorating LPS-induced sepsis in *in vivo* models,[54] although other studies have cast doubt on the specificity or efficacy of this compound against UCH-L1.[38] Another study reported that UCH-L1 promoted M1 macrophage polarization via the phosphatidylinositol 3-kinase (PI3K)/Akt signaling pathway.[55] Consistent with previous findings, UCH-L1 knockdown or inhibition yielded a significant decrease in pro-inflammatory cytokine expression and secretion, including IL-1β, IL-6, and TNF-α, in both THP-1 cells and human PBMCs, reflecting interference in upstream signaling affecting the priming stage (Figures 5I–5L, S9, and S13). Furthermore, mRNA levels of IL-1β remain unchanged in the absence of UCH-L1, suggesting that UCH-L1 affects IL-1β at the post-transcriptional or protein level (Figure 5J). Notably, pharmacological inhibition of UCH-L1 affected ASC/NLRP3 assembly and IL-1β production, which are part of the second inflammasome induction signal (Figure 7). Although the small-molecule inhibitor IMP-1711-S altered secreted active caspase-1 levels (Figure 7E), it does not seem to cross-react or inhibit caspases directly.[38] Caspase-1 inhibitors also show a different specificity profile toward TNF-α release.[56] To elaborate on the role of UCH-L1 involved in NLRP3 inflammasome activation, we utilized various methods, including siRNA knockdown, CRISPR-Cas9-induced genome editing, and pharmacological intervention. While the three distinct silencing strategies produce similar phenotypes, all demonstrating inhibitory regulation of IL-1β production, the varied impacts at different stages of inflammasome activation suggest divergent mechanisms

Figure 7. UCH-L1 inhibitor blocks ASC/NLRP3 assembly and IL-1β production

(A) UCH-L1 inhibitor IMP-1711-S structure.

(B) Red, production of IL-1β from PMA-differentiated THP-1 cells stimulated with LPS and nigericin and treated with IMP-1711-S (3–10,000 nM) as measured by ELISA (red); black, cell viability measured by MTS assay. Data are expressed as mean ± SD, $n = 3$ biologically independent samples.

(C–G) THP-1 cells were differentiated with PMA and primed with LPS (1 μg/mL) for 4 h, followed by treatment with nigericin (10 μM) for 45 min. DMSO or IMP-1711-S (0.3 μM) was added at the same time as LPS.

(C) Immunoblot analysis of whole-cell lysates and supernatants from THP-1 cells treated with DMSO or IMP-1711-S.

(D–G) Supernatants were collected for the measurement of IL-1β (D) and caspase-1 activity (E) from 3 independent experiments. Error bars show the standard deviation of the mean. $^{*}p < 0.05$, $^{**}p < 0.01$, $^{***}p < 0.001$, $^{****}p < 0.0001$ (unpaired two-sided t test). Additionally, the cell viability was measured using an LDH assay (F) and MTS assay (G).

(H) Immunoblot analysis of ASC polymerization upon treatment with DMSO or IMP-1711-S.

(I) Immunofluorescence imaging of FLAG-NLRP3 HEK293 stable cells treated with DMSO or IMP-1711-S (300 nM), followed by stimulation with nigericin. Scale bars, 10 μm.

(J) Quantitative analysis of NLRP3 puncta formation upon nigericin treatment in the presence of DMSO or different doses of IMP-1711-S (0.001–1 μM) as indicated. Error bars show the standard deviation of the mean. $^{**}p < 0.01$, $^{***}p < 0.001$ (unpaired two-sided t test).

(K) IL-1β levels were determined using ELISA from the supernatant of fully differentiated hiPSC-derived microglia. Cells were primed with LPS (1 μg/mL) for 4 h, followed by treatment with nigericin (10 μM) for 45 min. IMP-1711-S inhibitor was added simultaneously with LPS at different concentrations. Error bars show the standard deviation of the mean. $^{*}p < 0.05$ (unpaired two-sided t test).

(L) Immunoblot analysis of whole-cell lysates and supernatants from hiPSC-derived microglia treated with DMSO or different concentrations of IMP-1711-S as indicated.

of action (Figures 7, S14, and S16). UCH-L1, found to be bound to the NACHT domain of NLRP3, may act as a gating/editing factor to control the ubiquitylation status of multiple components, such as NLRP3, ASC, caspase-1, and IL-1β, required for NLRP3-ASC inflammasome complex assembly (Figure S20). Preliminary results indicate that NLRP3's half-life is dependent on the ubiquitin-proteasome pathway (Figure S15). However, NLRP3-associated ubiquitylation appears to be minimally altered by UCH-L1, and NLRP3 protein levels are unaffected (Figure S16), suggesting a more structural role for UCH-L1 and/or its modulation of NLRP3 ubiquitination during assembly rather than controlling turnover. Though speculative at this stage, such a putative structural and ubiquitylation editing "gate keeping" process maybe in analogy to the role of UCH-L5/UCH37 in the 26S proteasome complex, required for substrate deubiquitylation and ubiquitin recycling prior to substrate unfolding by the 19S and entry into the 20S for destruction,[57,58] or perhaps UCH-L1 interacting with the proteasome to interfere with protein degradation, causing proteotoxic stress in podocytes.[59]

Apart from UCH-L1, this approach also enabled the discovery of several unexpected hits, including stress granule components (such as DDX3X and G3BP2), early endosome component (EEA1), CSNK1A1, and IKKβ, which have been verified by recent studies (Figures S17 and S18).[30,60–62] In conclusion, in this study, we provide a detailed NLRP3 inflammasome proximity map at different physiological stages. UCH-L1 was identified and validated as an essential regulator involved in NLRP3 inflammasome activation and IL-1β production, affected by UCH-L1 chemical inhibition, and phenocopied by UCH-L1 deletion. Our results may have translational implications for exploring pharmacological inhibition of UCH-L1 in neuroinflammation-associated pathology, which could include dementia.

Limitations of the study

Limitations associated with the APEX2 PL-MS study include the use of HEK293 cells instead of a proper immune cell type, where NLRP3 inflammasome assembly typically occurs. While our research and others[33,63,64] have successfully demonstrated that the NLRP3 inflammasome can be reconstituted in HEK293T cells, suggesting the presence of essential components, it is possible that certain regulatory factors may be absent in HEK293 cells that would be present in a more appropriate myeloid-derived cell lineage.

Given that chemical inhibitors may have off-target effects that potentially confound data interpretation, we tested another cyanopyrrolidine moiety-containing UCH-L1 inhibitor (6RK73) in THP-1 cells (Figure S19). While both inhibitors reduced IL-1β production, their varied impact may suggest divergent mechanisms of action. This is probably due to either differences in the selectivity profiles of the compounds or possible individual off-target effects of these inhibitors.

It is crucial to clarify that the presence of all of the proteins identified in our study via APEX2 does not necessarily indicate a direct interaction with NLRP3 or the inflammasome complex. Further validation is essential to investigate whether any of the additional hits identified in our study has physical interaction with NLRP3 itself and/or other components of the inflammasome.

STAR★METHODS

Detailed methods are provided in the online version of this paper and include the following:

- KEY RESOURCES TABLE
- RESOURCE AVAILABILITY
  - ○ Lead contact
  - ○ Materials availability
  - ○ Data and code availability
- EXPERIMENTAL MODEL AND SUBJECT PARTICIPANT DETAILS
  - ○ Cell culture
  - ○ PBMC isolation and *in vitro* culture
  - ○ hiPSC culture and differentiation to microglia
- METHOD DETAILS
  - ○ Inflammasome activation assay
  - ○ ASC speck oligomer crosslinking
  - ○ Enzyme-linked immunosorbent assay (ELISA)
  - ○ TCA/DOC protein precipitation
  - ○ Cytotoxicity and cell viability assay
  - ○ Caspase-1 activity bioluminescent assay
  - ○ Immunoprecipitation
  - ○ Transient transfection
  - ○ Construction of plasmids
  - ○ Generation of stable cell line
  - ○ sgRNA design, lentivirus production and transduction
  - ○ PCR and agarose gel electrophoresis
  - ○ Biotin-phenol proximity labeling and biotinylated proteins capture
  - ○ Affinity-purification mass spectrometry (AP-MS)
  - ○ Mass spectrometry analysis
  - ○ RNA extraction and real time reverse transcription (RT)-PCR
  - ○ Pathway enrichment analysis
  - ○ PPIs network construction
- QUANTIFICATION AND STATISTICAL ANALYSIS
  - ○ SAINT probabilistic scoring for NLRP3 APEX2 PL-MS and AP-MS data
- STATISTICS AND REPRODUCIBILITY

SUPPLEMENTAL INFORMATION

Supplemental information can be found online at https://doi.org/10.1016/j.celrep.2024.114152.

ACKNOWLEDGMENTS

Z.L., A.D., I.V., G.L., X.Z., R.F., T.D., and B.M.K. were supported by the Chinese Academy of Medical Sciences (CAMS) Innovation Fund for Medical Science (CIFMS), China (grant 2018-I2M-2-002) awarded to B.M.K., R.F., and T.D. B.M.K. and A.D. were supported by Pfizer. E.D. was supported by Alzheimer's Research UK grant ARUK2015DDI-OX. E.J. was funded by the Wellcome Trust (grant 224040/Z/21/Z). Imaging was performed using the Oxford-Zeiss Centre of Excellence in Biomedical Imaging and the Kennedy Trust for Rheumatology Research (grants 202117 and 202103, respectively). E.W.T. was supported by a CRUK program award (DRCNPG-Nov21\100001) with support from the Engineering & Physical Sciences Research Council. We thank members of the Discovery Proteomics Facility and the Kessler and Oxford Drug Discovery Institute groups for constructive discussions. We would also like to thank Raphael Heilig for assistance with mass spectrometry and Dr. Val Millar and Ebner's group for expert help in the use of PerkinElmer Opera Phenix/High Content Imaging.

AUTHOR CONTRIBUTIONS

B.M.K., E.D.D., and Z.L. designed the research and wrote the manuscript. Z.L. and A.D. performed the NLRP3-APEX2 proximity labeling experiments and analyzed the mass spectrometry data. Z.L., A.D., and A.G. performed the DUB siRNA library screen experiment. I.V. operated the mass spectrometer

for LC-MS/MS acquisition of the samples and contributed to data processing. E.J. performed confocal imaging and analysis. S.J.W. and A.D. contributed to the culture of hiPSCs and differentiated them into microglial cells. E.W.T. and F.C. contributed to UCH-L1 inhibitor provision and study design. Z.L., A.D., I.V., E.J., F.H.L., S.J.W., G.L., G.Y., H.L., F.C., X.Z., R.A.F., T.D., E.W.T., E.D.D., and B.M.K. discussed the results and commented on and provided critical reviews of the manuscript.

DECLARATION OF INTERESTS

E.W.T. is a founder and shareholder in Myricx Pharma Ltd. and receives consultancy or research funding from Kura Oncology, Pfizer Ltd., Samsara Therapeutics, Myricx Pharma Ltd., MSD, Exscientia, and Daiichi Sankyo.

Received: November 10, 2023
Revised: February 28, 2024
Accepted: April 10, 2024
Published: April 25, 2024

REFERENCES

1. Paludan, S.R., Pradeu, T., Masters, S.L., and Mogensen, T.H. (2021). Constitutive immune mechanisms: mediators of host defence and immune regulation. Nat. Rev. Immunol. *21*, 137–150. https://doi.org/10.1038/s41577-020-0391-5.
2. Martinon, F., Burns, K., and Tschopp, J. (2002). The inflammasome: a molecular platform triggering activation of inflammatory caspases and processing of proIL-beta. Mol. Cell *10*, 417–426. https://doi.org/10.1016/s1097-2765(02)00599-3.
3. Gross, O., Yazdi, A.S., Thomas, C.J., Masin, M., Heinz, L.X., Guarda, G., Quadroni, M., Drexler, S.K., and Tschopp, J. (2012). Inflammasome activators induce interleukin-1alpha secretion via distinct pathways with differential requirement for the protease function of caspase-1. Immunity *36*, 388–400. https://doi.org/10.1016/j.immuni.2012.01.018.
4. Shao, B.Z., Xu, Z.Q., Han, B.Z., Su, D.F., and Liu, C. (2015). NLRP3 inflammasome and its inhibitors: a review. Front. Pharmacol. *6*, 262. https://doi.org/10.3389/fphar.2015.00262.
5. Swanson, K.V., Deng, M., and Ting, J.P.Y. (2019). The NLRP3 inflammasome: molecular activation and regulation to therapeutics. Nat. Rev. Immunol. *19*, 477–489. https://doi.org/10.1038/s41577-019-0165-0.
6. He, Y., Zeng, M.Y., Yang, D., Motro, B., and Núñez, G. (2016). NEK7 is an essential mediator of NLRP3 activation downstream of potassium efflux. Nature *530*, 354–357. https://doi.org/10.1038/nature16959.
7. Akther, M., Haque, M.E., Park, J., Kang, T.B., and Lee, K.H. (2021). NLRP3 Ubiquitination-A New Approach to Target NLRP3 Inflammasome Activation. Int. J. Mol. Sci. *22*, 8780. https://doi.org/10.3390/ijms22168780.
8. Liang, Z., Damianou, A., Di Daniel, E., and Kessler, B.M. (2021). Inflammasome activation controlled by the interplay between post-translational modifications: emerging drug target opportunities. Cell Commun. Signal. *19*, 23. https://doi.org/10.1186/s12964-020-00688-6.
9. Zangiabadi, S., and Abdul-Sater, A.A. (2022). Regulation of the NLRP3 Inflammasome by Posttranslational Modifications. JJ. Immunol. *208*, 286–292. https://doi.org/10.4049/jimmunol.2100734.
10. Lopez-Castejon, G. (2020). Control of the inflammasome by the ubiquitin system. FEBS J. *287*, 11–26. https://doi.org/10.1111/febs.15118.
11. Song, H., Liu, B., Huai, W., Yu, Z., Wang, W., Zhao, J., Han, L., Jiang, G., Zhang, L., Gao, C., and Zhao, W. (2016). The E3 ubiquitin ligase TRIM31 attenuates NLRP3 inflammasome activation by promoting proteasomal degradation of NLRP3. Nat. Commun. *7*, 13727. https://doi.org/10.1038/ncomms13727.
12. Xu, T., Yu, W., Fang, H., Wang, Z., Chi, Z., Guo, X., Jiang, D., Zhang, K., Chen, S., Li, M., et al. (2022). Ubiquitination of NLRP3 by gp78/Insig-1 restrains NLRP3 inflammasome activation. Cell Death Differ. *29*, 1582–1595. https://doi.org/10.1038/s41418-022-00947-8.
13. Yan, Y., Jiang, W., Liu, L., Wang, X., Ding, C., Tian, Z., and Zhou, R. (2015). Dopamine controls systemic inflammation through inhibition of NLRP3 inflammasome. Cell *160*, 62–73. https://doi.org/10.1016/j.cell.2014.11.047.
14. Guo, Y., Li, L., Xu, T., Guo, X., Wang, C., Li, Y., Yang, Y., Yang, D., Sun, B., Zhao, X., et al. (2020). HUWE1 mediates inflammasome activation and promotes host defense against bacterial infection. J. Clin. Invest. *130*, 6301–6316. https://doi.org/10.1172/JCI138234.
15. Tang, J., Tu, S., Lin, G., Guo, H., Yan, C., Liu, Q., Huang, L., Tang, N., Xiao, Y., Pope, R.M., et al. (2020). Sequential ubiquitination of NLRP3 by RNF125 and Cbl-b limits inflammasome activation and endotoxemia. JJ. Exp. Med. *217*, e20182091. https://doi.org/10.1084/jem.20182091.
16. Lopez-Castejon, G., and Edelmann, M.J. (2016). Deubiquitinases: Novel Therapeutic Targets in Immune Surveillance? Mediators Inflamm *2016*, 3481371. https://doi.org/10.1155/2016/3481371.
17. Lopez-Castejon, G., Luheshi, N.M., Compan, V., High, S., Whitehead, R.C., Flitsch, S., Kirov, A., Prudovsky, I., Swanton, E., and Brough, D. (2013). Deubiquitinases regulate the activity of caspase-1 and interleukin-1beta secretion via assembly of the inflammasome. J. Biol. Chem. *288*, 2721–2733. https://doi.org/10.1074/jbc.M112.422238.
18. Palazón-Riquelme, P., Worboys, J.D., Green, J., Valera, A., Martín-Sánchez, F., Pellegrini, C., Brough, D., and López-Castejón, G. (2018). USP7 and USP47 deubiquitinases regulate NLRP3 inflammasome activation. EMBO Rep. *19*, e44766. https://doi.org/10.15252/embr.201744766.
19. Py, B.F., Kim, M.S., Vakifahmetoglu-Norberg, H., and Yuan, J. (2013). Deubiquitination of NLRP3 by BRCC3 critically regulates inflammasome activity. Mol. Cell *49*, 331–338. https://doi.org/10.1016/j.molcel.2012.11.009.
20. Song, H., Zhao, C., Yu, Z., Li, Q., Yan, R., Qin, Y., Jia, M., and Zhao, W. (2020). UAF1 deubiquitinase complexes facilitate NLRP3 inflammasome activation by promoting NLRP3 expression. Nat. Commun. *11*, 6042. https://doi.org/10.1038/s41467-020-19939-8.
21. Ren, G., Zhang, X., Xiao, Y., Zhang, W., Wang, Y., Ma, W., Wang, X., Song, P., Lai, L., Chen, H., et al. (2019). ABRO1 promotes NLRP3 inflammasome activation through regulation of NLRP3 deubiquitination. EMBO J. *38*, e100376. https://doi.org/10.15252/embj.2018100376.
22. Xiao, L., Magupalli, V.G., and Wu, H. (2023). Cryo-EM structures of the active NLRP3 inflammasome disc. Nature *613*, 595–600. https://doi.org/10.1038/s41586-022-05570-8.
23. Sharif, H., Wang, L., Wang, W.L., Magupalli, V.G., Andreeva, L., Qiao, Q., Hauenstein, A.V., Wu, Z., Núñez, G., Mao, Y., and Wu, H. (2019). Structural mechanism for NEK7-licensed activation of NLRP3 inflammasome. Nature *570*, 338–343. https://doi.org/10.1038/s41586-019-1295-z.
24. Teo, G., Liu, G., Zhang, J., Nesvizhskii, A.I., Gingras, A.C., and Choi, H. (2014). SAINTexpress: improvements and additional features in Significance Analysis of INTeractome software. J. Proteomics *100*, 37–43. https://doi.org/10.1016/j.jprot.2013.10.023.
25. Stark, C., Breitkreutz, B.J., Reguly, T., Boucher, L., Breitkreutz, A., and Tyers, M. (2006). BioGRID: a general repository for interaction datasets. Nucleic Acids Res. *34*, D535–D539539. https://doi.org/10.1093/nar/gkj109.
26. Oughtred, R., Stark, C., Breitkreutz, B.J., Rust, J., Boucher, L., Chang, C., Kolas, N., O'Donnell, L., Leung, G., McAdam, R., et al. (2019). The BioGRID interaction database: 2019 update. Nucleic Acids Res. *47*, D529–D541. https://doi.org/10.1093/nar/gky1079.
27. Oughtred, R., Rust, J., Chang, C., Breitkreutz, B.J., Stark, C., Willems, A., Boucher, L., Leung, G., Kolas, N., Zhang, F., et al. (2021). The BioGRID database: A comprehensive biomedical resource of curated protein, genetic, and chemical interactions. Protein Sci. *30*, 187–200. https://doi.org/10.1002/pro.3978.
28. Zhang, Z., Meszaros, G., He, W.T., Xu, Y., de Fatima Magliarelli, H., Mailly, L., Mihlan, M., Liu, Y., Puig Gámez, M., Goginashvili, A., et al. (2017). Protein kinase D at the Golgi controls NLRP3 inflammasome activation. JJ. Exp. Med. *214*, 2671–2693. https://doi.org/10.1084/jem.20162040.

29. Fox, D., and Man, S.M. (2019). DDX3X: stressing the NLRP3 inflammasome. Cell Res. *29*, 969–970. https://doi.org/10.1038/s41422-019-0250-8.

30. Samir, P., Kesavardhana, S., Patmore, D.M., Gingras, S., Malireddi, R.K.S., Karki, R., Guy, C.S., Briard, B., Place, D.E., Bhattacharya, A., et al. (2019). DDX3X acts as a live-or-die checkpoint in stressed cells by regulating NLRP3 inflammasome. Nature *573*, 590–594. https://doi.org/10.1038/s41586-019-1551-2.

31. Hamilton, C., and Anand, P.K. (2019). Right place, right time: localisation and assembly of the NLRP3 inflammasome. F1000Res. *8*. https://doi.org/10.12688/f1000research.18557.1.

32. Bordon, Y. (2019). Trans-Golgi network breaks away to activate NLRP3. Nat. Rev. Immunol. *19*, 68–69. https://doi.org/10.1038/s41577-018-0111-6.

33. Chen, J., and Chen, Z.J. (2018). PtdIns4P on dispersed trans-Golgi network mediates NLRP3 inflammasome activation. Nature *564*, 71–76. https://doi.org/10.1038/s41586-018-0761-3.

34. Lambert, J.P., Tucholska, M., Go, C., Knight, J.D., and Gingras, A.C. (2015). Proximity biotinylation and affinity purification are complementary approaches for the interactome mapping of chromatin-associated protein complexes. J. Proteomics *118*, 81–94. https://doi.org/10.1016/j.jprot.2014.09.011.

35. Xiang, Y., Li, X., Cai, M., and Cai, D. (2023). USP9X promotes lipopolysaccharide-stimulated acute lung injury by deubiquitination of NLRP3. Cell Biol. Int. *47*, 394–405. https://doi.org/10.1002/cbin.11932.

36. Hai, B., Mao, T., Du, C., Jia, F., Liu, Y., Song, Q., Pan, X., Liu, X., and Zhu, B. (2022). USP14 promotes pyroptosis of human annulus fibrosus cells derived from patients with intervertebral disc degeneration through deubiquitination of NLRP3. Acta Biochim. Biophys. Sin. *54*, 1720–1730. https://doi.org/10.3724/abbs.2022171.

37. Mark Kemp, M.S., and Alison, J. (2017). Cyanopyrrolidines as Dub Inhibitors for the Treatment of Cancer (Patent Application WO2017009650A1).

38. Panyain, N., Godinat, A., Lanyon-Hogg, T., Lachiondo-Ortega, S., Will, E.J., Soudy, C., Mondal, M., Mason, K., Elkhalifa, S., Smith, L.M., et al. (2020). Discovery of a Potent and Selective Covalent Inhibitor and Activity-Based Probe for the Deubiquitylating Enzyme UCHL1, with Antifibrotic Activity. J. Am. Chem. Soc. *142*, 12020–12026. https://doi.org/10.1021/jacs.0c04527.

39. Panyain, N., Godinat, A., Thawani, A.R., Lachiondo-Ortega, S., Mason, K., Elkhalifa, S., Smith, L.M., Harrigan, J.A., and Tate, E.W. (2021). Activity-based protein profiling reveals deubiquitinase and aldehyde dehydrogenase targets of a cyanopyrrolidine probe. RSC Med. Chem. *12*, 1935–1943. https://doi.org/10.1039/d1md00218j.

40. Qin, W., Cho, K.F., Cavanagh, P.E., and Ting, A.Y. (2021). Deciphering molecular interactions by proximity labeling. Nat. Methods *18*, 133–143. https://doi.org/10.1038/s41592-020-01010-5.

41. Yang, X.D., Li, W., Zhang, S., Wu, D., Jiang, X., Tan, R., Niu, X., Wang, Q., Wu, X., Liu, Z., et al. (2020). PLK4 deubiquitination by Spata2-CYLD suppresses NEK7-mediated NLRP3 inflammasome activation at the centrosome. EMBO J. *39*, e102201. https://doi.org/10.15252/embj.2019102201.

42. Vande Walle, L., Van Opdenbosch, N., Jacques, P., Fossoul, A., Verheugen, E., Vogel, P., Beyaert, R., Elewaut, D., Kanneganti, T.D., van Loo, G., and Lamkanfi, M. (2014). Negative regulation of the NLRP3 inflammasome by A20 protects against arthritis. Nature *512*, 69–73. https://doi.org/10.1038/nature13322.

43. Duong, B.H., Onizawa, M., Oses-Prieto, J.A., Advincula, R., Burlingame, A., Malynn, B.A., and Ma, A. (2015). A20 restricts ubiquitination of pro-interleukin-1beta protein complexes and suppresses NLRP3 inflammasome activity. Immunity *42*, 55–67. https://doi.org/10.1016/j.immuni.2014.12.031.

44. Bednash, J.S., Johns, F., Patel, N., Smail, T.R., Londino, J.D., and Mallampalli, R.K. (2021). The deubiquitinase STAMBP modulates cytokine secretion through the NLRP3 inflammasome. Cell. Signal. *79*, 109859. https://doi.org/10.1016/j.cellsig.2020.109859.

45. Ramachandran, A., Kumar, B., Waris, G., and Everly, D. (2021). Deubiquitination and Activation of the NLRP3 Inflammasome by UCHL5 in HCV-Infected Cells. Microbiol. Spectr. *9*, e0075521. https://doi.org/10.1128/Spectrum.00755-21.

46. Qu, Z., Zhou, J., Zhou, Y., Xie, Y., Jiang, Y., Wu, J., Luo, Z., Liu, G., Yin, L., and Zhang, X.L. (2020). Mycobacterial EST12 activates a RACK1-NLRP3-gasdermin D pyroptosis-IL-1beta immune pathway. Sci. Adv. *6*, eaba4733. https://doi.org/10.1126/sciadv.aba4733.

47. Kummari, E., Alugubelly, N., Hsu, C.Y., Dong, B., Nanduri, B., and Edelmann, M.J. (2015). Activity-Based Proteomic Profiling of Deubiquitinating Enzymes in Salmonella-Infected Macrophages Leads to Identification of Putative Function of UCH-L5 in Inflammasome Regulation. PLoS One *10*, e0135531. https://doi.org/10.1371/journal.pone.0135531.

48. Liu, Y., Fallon, L., Lashuel, H.A., Liu, Z., and Lansbury, P.T., Jr. (2002). The UCH-L1 gene encodes two opposing enzymatic activities that affect alpha-synuclein degradation and Parkinson's disease susceptibility. Cell *111*, 209–218. https://doi.org/10.1016/s0092-8674(02)01012-7.

49. Ham, S.J., Lee, D., Xu, W.J., Cho, E., Choi, S., Min, S., Park, S., and Chung, J. (2021). Loss of UCHL1 rescues the defects related to Parkinson's disease by suppressing glycolysis. Sci. Adv. *7*, eabg4574. https://doi.org/10.1126/sciadv.abg4574.

50. Mondal, M., Conole, D., Nautiyal, J., and Tate, E.W. (2022). UCHL1 as a novel target in breast cancer: emerging insights from cell and chemical biology. Br. J. Cancer *126*, 24–33. https://doi.org/10.1038/s41416-021-01516-5.

51. Reinicke, A.T., Laban, K., Sachs, M., Kraus, V., Walden, M., Damme, M., Sachs, W., Reichelt, J., Schweizer, M., Janiesch, P.C., et al. (2019). Ubiquitin C-terminal hydrolase L1 (UCH-L1) loss causes neurodegeneration by altering protein turnover in the first postnatal weeks. Proc. Natl. Acad. Sci. USA *116*, 7963–7972. https://doi.org/10.1073/pnas.1812413116.

52. Corsetti, V., Florenzano, F., Atlante, A., Bobba, A., Ciotti, M.T., Natale, F., Della Valle, F., Borreca, A., Manca, A., Meli, G., et al. (2015). NH2-truncated human tau induces deregulated mitophagy in neurons by aberrant recruitment of Parkin and UCHL-1: implications in Alzheimer's disease. Hum. Mol. Genet. *24*, 3058–3081. https://doi.org/10.1093/hmg/ddv059.

53. Dellar, E.R., Vendrell, I., Talbot, K., Kessler, B.M., Fischer, R., Turner, M.R., and Thompson, A.G. (2024). Data-independent acquisition proteomics of cerebrospinal fluid implicates endoplasmic reticulum and inflammatory mechanisms in amyotrophic lateral sclerosis. J. Neurochem. *168*, 115–127. https://doi.org/10.1111/jnc.16030.

54. Zhang, Z., Liu, N., Chen, X., Zhang, F., Kong, T., Tang, X., Yang, Q., Chen, W., Xiong, X., and Chen, X. (2021). UCHL1 regulates inflammation via MAPK and NF-kappaB pathways in LPS-activated macrophages. Cell Biol. Int. *45*, 2107–2117. https://doi.org/10.1002/cbin.11662.

55. Huang, Y., He, S., Chen, Y., Sheng, J., Fu, Y., Du, X., Yang, Y., Liu, H., Han, Z., Huang, Y., et al. (2022). UCHL1 Promoted Polarization of M1 Macrophages by Regulating the PI3K/AKT Signaling Pathway. J. Inflamm. Res. *15*, 735–746. https://doi.org/10.2147/JIR.S343487.

56. Cao, D.Y., Zhang, Z.H., Li, R.Z., Shi, X.K., Xi, R.Y., Zhang, G.L., Li, F., and Wang, F. (2022). A small molecule inhibitor of caspase-1 inhibits NLRP3 inflammasome activation and pyroptosis to alleviate gouty inflammation. Immunol. Lett. *244*, 28–39. https://doi.org/10.1016/j.imlet.2022.03.003.

57. Song, A., Hazlett, Z., Abeykoon, D., Dortch, J., Dillon, A., Curtiss, J., Martinez, S.B., Hill, C.P., Yu, C., Huang, L., et al. (2021). Branched ubiquitin chain binding and deubiquitination by UCH37 facilitate proteasome clearance of stress-induced inclusions. Elife *10*, e72798. https://doi.org/10.7554/eLife.72798.

58. Vander Linden, R.T., Hemmis, C.W., Schmitt, B., Ndoja, A., Whitby, F.G., Robinson, H., Cohen, R.E., Yao, T., and Hill, C.P. (2015). Structural basis for the activation and inhibition of the UCH37 deubiquitylase. Mol. Cell *57*, 901–911. https://doi.org/10.1016/j.molcel.2015.01.016.

59. Reichelt, J., Sachs, W., Frömbling, S., Fehlert, J., Studencka-Turski, M., Betz, A., Loreth, D., Blume, L., Witt, S., Pohl, S., et al. (2023). Non-functional ubiquitin C-terminal hydrolase L1 drives podocyte injury through

impairing proteasomes in autoimmune glomerulonephritis. Nat. Commun. *14*, 2114. https://doi.org/10.1038/s41467-023-37836-8.

60. Zhang, Z., Venditti, R., Ran, L., Liu, Z., Vivot, K., Schürmann, A., Bonifacino, J.S., De Matteis, M.A., and Ricci, R. (2023). Distinct changes in endosomal composition promote NLRP3 inflammasome activation. Nat. Immunol. *24*, 30–41. https://doi.org/10.1038/s41590-022-01355-3.
61. Schmacke, N.A., O'Duill, F., Gaidt, M.M., Szymanska, I., Kamper, J.M., Schmid-Burgk, J.L., Madler, S.C., Mackens-Kiani, T., Kozaki, T., Chauhan, D., et al. (2022). IKKbeta primes inflammasome formation by recruiting NLRP3 to the trans-Golgi network. Immunity *55*, 2271–2284.e2277. https://doi.org/10.1016/j.immuni.2022.10.021.
62. Niu, T., De Rosny, C., Chautard, S., Rey, A., Patoli, D., Groslambert, M., Cosson, C., Lagrange, B., Zhang, Z., Visvikis, O., et al. (2021). NLRP3 phosphorylation in its LRR domain critically regulates inflammasome assembly. Nat. Commun. *12*, 5862. https://doi.org/10.1038/s41467-021-26142-w.
63. Bartok, E., Kampes, M., and Hornung, V. (2016). Measuring IL-1beta Processing by Bioluminescence Sensors II: The iGLuc System. Methods Mol. Biol. *1417*, 97–113. https://doi.org/10.1007/978-1-4939-3566-6_6.
64. Bartok, E., Bauernfeind, F., Khaminets, M.G., Jakobs, C., Monks, B., Fitzgerald, K.A., Latz, E., and Hornung, V. (2013). iGLuc: a luciferase-based inflammasome and protease activity reporter. Nat. Methods *10*, 147–154. https://doi.org/10.1038/nmeth.2327.
65. Tyanova, S., Temu, T., Sinitcyn, P., Carlson, A., Hein, M.Y., Geiger, T., Mann, M., and Cox, J. (2016). The Perseus computational platform for comprehensive analysis of (prote)omics data. Nat. Methods *13*, 731–740. https://doi.org/10.1038/nmeth.3901.
66. Schindelin, J., Arganda-Carreras, I., Frise, E., Kaynig, V., Longair, M., Pietzsch, T., Preibisch, S., Rueden, C., Saalfeld, S., Schmid, B., et al. (2012). Fiji: an open-source platform for biological-image analysis. Nat. Methods *9*, 676–682. https://doi.org/10.1038/nmeth.2019.
67. Shannon, P., Markiel, A., Ozier, O., Baliga, N.S., Wang, J.T., Ramage, D., Amin, N., Schwikowski, B., and Ideker, T. (2003). Cytoscape: a software environment for integrated models of biomolecular interaction networks. Genome Res. *13*, 2498–2504. https://doi.org/10.1101/gr.1239303.
68. Tyanova, S., Temu, T., and Cox, J. (2016). The MaxQuant computational platform for mass spectrometry-based shotgun proteomics. Nat. Protoc. *11*, 2301–2319. https://doi.org/10.1038/nprot.2016.136.
69. Perez-Riverol, Y., Bai, J., Bandla, C., García-Seisdedos, D., Hewapathirana, S., Kamatchinathan, S., Kundu, D.J., Prakash, A., Frericks-Zipper, A., Eisenacher, M., et al. (2022). The PRIDE database resources in 2022: a hub for mass spectrometry-based proteomics evidences. Nucleic Acids Res. *50*, D543–D552. https://doi.org/10.1093/nar/gkab1038.
70. Deutsch, E.W., Bandeira, N., Perez-Riverol, Y., Sharma, V., Carver, J.J., Mendoza, L., Kundu, D.J., Wang, S., Bandla, C., Kamatchinathan, S., et al. (2023). The ProteomeXchange consortium at 10 years: 2023 update. Nucleic Acids Res. *51*, D1539–D1548. https://doi.org/10.1093/nar/gkac1040.
71. Bruntraeger, M., Byrne, M., Long, K., and Bassett, A.R. (2019). Editing the Genome of Human Induced Pluripotent Stem Cells Using CRISPR/Cas9 Ribonucleoprotein Complexes. Methods Mol. Biol. *1961*, 153–183. https://doi.org/10.1007/978-1-4939-9170-9_11.
72. Vaughan-Jackson, A., Stodolak, S., Ebrahimi, K.H., Browne, C., Reardon, P.K., Pires, E., Gilbert-Jaramillo, J., Cowley, S.A., and James, W.S. (2021). Differentiation of human induced pluripotent stem cells to authentic macrophages using a defined, serum-free, open-source medium. Stem Cell Rep. *16*, 1735–1748. https://doi.org/10.1016/j.stemcr.2021.05.018.
73. van Wilgenburg, B., Browne, C., Vowles, J., and Cowley, S.A. (2013). Efficient, long term production of monocyte-derived macrophages from human pluripotent stem cells under partly-defined and fully-defined conditions. PLoS One *8*, e71098. https://doi.org/10.1371/journal.pone.0071098.
74. Washer, S.J., Perez-Alcantara, M., Chen, Y., Steer, J., James, W.S., Trynka, G., Bassett, A.R., and Cowley, S.A. (2022). Single-cell transcriptomics defines an improved, validated monoculture protocol for differentiation of human iPSC to microglia. Sci. Rep. *12*, 19454. https://doi.org/10.1038/s41598-022-23477-2.
75. Davis, S., Charles, P.D., He, L., Mowlds, P., Kessler, B.M., and Fischer, R. (2017). Expanding Proteome Coverage with CHarge Ordered Parallel Ion aNalysis (CHOPIN) Combined with Broad Specificity Proteolysis. J. Proteome Res. *16*, 1288–1299. https://doi.org/10.1021/acs.jproteome.6b00915.
76. Olie, C.S., Pinto-Fernández, A., Damianou, A., Vendrell, I., Mei, H., den Hamer, B., van der Wal, E., de Greef, J.C., Raz, V., and Kessler, B.M. (2023). USP18 is an essential regulator of muscle cell differentiation and maturation. Cell Death Dis. *14*, 231. https://doi.org/10.1038/s41419-023-05725-z.
77. Wu, T., Hu, E., Xu, S., Chen, M., Guo, P., Dai, Z., Feng, T., Zhou, L., Tang, W., Zhan, L., et al. (2021). clusterProfiler 4.0: A universal enrichment tool for interpreting omics data. Innovation. *2*, 100141. https://doi.org/10.1016/j.xinn.2021.100141.
78. Yu, G., Wang, L.G., Han, Y., and He, Q.Y. (2012). clusterProfiler: an R package for comparing biological themes among gene clusters. OMICS *16*, 284–287. https://doi.org/10.1089/omi.2011.0118.
79. Mellacheruvu, D., Wright, Z., Couzens, A.L., Lambert, J.P., St-Denis, N.A., Li, T., Miteva, Y.V., Hauri, S., Sardiu, M.E., Low, T.Y., et al. (2013). The CRAPome: a contaminant repository for affinity purification-mass spectrometry data. Nat. Methods *10*, 730–736. https://doi.org/10.1038/nmeth.2557.

STAR★METHODS

KEY RESOURCES TABLE

REAGENT or RESOURCE	SOURCE	IDENTIFIER
Antibodies		
Cleaved-IL-1β (Asp116) (D3A3Z) Rabbit mAb	Cell Signaling Technology	CAT# 83186; RRID: AB_2800010
IL-1β (D3U3E) Rabbit mAb	Cell Signaling Technology	CAT# 12703; RRID: AB_2737350
Caspase-1 (D7F10) Rabbit mAb	Cell Signaling Technology	CAT# 3866; RRID: AB_2069051
NLRP3 (D4D8T) Rabbit mAb	Cell Signaling Technology	CAT# 15101; RRID: AB_2722591
ASC(B-3)	Santa Cruz	CAT# sc-514414; RRID: AB_2737351
Monoclonal Anti-β-Actin antibody produced in mouse	Sigma-Aldrich	CAT# A5441; RRID: AB_476744
NEK7	Abcam	CAT# ab133514; RRID: AB_2877625
UCH-L1	Santa Cruz	CAT# sc-271639; RRID: AB_10714950
IRDye® 800CW Goat anti-Rabbit IgG Secondary Antibody	LI-COR Biosciences, Ltd.	CAT# 926-32211; RRID: AB_621843
IRDye® 800CW Goat anti-Mouse IgG Secondary Antibody	LI-COR Biosciences, Ltd.	CAT# 926-32210; RRID: AB_621842
IRDye® 680RD Goat anti-Mouse IgG Secondary Antibody	LI-COR Biosciences, Ltd.	CAT# 926-68070: RRID: AB_10956588
IRDye® 680RD Goat anti-Rabbit IgG Secondary Antibody	LI-COR Biosciences, Ltd.	CAT# 926-68071; RRID: AB_10956166
Goat anti-Rabbit IgG (H + L) secondary, Alexa Fluor 488-conjugated	ThermoFisher Scientific	CAT# A-11008; RRID: AB_143165
Goat anti-Mouse IgG (H + L) secondary, Alexa Fluor 488-conjugated	ThermoFisher Scientific	CAT# A-11001; RRID: AB_2534069
Bacterial and virus strains		
DH5α competent cells	Invitrogen	CAT# 18265017
Chemicals, peptides, and recombinant proteins		
L-Glutamine (200 mM)	Gibco	CAT# 25030149
Fetal Bovine Serum	Gibco	CAT# 10100147
Poly-D-Lysine	Gibco	CAT# A3890401
GlutaMAX Supplement	Gibco	CAT# 35050061
β-Mercaptoethanol	Sigma-Aldrich	CAT# M6250
RPMI-1640 Medium	Sigma-Aldrich	CAT# R0883
DME Medium - high glucose	Sigma-Aldrich	CAT# D5671
Suberic acid bis(N-hydroxysuccinimide ester)	Sigma-Aldrich	CAT# S1885
Sodium deoxycholate	Sigma-Aldrich	CAT# D6750
Ultrapure LPS, *E. coli* 0111:B4	InvivoGen	CAT# tlrl-3pelps
Cycloheximide solution	Sigma-Aldrich	CAT# C4859-1ML
Bafilomycin A1 from Streptomyces griseus	InvivoGen	CAT# B1793
16% Formaldehyde (w/v), Methanol-free	ThermoFisher Scientific	CAT# 28906
PhosSTOP phosphatase inhibitor	Roche	CAT# 4906837001
cOmplete^{TM}, Mini, EDTA-free Protease Inhibitor Cocktail	Roche	CAT# 11836170001
Trichloroacetic acid	Sigma-Aldrich	CAT# T6399
Pierce^{TM} DTT (Dithiothreitol)	ThermoFisher Scientific	CAT# 20290
Iodoacetamide	Sigma-Aldrich	CAT# A3221
Lipofectamine^{TM} 3000 Transfection Reagent	ThermoFisher Scientific	CAT# L3000001
Lipofectamine^{TM} 2000 Transfection Reagent	ThermoFisher Scientific	CAT# 11668030
Lipofectamine^{TM} RNAiMAX Transfection Reagent	ThermoFisher Scientific	CAT# 13778100
Sequencing-grade modified trypsin	Promega	CAT# V5111
Tween 20	Sigma-Aldrich	CAT# P1379-1L
Triton X-100	Sigma-Aldrich	CAT# T9284-500ML
Bromophenol blue	Sigma-Aldrich	CAT# B0126
Biotin	Sigma-Aldrich	CAT# B4501

(*Continued on next page*)

Continued

REAGENT or RESOURCE	SOURCE	IDENTIFIER
PMSF	G-Biosciences	CAT# 786-055
Hydrogen peroxide (H_2O_2), 30% (wt/wt)	Sigma-Aldrich	CAT# H1009-100ML
Trifluoroacetic acid	Sigma-Aldrich	CAT# 91707
Formic acid	Sigma-Aldrich	CAT# 56302
Biotin-phenol	Sigma-Aldrich	CAT# SML2135
Dynabeads^{TM} MyOne^{TM} Streptavidin T1	ThermoFisher Scientific	CAT# 65602
Sodium ascorbate	Sigma-Aldrich	CAT# A7631
Trolox	Sigma-Aldrich	CAT# 238813-5G
Sodium azide	Sigma-Aldrich	CAT# S2002
Trolox	Sigma-Aldrich	CAT# 238813-5G
Sodium azide	Sigma-Aldrich	CAT# S2002
MG132, Ready Made Solution	Sigma-Aldrich	CAT# M7449-1ML
TCEP	Gold Biotechnology	CAT# TCEP2
IGEPAL® CA-630	Sigma-Aldrich	CAT# I8896
Triton^{TM} X-100	Sigma-Aldrich	CAT# X100
Nuclease-Free Water (not DEPC-Treated)	ThermoFisher Scientific	CAT# AM9932
SYBR® Safe DNA gel stain	ThermoFisher Scientific	CAT# S33102
Q5® High-Fidelity 2X Master Mix	New England Biolabs	CAT# M0492S
Agarose	Sigma-Aldrich	CAT# A9539
Phosphoric acid	Sigma-Aldrich	CAT# 49685
SDS, 20% Solution, RNase-free	ThermoFisher Scientific	CAT# AM9820
Pierce^{TM} 3x DYKDDDDK Peptide	Thermo Scientific	CAT# A36806
RIPA Lysis and Extraction Buffer	Thermo Scientific	CAT# 89901
Benzonase® Nuclease	Millipore	CAT# E1014
IMP-1711-S	Panyain et al.[38]	N/A
6RK73	MedChemExpress	CAT# HY-133118
Critical commercial assays		
Caspase-Glo® 1 Inflammasome Assay	Promega	CAT# G9951
Pierce^{TM} BCA Protein Assay Kit	ThermoFisher Scientific	CAT# 23225
InstantBlue® Coomassie Protein Stain (ISB1L)	Abcam	CAT# ab119211
CyQUANT^{TM} LDH Cytotoxicity Assay	ThermoFisher Scientific	CAT# C20300
CellTiter 96® AQueous One Solution Cell Proliferation Assay (MTS)	Promega	CAT# G3582
Dynabeads^{TM} Co-Immunoprecipitation Kit	ThermoFisher Scientific	CAT# 14321D
Human IL-1 beta/IL-1F2 DuoSet ELISA	R&D Systems	CAT# DY201
Human IL-6 DuoSet ELISA	R&D Systems	CAT# DY206
Human TNF-alpha DuoSet ELISA	R&D Systems	CAT# DY210
LightCycler® 480 SYBR Green I Master	Roche	CAT# 04707516001
High-Capacity cDNA Reverse Transcription Kit	ThermoFisher Scientific	CAT# 4368814
RNeasy Mini Kit	Qiagen	CAT# 74104
Stop Solution 2N Sulfuric Acid	R&D Systems	CAT# DY994
DNeasy Blood & Tissue Kit	Qiagen	CAT# 69504
Deposited data		
Mass Spectrometry Proteomics Data	PRIDE	PXD045862
Experimental models: Cell lines		
THP-1	ATCC	CAT# TIB-202
HEK293T	ATCC	CAT# CRL-3216
Human PBMC	Clinical partners	N/A
KOLF2.1S hiPSC	HipSci project	N/A

(*Continued on next page*)

Continued

REAGENT or RESOURCE	SOURCE	IDENTIFIER
Flp-In T-REx 293 Cell Line	ThermoFisher Scientific	CAT# R78007
Recombinant DNA		
pOG44 Plasmid Vector	ThermoFisher Scientific	CAT# V600520
pcDNA5/FRT/TO GFP	Addgene	CAT# 19444
pcDNA5/FRT/TO APEX2-MyD88-Flag	Generated in our Lab (Backbone 19444)	N/A
pcDNA5/FRT/TO APEX2-NLRP3-Flag	Generated in this study (Backbone 19444)	N/A
pEGFP-C2-NLRP3	Addgene	CAT# 73955
pNLRP3 FLAG Full-length	Generated in this study (Backbone 73955)	N/A
pNLRP3 NACHT+ LRR- FLAG (140–1035)	Generated in this study (Backbone 73955)	N/A
pNLRP3 LRR only- FLAG (700–1035)	Generated in this study (Backbone 73955)	N/A
pNLRP3 Pyrin + NACHT- FLAG (1–700)	Generated in this study (Backbone 73955)	N/A
pNLRP3 NACHT only- FLAG (140–700)	Generated in this study (Backbone 73955)	N/A
lentiCRISPR v2	Addgene	CAT# 52961
lentiCRISPRv2 with UCH-L1-sgRNA#1	Generated in this study (Backbone lentiCRISPRv2)	N/A
lentiCRISPRv2 with UCH-L1-sgRNA#2	Generated in this study (Backbone lentiCRISPRv2)	N/A
lentiCRISPRv2 with UCH-L1-sgRNA#3	Generated in this study (Backbone lentiCRISPRv2)	N/A
Software and algorithms		
Prism, version 10.1.2	GraphPad	https://www.graphpad.com/scientific-software/prism/
Perseus, version 2.0.7.0	Tyanova et al.[65]	https://maxquant.net/perseus/
Image Studio Lite, version 5.2	LI-COR	https://www.licor.com/bio/image-studio-lite/
FiJi	Schindelin et al.[66]	https://imagej.net/software/fiji/
Cytoscape, version 3.9.0	Shannon et al.[67]	https://cytoscape.org
Columbus^{TM} Image Data Storage and Analysis system, version 2.9.0	Revvity	https://www.revvity.com
Illustrator	Adobe	https://www.adobe.com
Photoshop	Adobe	https://www.adobe.com
MaxQuant, Version v1.6.10.43	Tyanova et al.[68]	http://www.maxquant.org

RESOURCE AVAILABILITY

Lead contact

Further information and requests for resources and reagents should be directed to and will be fulfilled by the lead contact, Benedikt Kessler (benedikt.kessler@ndm.ox.ac.uk).

Materials availability

Plasmids generated in this study will be available from the lead contact upon request.

Data and code availability

- The mass spectrometry proteomics data have been deposited to the ProteomeXchange Consortium via the PRIDE partner repository[69,70] with the dataset identifier PXD045862.

- This study does not report original code.
- Any additional information required to reanalyse the data reported in this paper is available from the lead contact upon request.

EXPERIMENTAL MODEL AND SUBJECT PARTICIPANT DETAILS

Cell culture

THP-1 cells were cultured in 10% FBS (Gibco #10500-64) RPMI 1640 (Sigma) supplemented with 2% L-glutamine (G7513, Sigma-Aldrich), 0.05 mM β-mercaptoethanol (Sigma), and antibiotics (penicillin/streptomycin, Gibco). HEK293T cells were cultured in high glucose DMEM, supplemented with 10% FBS, and 2% L-glutamine. Flp-In T-REx 293 cell line (R78007, ThermoFisher) were cultured in high glucose DMEM, supplemented with 10% FBS, 2% L-glutamine, 100 μg/mL Zeocin (InvivoGen, ant-zn-1) and 15 μg/mL blasticidin (InvivoGen, ant-bl-1) at 37 °C in a humidified 5% CO2 atmosphere. The stably transfected Flp-In T-REx 293 cell lines (flag-NLRP3 and flag-NLRP3-APEX2) were cultured in the same medium and selected by 100 μg/mL hygromycin B (InvivoGen, ant-hg-1). 1 μg/mL tetracycline was added to induce the expression of flag-NLRP3 or flag-NLRP3-APEX2.

PBMC isolation and *in vitro* culture

To isolate the mononuclear cells, leukocyte cones (around 4 mL) were diluted in 25 mL RPMI medium before laid onto 15 mL LymphoPrep without disturbing the interface between LymphoPrep and the cone blood. Subsequently, it was centrifuged at 2000 rpm (400 g) at room temperature for 20 min. Lymphocytes, which form a thin layer of white film after the centrifuge, are transferred into a fresh 50 mL tube with a Graduated Pasteur Pipette and washed twice with RPMI medium. PBMCs were plated in 6-well plate at 1-2 × 10^7 cells/mL in 10 mL and allowed to adhere at 37°C for 4 h. Non-adherent cells were removed thorough washing with RPMI-1640.

hiPSC culture and differentiation to microglia

The KOLF2.1S hiPSC line used for this study was obtained with informed consent from all subjects, donors and/or their legal guardian(s) and with the approval of all the relevant institutions. All methods and experimental protocols were carried out in accordance with University of Oxford guidelines and regulations. hiPSC lines were generated previously as part of the HipSci project (REC ref. 09/H0304/77, covered under HMDMC 14/013 and REC ref. 14/LO/0345). KOLF2.1S was generated from the parental KOLF2-C1 line (https://hpscreg.eu/cell-line/WTSIi018-B-1) itself a clonal isolate of KOLF2 (https://hpscreg.eu/cell-line/WTSIi018-B) by correction of a heterozygous loss of function mutation ARID2 using CRISPR based homology repair by the Cellular Operations Gene Editing team at the Wellcome Sanger Institute.[71] hiPSC were cultured in OxE8 medium with daily media changes[72] on Geltrex (Gibco A1413302) coated tissue culture dishes and passaged with 0.5mM EDTA. hiPSC were differentiated into microglial precursors through the formation of embryoid bodies (EB)[73] by seeding 4 x 10^6 hiPSC per well of an Aggrewell 800 plate (STEMCELL Technologies, 34815) in EB medium (OxE8 supplemented with 50 ng/mL BMP4 (PeproTech PHC9534), 50 ng/mL VEGF (PeproTech PHC9394), and 20 ng/mL SCF (Miltenyi Biotec 130-096-695)). After differentiating in EB media for 6 days (with daily 50% media changes), 150 EB were transferred to T175 coated with 0.1% Gelatin containing differentiation media (X-VIVO 15 (Lonza BE02-060F), 1x GlutaMAX (Lifetech 25050-061), 50μM β-mercaptoethanol (LifeTech 31350-010), 100 ng/mL M-CSF (Gibco, PHC9501), 25 ng/mL IL-3 (Gibco, PHC0033). After 4–5 weeks of differentiation, microglial precursors shed into the media are harvested weekly by collection of supernatant and pelleting at 400 x g for 5 min. Microglial precursors are then resuspended in the final microglia maturation media ITMG (ADMEM/F12 (LifeTech, 12634-010), 1x GlutaMAX (Lifetech, 25050-061), 100 ng/mL IL-34 (PeproTech, 200-34-500), 50 ng/mL TGFβ-1 (PeproTech, 100-21C-250), 25 ng/mL M-CSF (Gibco, PHC0033), 10 ng/mL GM-CSF (Gibco, PHC2013), as previously described,[74] and differentiated to hiPSC-microglia for 14 days, with 50% media changes every 3 to 4 days. All differentiation steps are carried out at 37°C, 5% CO2.

METHOD DETAILS

Inflammasome activation assay

THP-1 cells were plated in a concentration of 1x10^6 cells/mL and incubated with 0.5 μM PMA for 4 h. After differentiation, PMA-containing media was replaced with fresh media. Experiments were carried out on the following day. Differentiated THP-1 cells were primed with LPS (1 μg/mL) for 4 h, followed by the treatment of PBS (mock) or 5 μM nigericin for 45 min. After stimulation, supernatants and cell lysates were collected separately, or combined together for immunoblotting analysis.

ASC speck oligomer crosslinking

PMA-differentiated THP-1 cells were primed with LPS (1 μg/mL) for 4 h, and then stimulated with nigericin (10μM) for 45 min. Cells were lysed on ice in Buffer A (20 mM HEPES-KOH, pH 7.5, 10 mM KCl, 1.5 mM $MgCl_2$, 1 mM EDTA, 1 mM EGTA, 320 mM sucrose, and protease inhibitor cocktail), and homogenized using a 21-gauge needle. The lysates were centrifuged at 1,800 rpm (300 g) for 8 min at 4°C. Supernatants were transferred to a new tube and diluted with 1 volume of CHAPS buffer (20 mM HEPES-KOH, pH 7.5, 5 mM MgCl2, 0.5 mM EGTA, 0.1% CHAPS, and protease inhibitor cocktail). The diluted lysates were then centrifuged at 5,000 rpm (2,400 g) provide g for 8 min to obtain the crude inflammasome-containing pellets. The pellets were washed with ice-cold

PBS twice, resuspended in CHAPS buffer, and then cross-linked at 37°C for 20 min by adding 2mM DSS (disuccinimidyl suberate, dissolved in DMSO). The reaction was quenched by adding SDS sample buffer and followed by Western blotting analysis.

Enzyme-linked immunosorbent assay (ELISA)

Human IL-1β (DY201, R&D Systems) and IL-6 (DY206, R&D Systems) production in the supernatants were detected by ELISA kit according to manufacturer's protocol. Plates were coated with diluted capture antibody in sterile PBS at room temperature overnight. On the following day, plates were washed three times with 200 μL/well wash buffer (0.05% Tween 20 in PBS, pH 7.2–7.4) before being blocked with 200 μL/well reagent diluent (1% BSA in PBS, pH 7.2–7.4, 0.2 μm filtered) at room temperature for a minimum of 1 h. After blocking, plates were washed three times and incubated with samples or standards (in reagent diluent) for 2 h at room temperature. After three washes of plates, 100 μL/well detection antibody (diluted in reagent diluent) was added to the wells and incubated for 2 h at room temperature. Plates were then washed three times and incubated with 100 μL/well Streptavidin-HRP for 20 min at room temperature, followed by another three washes and incubation with 100 μL/well substrate solution (1:1 mixture of Color Reagent A (H_2O_2) and Color Reagent B (Tetramethylbenzidine)) at room temperature. 20 min after the reaction, 50 μL/well stop solution (2 N H2SO4, DY994, R&D Systems) was added and mixed thoroughly to quench the reaction. The optical density of each well was determined at the wavelength of 450nm, and the relative concentration was calculated based on the standard curve, generated through a 3 parameter logistic curve fit using the data from standard samples.

TCA/DOC protein precipitation

Trichloroacetic acid (TCA)- deoxycholate (DOC) precipitation was commonly used to concentrate the proteins in supernatants and this method was adapted from André et al. Briefly, 8.5 μL of 2% Na-deoxycholate was added to 1 mL sample with a final concentration of 125 μg/mL. This mixture was incubated at room temperature for 15 min and 333 μL of 24% TCA (final concentration 6%) was added to the samples. Proteins were precipitated and centrifuged at 12,000 g for 30 min at 4°C. Supernatant was carefully removed and the pellets were washed once with acetone to remove excessive TCA before another centrifuge at 12,000 g for 5 min. After removing the supernatants, the resulting pellets were solubilised in loading buffer and subjected to immunoblotting analysis.

Cytotoxicity and cell viability assay

Relevant cells were treated as indicated, and the cytotoxicity was detected using CyQUANT LDH Cytotoxicity Assay (Invitrogen) according to manufacturer's instruction. Briefly, 50 μL of each sample supernatant was transferred to 96-well flat-bottom plate in triplicate wells, and then, 50 μL of premixed reaction buffer was added to each well. The plate was incubated for 30 min at room temperature before addition of 50 μL/well stop solution. The optical density of each well was measured at the wavelength of 490nm and 680nm (680 nm absorbance was used as background), and the cytotoxicity (% LDH release) was calculated according to manufacturer's protocol.

Cell viability was measured using CellTiter 96 AQueous One Solution Cell Proliferation Assay (MTS, Promega). Briefly, 20μL of CellTiter 96 AQueous One Solution Reagent was added to each well containing samples in 100 μL of culture medium. The plate was then incubated for a minimum of 1h at 37°C. The absorbance of each well was measured at the wavelength of 490nm, and the cell viability was calculated according to manufacturer's protocol.

Caspase-1 activity bioluminescent assay

Relevant cells were treated as indicated, and the caspase-1 activity in the culture medium (supernatant) was measured using Caspase-Glo 1 Inflammasome Assay (Promega) according to manufacturer's instruction. Briefly, Caspase-Glo 1 Reagent was prepared through resuspension of Z-WEHD substrate using Caspase-Glo 1 buffer, and the addition of MG132 inhibitor to a final concentration of 60 μM. Afterward, 50 μL of cell culture medium was transferred to the 96-well plate, followed by adding 5 μL Caspase-Glo 1 Reagent. The contents of the wells were thoroughly mixed and incubated at room temperature for at least 1 h for the signal to be stable. Subsequently, the luminescence value was measured using multi-mode microplate reader FLUOstar Omega (BMG LABTECH) according to manufacturer's instruction.

Immunoprecipitation

Cells were washed with ice-cold PBS for two times, and then lysed in Pierce IP lysis buffer (25 mM Tris-HCl pH 7.4, 150 mM NaCl, 1% NP-40, 1 mM EDTA, 5% glycerol, PhosSTOP phosphatase inhibitor and cOmplete Protease Inhibitor Cocktail). Lysates were incubated on ice for 10 min with periodic mixing, and then clarified at 13,000 g for 10 min at 4°C to remove the cell debris. Pre-cleared lysates were incubated with anti-FLAG M2 Magnetic Beads at room temperature for 30 min. After three times of washes with TBS, the proteins bound by the anti-flag antibody were pulled down and 3X FLAG peptide was added for elution. Both the whole cell lysates and the pull-down samples are subjected to immunoblotting analysis.

Transient transfection

For DNA plasmids: Cells were grown in 6-well plates and Lipofectamine 3000 Transfection Reagent (L3000001, ThermoFisher UK) was used to transfect the cells following the manufacturer's instructions. The concentration of plasmids used was indicated in each experiment. For siRNA transfection experiments: Cells were grown in 6-well plates and RNAimax transfection reagent (Invitrogen, 13778-150) was used following the manufacturer's protocol. A final concentration of 10 nM of the following Silencer select siRNAs were used: control siRNA (4390844), si-NLRP3 (s41554) and si-UCH-L1 (s14616).

Construction of plasmids

The full list and descriptions of all primers and plasmids used in this study can be found in key resources table. For the generation of NLRP3-APEX2, NLRP3-Flag, NEBuilder HiFi DNA Assembly (NEB: E5520S) was used following manufacture protocol. Primers were designed using the NEBuilder Assembly Tool. NLRP3 ORF was initially amplified from the pEGFP-C2-NLRP3. Then, pcDNA5/FRT/TO APEX2-MyD88-Flag was PCR amplified and assembled together. The successful clones were confirmed using both PCR and DNA sequencing. Finally, the expression plasmids for NLRP3 domains were generated using the Q5 Site-Directed Mutagenesis Kit (NEB: E0554S) following manufacture protocols. We used as a template the GFP- NLRP3 plasmid (Addgene), we initially replace GFP with Flag. Finally, different domains were deleted to generate the successful plasmids. The successful clones were confirmed using both PCR and DNA sequencing.

Generation of stable cell line

The Flp-In T-Rex 293 stable cell lines (flag-NLRP3 and flag-NLRP3-APEX2) were generated using Lipofectamine 3000 following manufacture protocol in a 6-well plate. The cells were transfected with both the expression plasmid and the plasmid pOG44 in a ratio of 1:9. Cells were split the following day and transferred in a 100mm dish. After 8 h, 300 μg/mL hygromycin B was added into the medium for selection.

sgRNA design, lentivirus production and transduction

Non-targeting control (NTC) and UCH-L1-targeting sgRNA sequences were designed using CRISPick tool (https://portals.broadinstitute.org/gppx/crispick/public). To clone the target sequences into the lentiCRISPRv2 backbone (one vector system), two oligos containing the target sequences were synthesized (Sigma) and inserted into the digested lentiviral construct. sgRNA sequences are as follows: UCH-L1-sgRNA#1: 5′-ACTTCATGAAGCAGACCATT-3'; UCH-L1-sgRNA#2: 5′- AATCGGACTTATTCACGCAG-3'; UCH-L1-sgRNA#3: 5′- AAGACAAACTGGGATTTGGT-3'. HEK293T cell lines were seeded at 40% confluency and transfected with pMD2G, psPAX2 and the above lentiCRISPRv2 plasmids using lipofectamine 2000 following manufacturer's instructions. After incubation for two days, supernatants were collected and filtered by 0.45μm filter, followed by ultracentrifuge to obtain concentrated viral particles.

PCR and agarose gel electrophoresis

Genomic DNAs were extracted using the DNeasy Blood and Tissue Kits (QIAGEN, Cat. No 69504) following the manufacturer's protocol. PCR was subsequently performed to confirm the knockout efficiency. The PCR reactions consisted of a 25 μL mixture containing forward and reverse primers (1.25 μL each, Forward primer: 5′-CATTCTGAGATGTAAAAACGCTTTT-3'; Reverse primer: 5′-CTTAGGATGGCTGGCCTCAAAACCCA-3′), and Q5 High-Fidelity 2x master mix. The PCR conditions involved an initial denaturation at 98°C for 3 min, followed by 35 cycles of denaturation at 98°C for 10 s, annealing at 59°C for 30 s, and extension at 72°C for 20 s. The extension phase continued for an additional 5 min at 72°C, and the samples were held overnight at 4°C. Subsequently, the PCR products were subjected to gel electrophoresis on a 4% agarose gel with SYBR safe, running at 100V for 2 h.

Biotin-phenol proximity labeling and biotinylated proteins capture

This method was adapted from that previously reported by Stephanie et al. 5×10^6 Flp-In T-Rex HEK293 stable cells were induced with 1 μg/mL tetracycline overnight. The next day cells were incubated with medium containing 500 μM biotin-phenol for 30 min at 37°C under 5% CO2. Afterward, a final concentration of 1 mM H_2O_2 was added and incubated for 40 s. The reaction was then quenched by the addition of quenching buffer (10 mM sodium ascorbate, 10 mM sodium azide, 5mM Trolox in DPBS). Subsequently, cells were washed with quenching buffer for three times, PBS for two times and then lysed with RIPA lysis buffer containing 1 mM PMSF, 5 mM Trolox, 10 mM sodium azide, 10 mM sodium ascorbate, PhosSTOP phosphatase inhibitor and cOmplete Protease Inhibitor Cocktail. Samples were then briefly sonicated and centrifuged at 10,000 g for 10 min at 4°C to remove cell debris. For streptavidin pull-down experiments, Dynabeads MyOne Streptavidin T1 was prepared and washed with RIPA lysis buffer twice. The cleared lysate was applied to the magnetic beads and at RT for 1 h. Afterward, the beads were washed for two times with RIPA lysis buffer, once with 1M KCL, 0.1 M Na_2CO_3 and 2 M Urea (in 10 mM Tris-HCL, pH 8) and finally twice with RIPA buffer again. For western blot analysis, biotinylated proteins were eluted using 60 μL of 3×loading buffer supplemented with 2 mM biotin and 20 mM DTT by boiling (98°C) for 10 min. For Mass spectrometry analysis, an on-beads digestion protocol was used as described below. Samples were denatured in 8 M Urea (in 100 mM triethylammonium bicarbonate buffer (TEAB)) and incubated at room temperature for 30 min. Afterward, the samples were reduced with 10 mM tris(2-carboxyethyl)phosphine (TCEP) for at room temperature 30 min. Samples were alkylated by the addition of iodoacetamide (final concentration 50 mM) and incubated at room temperature for 30 min. The reaction was quenched by adding DTT (final concentration 20 mM), and the urea concentration were diluted down to 1.5 M by adding TEAB. Biotinylated proteins were digested through the incubation with trypsin (1 μg trypsin per 20 μL streptavidin beads) overnight at 37°C. Following the trypsinization, samples were desalted using the C18 solid phase cartridge (Sep-Pak, Waters) according to the manufacturer's protocol. Purified peptide eluates were dried down in the speed-vac, re-suspended in buffer A (98% MilliQ-H_20, 2% CH_3CN and 0.1% trifluoroacetic acid - TFA) and stored at $-20^\circ C$ until further analysis.

Affinity-purification mass spectrometry (AP-MS)

In the AP-MS experiment, four distinct experimental setups were employed: 1) no tetracycline and treated with DMSO, 2) no tetracycline and treated with nigericin, 3) tetracycline added and treated with DMSO, and 4) tetracycline added and treated with nigericin. Each setup was replicated three times biologically to ensure the reliability of the results. 1×10^7 HEK293 FLAG-NLRP3 Flp-In T-Rex stable cells were induced with 1 μg/mL tetracycline overnight. The next day cells were incubated with Nigericin (10μM) or DMSO for 90 min at 37°C under 5% CO_2. Cells were washed with ice-cold PBS for five times, and then lysed in Pierce IP lysis buffer (25 mM Tris-HCl pH 7.4, 150 mM NaCl, 1% NP-40, 1 mM EDTA, 5% glycerol), supplemented with PhosSTOP phosphatase inhibitor and cOmplete Protease Inhibitor Cocktail. Lysates were incubated on ice for 10 min with periodic mixing, and then clarified at 13,000 g for 10 min at 4°C to remove the cell debris. Pre-cleared lysates were incubated with anti-FLAG M2 Magnetic Beads at 4°C overnight. The next day beads were washed 3 times with wash buffer, followed by the elution using 100 μL of 150 ng/μL 3x FLAG peptide in PBS after 30 min of incubation at room temperature.

Subsequently, the samples were subjected to the S-Trap micro spin column. Briefly, SDS was added to the samples to achieve a final concentration of 5%, followed by reduction with DTT (22 mM) and incubation at 95°C for 10 min. Samples were then alkylated with 40 mM Iodoacetamide and incubated in dark at room temperature for 30 min. To acidify the samples, 12% aqueous phosphoric acid was added to achieve a final concentration of 1.2% phosphoric acid. 7 volumes of protein binding buffer (90% aqueous methanol containing 100 mM TEAB, pH 7.5) were added to each sample and thoroughly mixed. The samples were then transferred into S-Trap microcolumns and centrifuged at 4,000 g until all SDS lysate/S-Trap buffer had passed through the columns, repeating this step until all sample was added. Afterward, the captured proteins were washed by 150 μL of S-Trap protein binding buffer and centrifuged at 4,000 g for 3 min, repeating the wash four times. Following washing, 40 μL of digestion buffer (80 ng/μL trypsin in 50 mM TEAB) was added, and the samples were incubated at 37°C overnight. The next day, the digested peptides were eluted using 40 μL each of 50 mM TEAB and 0.2% aqueous formic acid, with samples centrifuged at 4,000 g for 4 min after each elution. Finally, hydrophobic peptides were eluted by adding 40 μL of 50% acetonitrile containing 0.2% formic acid. The three eluates were pooled together and dried in a SpeedVac at room temperature for 4 h.

Mass spectrometry analysis

An Orbitrap Fusion Lumos Tribid mass spectrometer (Thermo Fisher Scientific) coupled to an Ultimate 3000 UHPLC (Thermo Fischer Scientific) platform was used to analyze the purified tryptic peptides by liquid chromatography-tandem mass spectrometry (LC-MS/MS) as described previously.[75] In brief, 10% of tryptic peptides (~200 ng) were loaded onto a trap column (PepMapC18; 300μm × 5mm, 5μm particle size, Thermo Fischer) and separated on a 50 cm EasySpray column (ES803, Thermo Fischer) using a 60 min linear gradient ranging from 2% to 35% buffer B (A: 5% DMSO, 0.1% formic acid; B: 5% DMSO, 0.1% formic acid in acetonitrile) at a flow rate of ~250 nL/min. Eluted peptides were then subjected to electrospray ionisation (ESI) and directed into an Orbitrap Fusion Lumos Tribrid mass spectrometer (instrument control software v3.3). Data were acquired in data-dependent mode (DDA), with the advance peak detection (APD) feature enabled. Survey scans were acquired in the Orbitrap at 120 k resolution over an m/z range 400–1500, AGC target of 4e5 and S-lens RF of 30. Fragment ion spectra (MS/MS) were obtained in the Ion trap (rapid scan mode) with a Quad isolation window of 1.6, 40% AGC target and a maximum injection time of 35 ms, with HCD activation and 28% collision energy. Raw MS files were analyzed using MaxQuant software (v1.6.10.43) using label-free quantitation (LFQ) as described previously.[76] In brief, raw MS files were searched against the UniProtKB human sequence database (UP000005640, 79,038 human sequence entries). The following parameters were set to perform label free quantification: Modifications were set on Carbamidomethyl (C) as fixed and Oxidation (M) and Deamidation (NQ) as variable and a maximum of two missed cleavages were allowed. Match between runs function was used.

RNA extraction and real time reverse transcription (RT)-PCR

Total RNA was isolated with the TRIzol reagent (Sigma Aldrich) according to the manufacturer's instructions. The nucleic acid concentration was measured with the NanoDrop2000 (NanoDrop Technologies, Inc.). Complementary DNA (cDNA) was synthesized from 1.5 μg of total RNA with the High-Capacity cDNA Reverse Transcription Kit (Applied Biosystems, USA). Quantitative real-time PCR (RT-qPCR) was performed using the LightCycler 480 SYBR Green I Master kit and LightCycler 480 PCR System (Roche, Switzerland) according to the manufacturer's instructions. The Delta-Ct method was used to calculate the relative RNA expression levels.

Pathway enrichment analysis

Filtered proximity proteomes (SAINT probability >0.8, FC-A $\geq$ 1) either in DMSO control or nigericin activated samples were imported into the STRING database search portal (version 11.5, Szklarczyk et al., 2021; von Mering et al., 2003), and the top 20 retrieved terms were plotted with both strength (Log10 [observed/expected]) and false discovery rate (FDR) (interaction score $\geq$0.7). Terms were clustered through the similarity of enrichment strength patterns across the four groups and the results were further visualized using clusterProfiler 4.0 [77,78].

PPIs network construction

Differentially enriched proteins under unstimulated or stimulated condition that passed the filtering criteria (log2[FC] ≥ 0.5 or ≤ -0.5, FDR ≤ 0.05) were separately uploaded to the STRING portal, and physical subnetwork type was chosen to extract the physical (direct) protein-protein associations from the databases. Active interaction sources, including text mining, experiments, and databases, and an interaction score >0.7 (high confidence interaction) were applied to construct the PPI networks. Markov clustering algorithm (MCL) was used to group the interaction subnetworks with the inflation value of 3.0, resulting in 13 clusters for the stimulated condition and 18 clusters for the unstimulated condition.

QUANTIFICATION AND STATISTICAL ANALYSIS

SAINT probabilistic scoring for NLRP3 APEX2 PL-MS and AP-MS data

The computational tool, SAINTexpress[24]- an updated version of the "Significance Analysis of INTeractome (SAINT)," was utilised to allocate confidence scores to the proximity labeling and AP-MS data. This analysis was conducted via the online Contaminant Repository for Affinity Purification platform at www.crapome.org.[79]

STATISTICS AND REPRODUCIBILITY

All data are presented as mean ± standard deviation (SD). We performed statistical analysis using one-way ANOVA to compare various treatments against a single control group. A two-tailed, unpaired student's t test was used for the comparison between two groups. Unless stated, all quantitative experiments were performed in triplicates and average with SD reported. All statistical analyses were conducted using GraphPad Prism 9 software. Detailed statistical information and sample sizes are provided in the figure legends. $^{*}p < 0.05$, $^{**}p < 0.01$, $^{***}p < 0.001$, $^{****}p < 0.0001$.

Cell Reports, Volume *43*

Supplemental information

Proximity proteomics reveals UCH-L1 as an essential regulator of NLRP3-mediated IL-1β production in human macrophages and microglia

Zhu Liang, Andreas Damianou, Iolanda Vendrell, Edward Jenkins, Frederik H. Lassen, Sam J. Washer, Athina Grigoriou, Guihai Liu, Gangshun Yi, Hantao Lou, Fangyuan Cao, Xiaonan Zheng, Ricardo A. Fernandes, Tao Dong, Edward W. Tate, Elena Di Daniel, and Benedikt M. Kessler

Figure S1

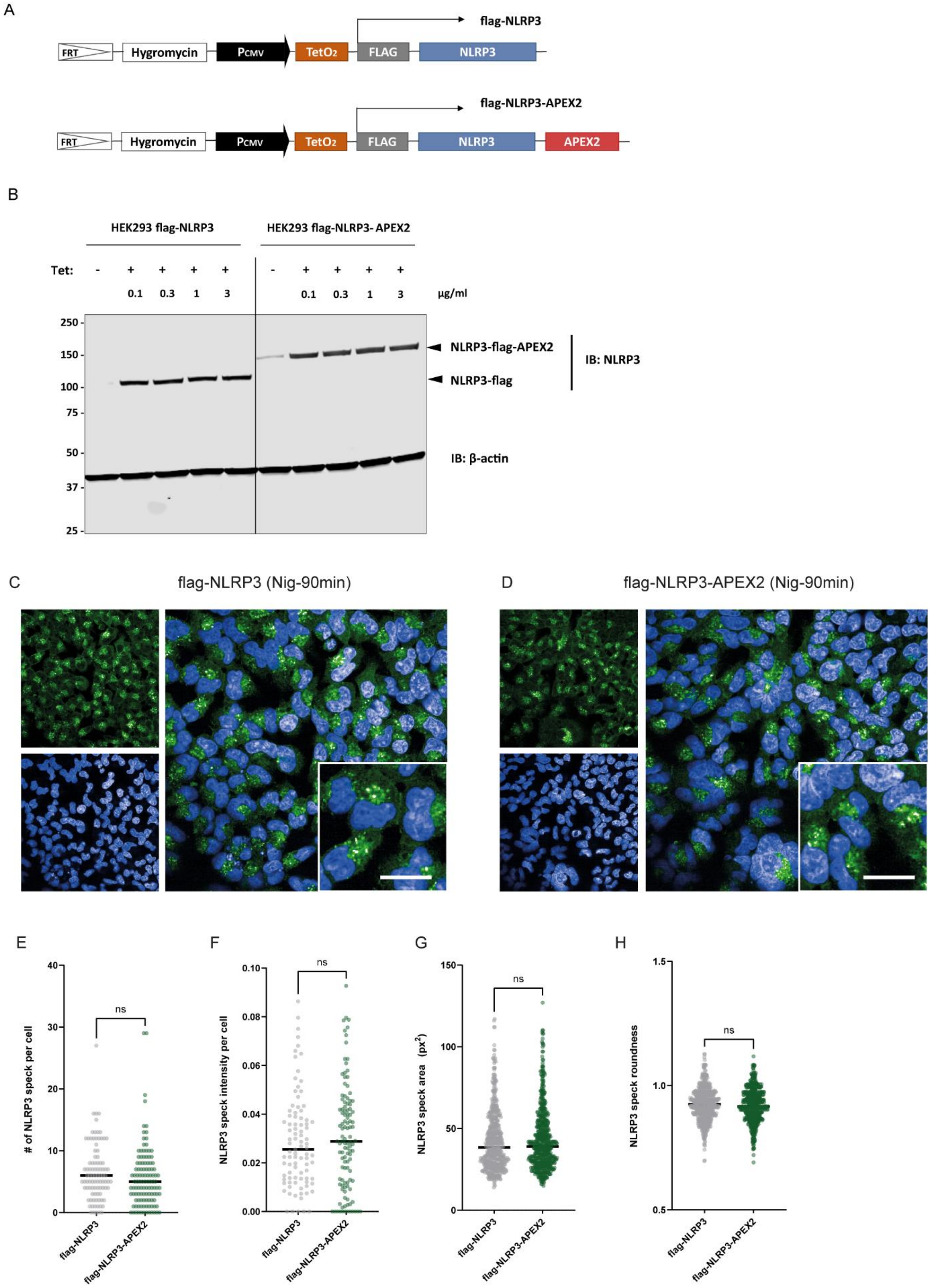
A
flag-NLRP3
FRT
Hygromycin
PCMV
TetO2
FLAG
NLRP3
flag-NLRP3-APEX2
FRT
Hygromycin
PCMV
TetO2
FLAG
NLRP3
APEX2
B
HEK293 flag-NLRP3
HEK293 flag-NLRP3- APEX2
Tet:
-
+
+
+
+
-
+
+
+
+
0.1
0.3
1
3
0.1
0.3
1
3
µg/ml
250
150
100
75
50
37
25
NLRP3-flag-APEX2
NLRP3-flag
IB: NLRP3
IB: β-actin
C
flag-NLRP3 (Nig-90min)
D
flag-NLRP3-APEX2 (Nig-90min)
E
# of NLRP3 speck per cell
40
30
20
10
0
ns
flag-NLRP3
flag-NLRP3-APEX2
F
NLRP3 speck intensity per cell
0.10
0.08
0.06
0.04
0.02
0.00
ns
flag-NLRP3
flag-NLRP3-APEX2
G
NLRP3 speck area (px²)
150
100
50
0
ns
flag-NLRP3
flag-NLRP3-APEX2
H
NLRP3 speck roundness
1.5
1.0
0.5
ns
flag-NLRP3
flag-NLRP3-APEX2

Figure S1. Construction of flag-NLRP3 and flag-NLRP3-APEX2 HEK293 stable cell line

(A) Schematic of Flag-NLRP3 and Flag-NLRP3-APEX2 constructs. (B) Both the flag-NLRP3 and flag-NLRP3-APEX2 Flp-In T-Rex HEK293 stable cell lines were treated with tetracycline at indicated concentrations (0.1-3 μg/mL). 24 hours after induction, cell lysates were collected for immunoblotting analysis. (C-D) Representative confocal images of flag-NLRP3 (C) or flag-NLRP3-APEX2 (D)-expressing HEK293 stable cell lines treated with 10μM Nigericin for 90 min. Cells were stained with anti-flag antibody (green) and DAPI (blue). Scale bars, 10 μm. (E-H) Quantitative analysis of NLRP3 puncta in flag-NLRP3 (n = 602) or flag-NLRP3-APEX2 (n = 642)-expressing HEK293 stable cell lines treated with 10μM Nigericin for 90 min using Columbus Image Data Analysis System.

Figure S2

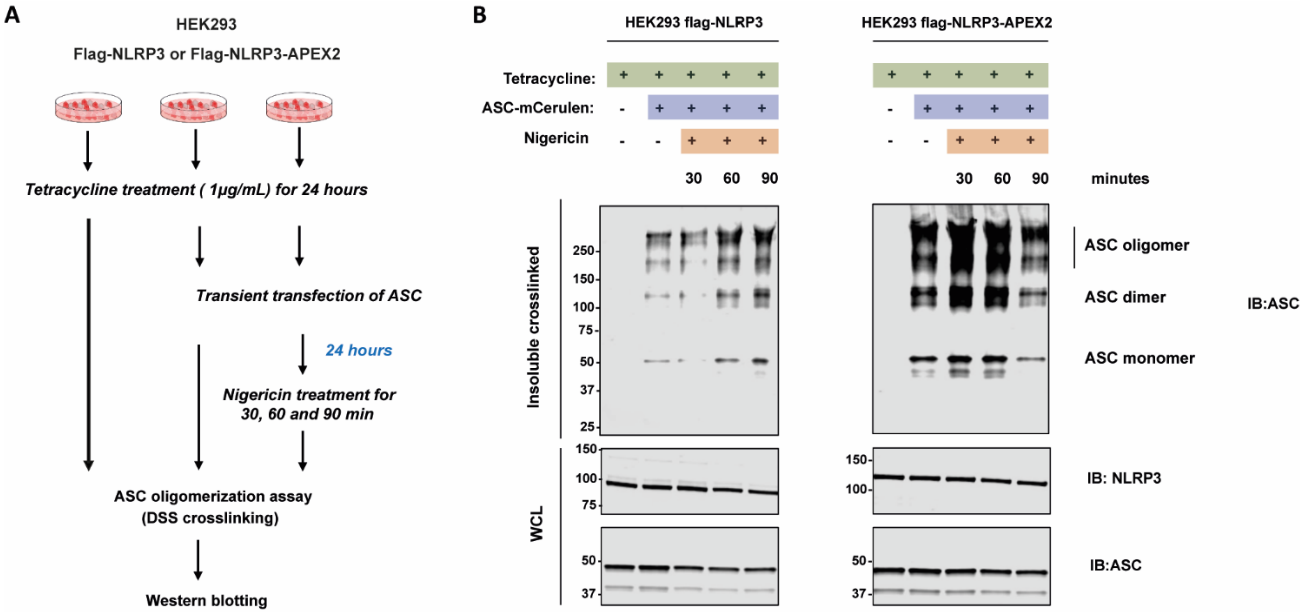

Figure S2. Reconstituted NLRP3 induces ASC oligomerization in HEK293 cell lines

(A) Schematic of the ASC oligomerization assay in Flp-In T-Rex HEK293 stable cell lines. (B) Immunoblot of DSS-crosslinked ASC oligomers in the lysates from flag-NLRP3 and flag-NLRP3-APEX2 HEK293 stable cell lines, treated with tetracycline overnight, transfected with ASC mCerulean, and followed by the treatment with nigericin (10μM) for the indicated time.

Figure S3

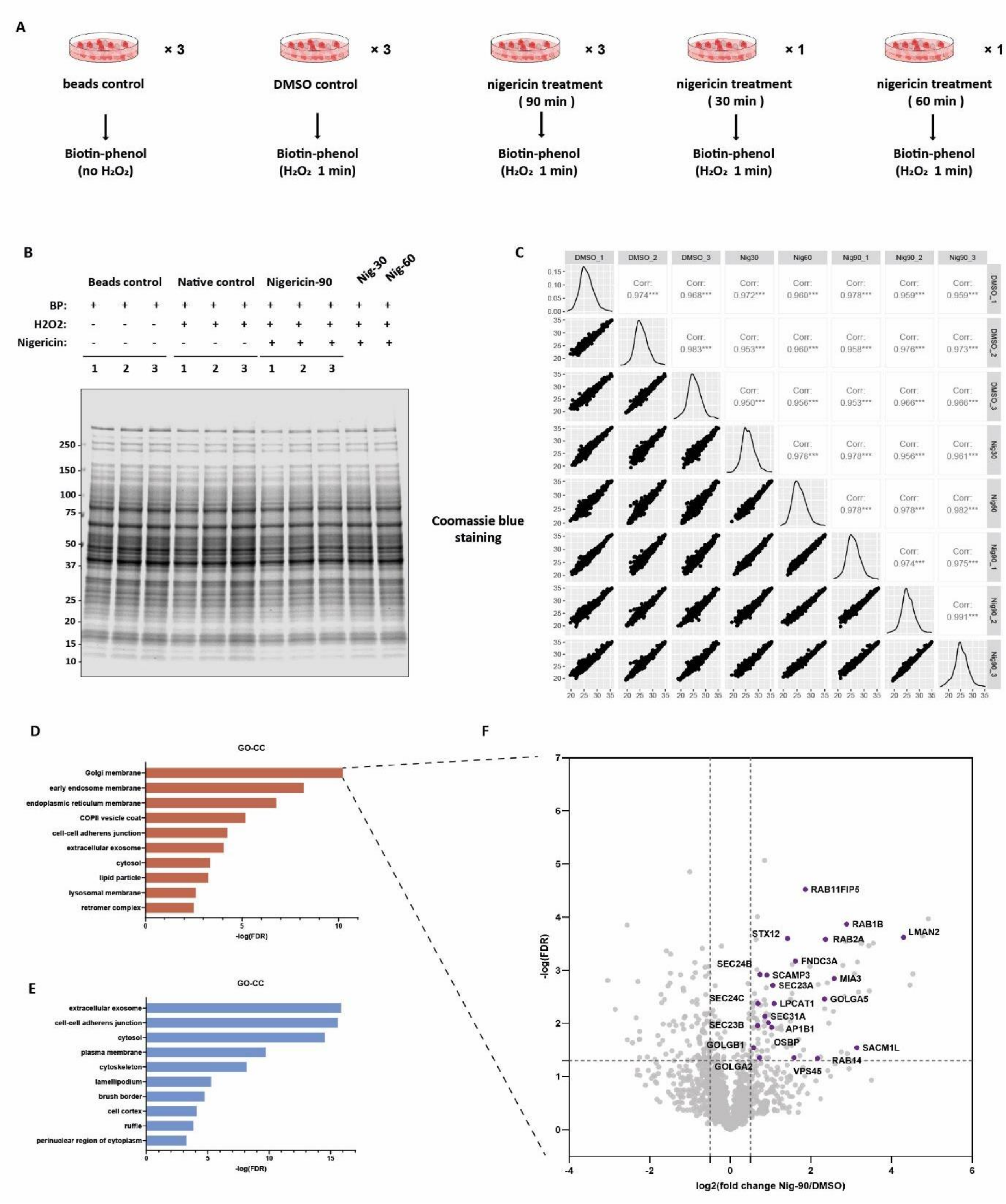

Figure S3. Tracing NLRP3 translocation using NLRP3-APEX2 proximity labelling

(A) Scheme of the experimental design and procedures of NLRP3-APEX2 proximity labelling. (B) Coomassie blue staining of whole-cell lysates from HEK293 Flp-In T-Rex NLRP3-APEX2 cells, treated as indicated with tetracycline, biotin-phenol, H_2O_2, and nigericin. (C) Pearson correlation matrix heatmap of the biotinylated proteome profiling. This analysis confirms high reproducibility in protein relative abundance measurements. (D-F) Bar graph showing the top 10 gene ontology-cellular component (GO-CC) terms of the proteins enriched in nigericin-stimulated state (nigericin treatment for 90 min) (D) and unstimulated state (DMSO treatment for 90 min) (E) respectively. (F) The 24 proteins that belong to the Golgi membranes term are shown and coloured as purple in the volcano plotting.

Figure S4

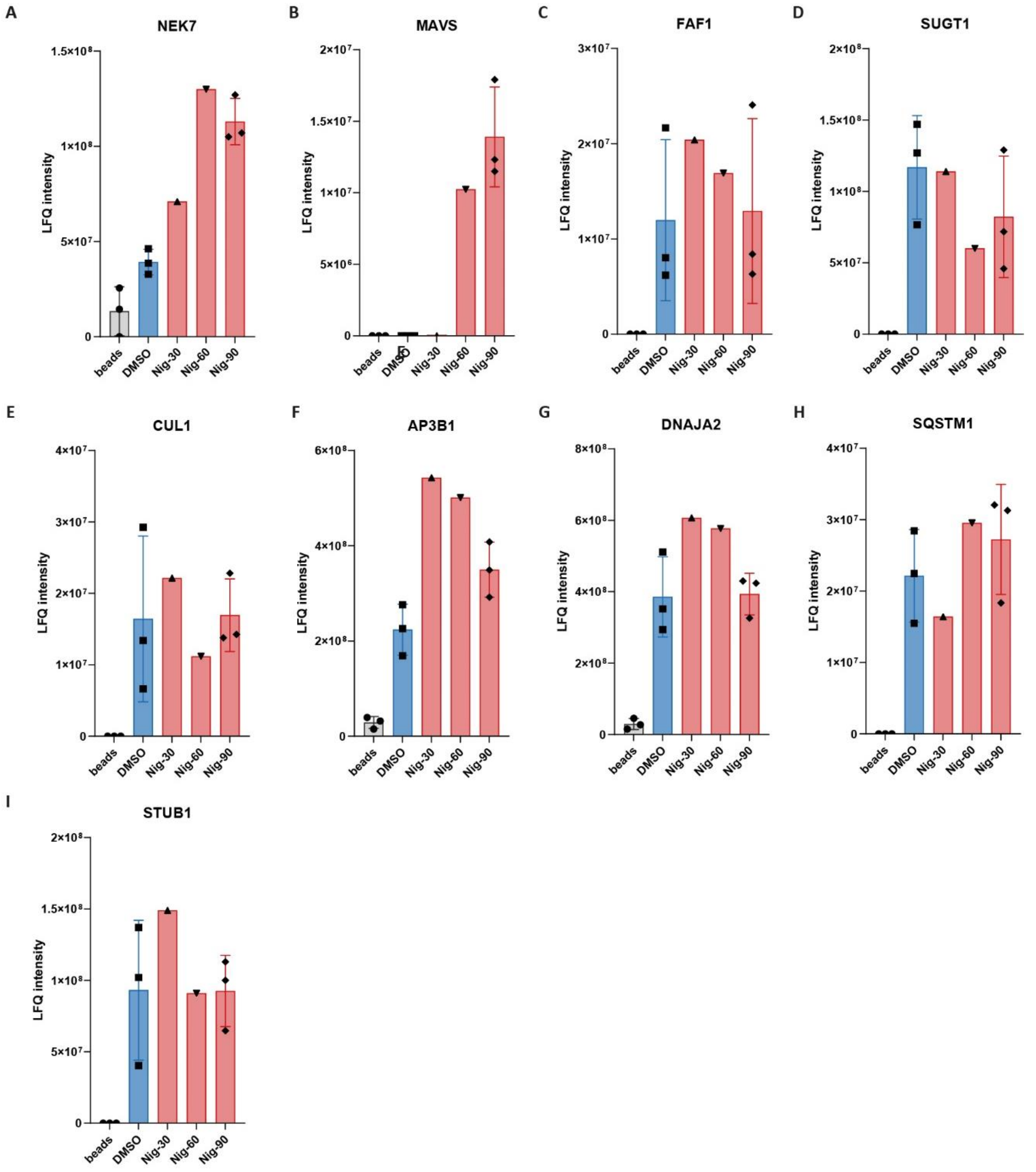

Figure S4 | APEX2 proximity labelling identifies known NLRP3-interacting proteins during NLRP3 activation downstream of potassium efflux

(A-I) The raw LFQ Intensity values of the APEX2 NLRP3 proximity labelling from all the known NLRP3-interacting proteins identified in our experiment. An average value of 3 independent experiments is presented for DMSO and Nig-90 whereas for Nig-30 and Nig-60 just a single experiment. Error bars show the standard deviation of the mean.

Figure S5

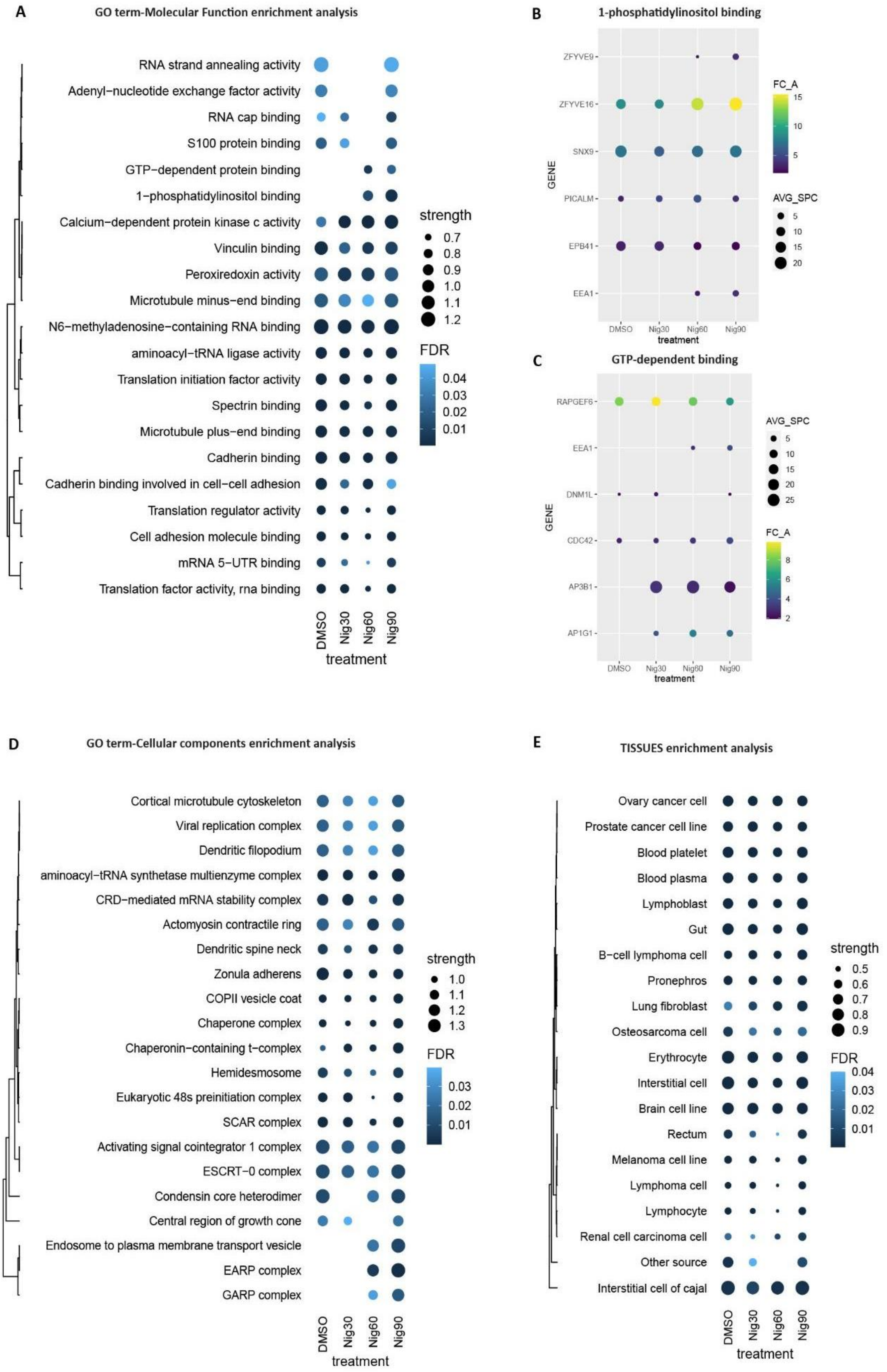

Figure S5. Functional analysis of the NLRP3 proximal proteins during inflammasome activation

(A, D, E) Dot plots displaying the GOBP (A), GOCC (D) and TISSUE (E) enrichment analysis of high confidence NLRP3 proximal proteins upon nigericin stimulation for different timepoints as indicated. (B, C) Dot plots showing the average spectral counts (AVG_SPC) and fold change (FC_A) of NLRP3 proximal proteins enriched in the GOMF term 1-phosphatidylinostol binding (B) and GTP-dependent binding (C) respectively.

Figure S6

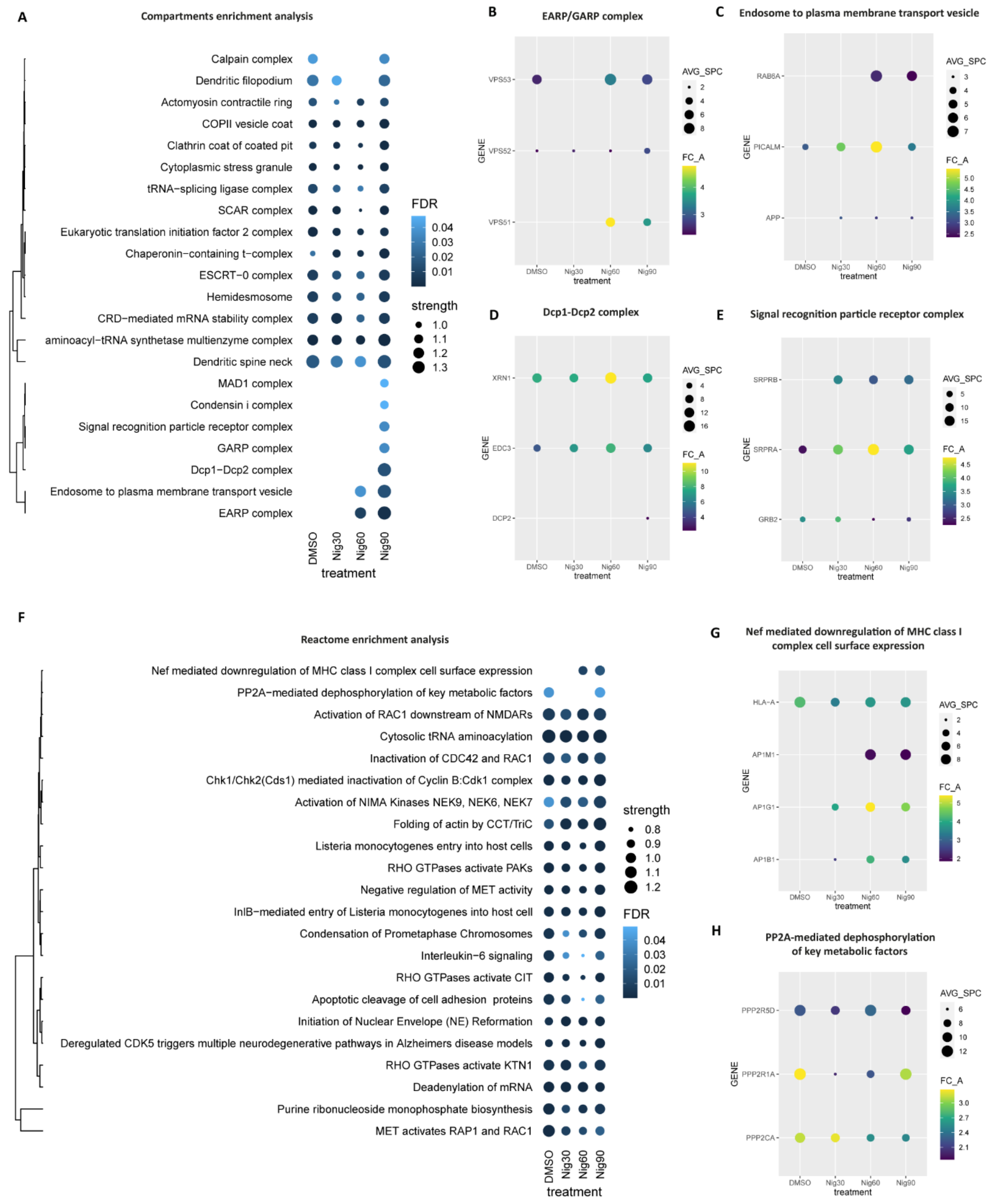

Figure S6. Functional analysis of the NLRP3 proximal proteins during inflammasome activation (A, D) Dot plots displaying the Compartments (A) and Reactome (F) enrichment analysis of high confidence NLRP3 proximal proteins upon nigericin stimulation for different timepoints. (B-E, G-H) Dot plots showing the average spectral counts (AVG_SPC) and fold change (FC_A) of NLRP3 proximal proteins enriched in the term EARP/GARP complex (B), Endosome to plasma membrane transport vesicle (C), Dcp1-Dcp2 complex (D) and Signal recognition particle receptor complex (E), Nef mediated downregulation of MHC class I complex cell surface expression (G), PP2A-mediated dephosphorylation of key metabolic factors (H) respectively.

Figure S7

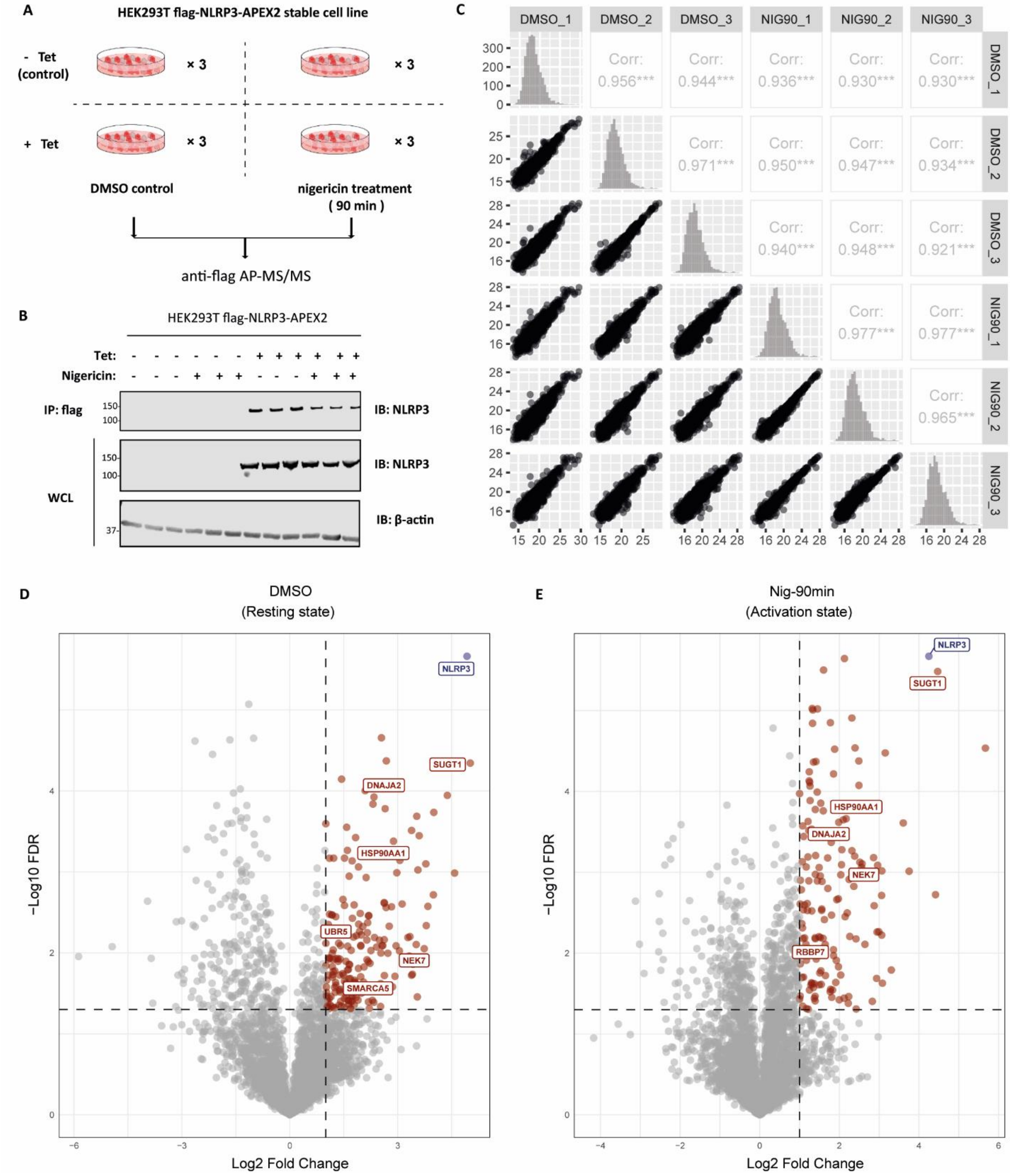

Figure S7. NLRP3 interactome determined by AP-MS

(A) Schematic of the NLRP3 AP-MS experiment design. (B) Stable HEK293 cells expressing flag-NLRP3-APEX2 were incubated with tetracycline overnight. Subsequently, they were treated with nigericin for 90 min as specified. Flag-tagged NLRP3-APEX2 fusion was then isolated using an anti-flag antibody and subjected to immunoblotting with the indicated antibodies. (C) Pearson correlation matrix heatmap of the NLRP3 AP-MS proteomic profiling. (D-E) Volcano plot depicting the fold change for relative protein quantification of NLRP3 AP-MS samples between unstimulated (DMSO) or stimulated conditions (nigericin-90min) and the corresponding beads control. Data are shown as means of three independent samples. Non-adjusted unpaired two-tailed t-test was applied to the statistical analysis.

Figure S8

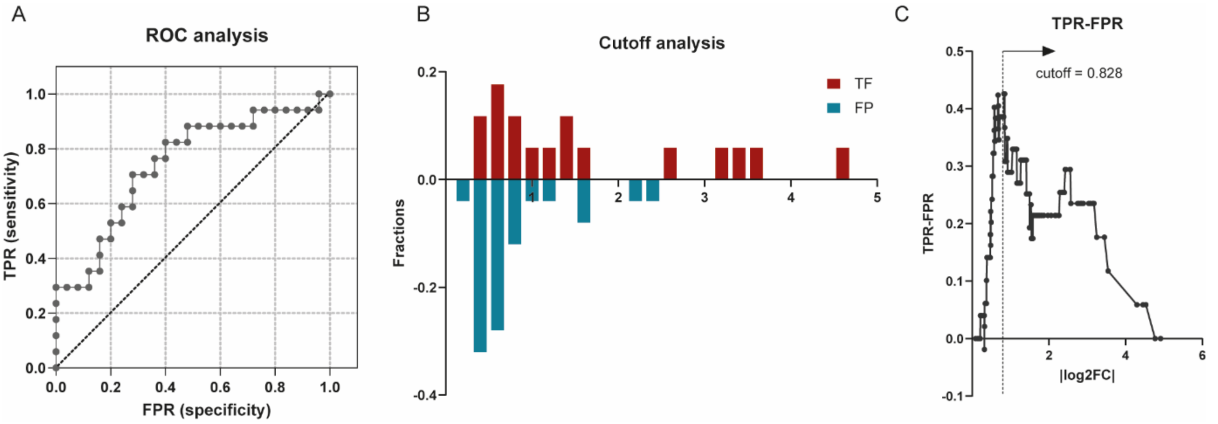

Figure S8. Cut-off analysis for the stimulation-dependent NLRP3 proximity proteome

(A) Receiver operating characteristic (ROC) curve of NLRP3-APEX2-PL for the prediction of NLRP3-interacting partners. (B) Distribution of TP and FP fractions across bins of log2 |FC(Nig-90min/DMSO)|. (C) The cut-off point was determined where the difference between the true positive rate and the false positive rate (TPR-FPR) was maximized. True positive includes NLRP3-interacting proteins in BioGRID and those captured by AP-MS, while false positive includes nucleolus and secreted proteins that are annotated by GO-CC.

Figure S9

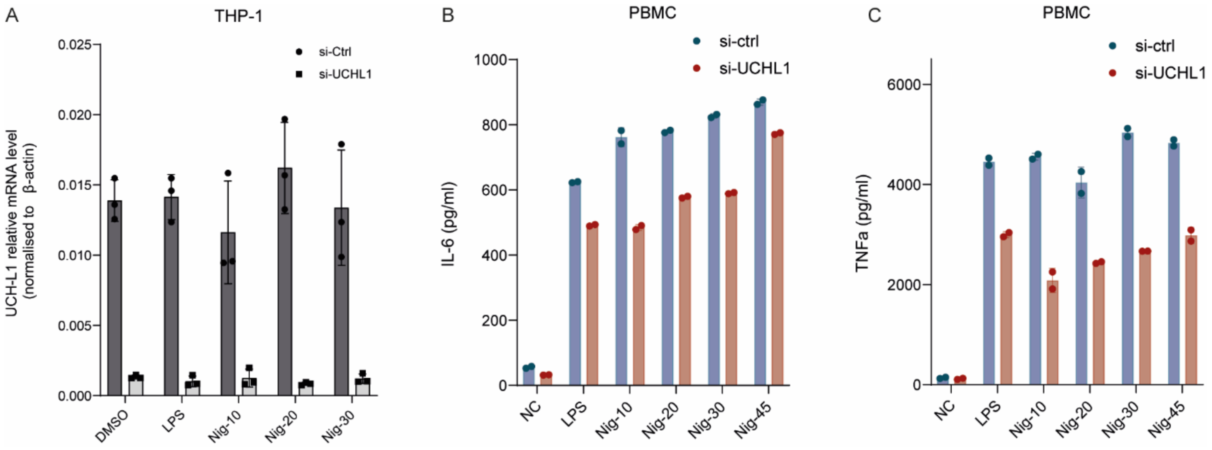

Figure S9. UCH-L1 deficiency decreases IL-6 and TNFα expression in human PBMC

(A) RT-qPCR analysis of UCH-L1 expression in THP-1 cells after transfection with either non-targeting siRNA or UCH-L1-targeted siRNA. Following differentiation with PMA, cells were primed using LPS (1 μg/mL) for 4 hours, and then treated with nigericin (10 μM) for different timepoints as indicated. (B-C) PBMCs were transfected with non-targeting control, or UCH-L1-specific siRNA, stimulated with LPS for 4 hours and nigericin for different timepoints as indicated. Production of IL-6 (B) and TNFα (C) in the supernatants from PBMCs were measured by ELISA.

Figure S10

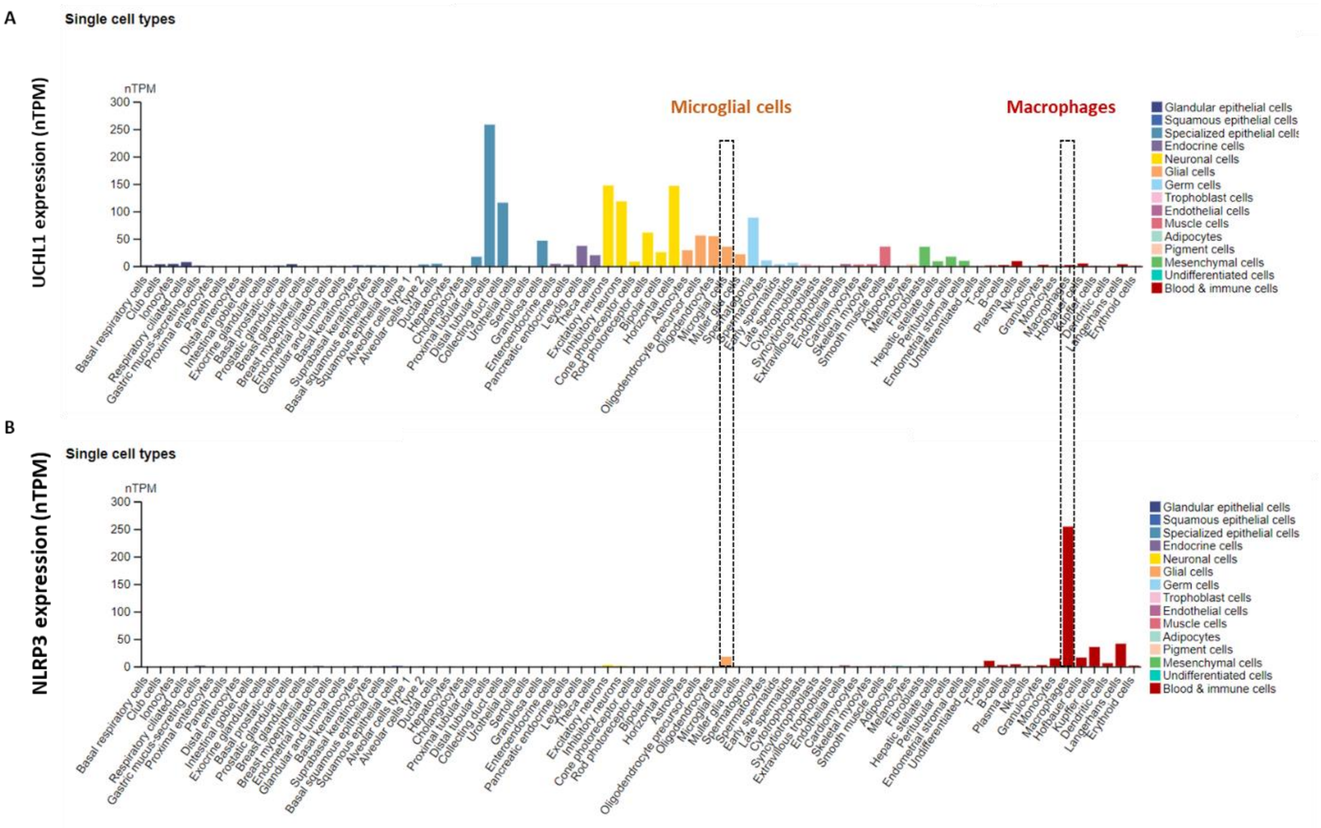

Figure S10. RNA expression level of NLRP3 and UCH-L1 in different cell types

(A,B) A summary of normalized single cell RNA expression (nTPM) in different cell lines for UCH-L1 (A) and NLRP3 (B). Color-coding represents different cell type groups consisting of cell types with functional features in common (Data were retrieved from https://www.proteinatlas.org/)

Figure S11

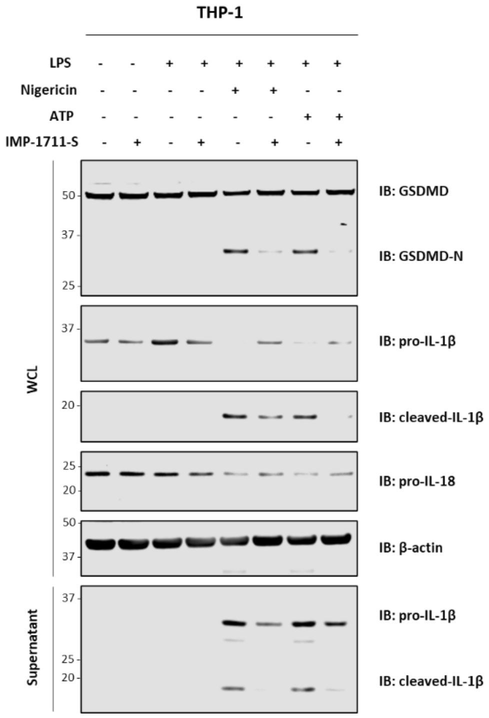

Figure S11. UCH-L1 inhibitor interferes with GSDMD cleavage

Immunoblot analysis of whole cell lysates and supernatants from THP-1 cells treated with DMSO or IMP-1711-S. THP-1 cells were differentiated with PMA and primed with LPS (1 µg/mL) for 4 hours, followed by the nigericin treatment (10 µM) for 45 minutes. DMSO or IMP-1711-S (0.3 µM) was added at the same time with LPS.

Figure S12

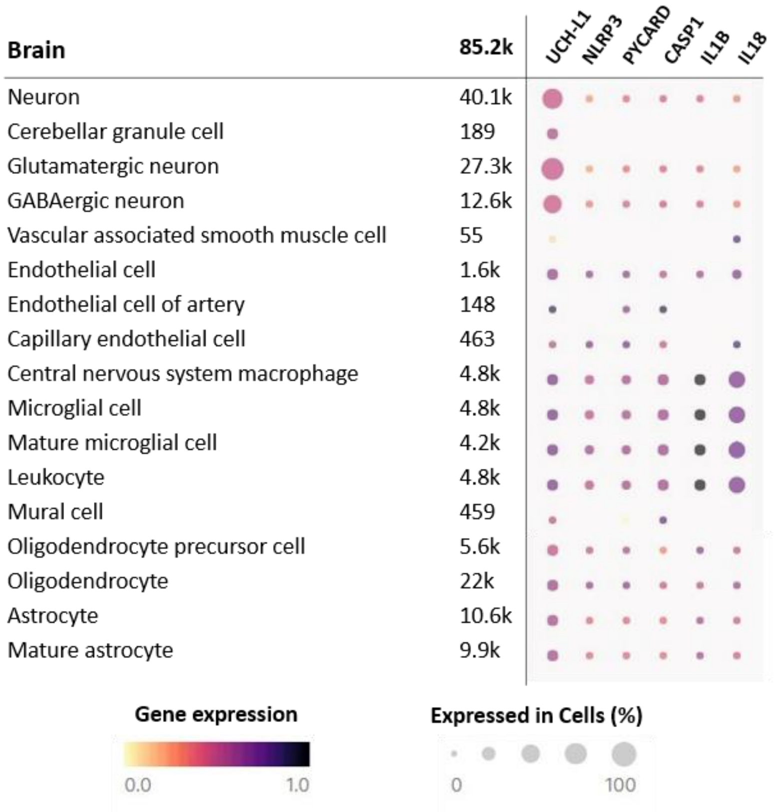

Figure S12. Single cell transcriptomics reveal the brain cell types that simultaneously express UCH-L1 and NLRP3 inflammasome components

Gene expression of UCH-L1, NLRP3, PYCARD, CASP1, IL1B, and IL18 in different brain cell types, where dot size and colour represent percentage of gene expression and the scaled expression value, respectively. Data were retrieved and visualized using CZ CellxGene Discover online portal (cellxgene.cziscience.com)[1].

Figure S13

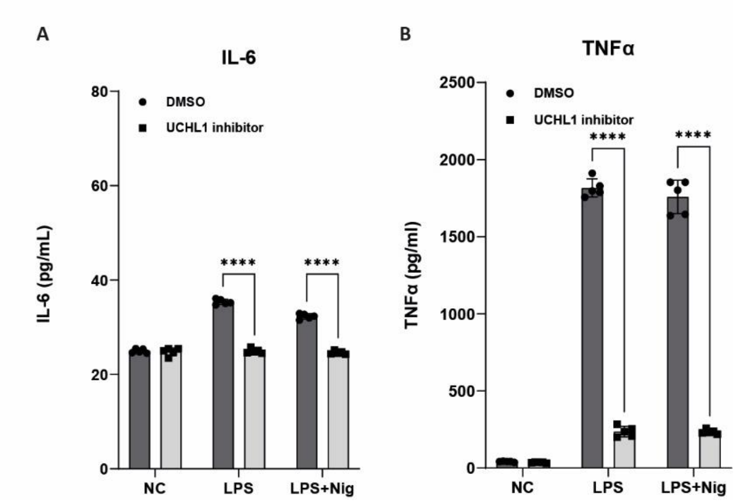

Figure S13 | UCH-L1 inhibitor diminishes IL-6 and TNFα production in THP-1 cells

(A, B) IL-6 (A) and TNFα (B) levels determined by ELISA from THP-1 cells treated with DMSO or 0.3 μM IMP-1711-S. Cells were differentiated with PMA and primed with LPS 1 μg/mL for 4 hours, followed by the treatment of nigericin (10 μM) for 45 minutes. The inhibitor or DMSO were added at the same time with LPS. Error bars show the standard deviation of the mean. ****p < 0.0001 (unpaired two-sided t-test).

Figure S14

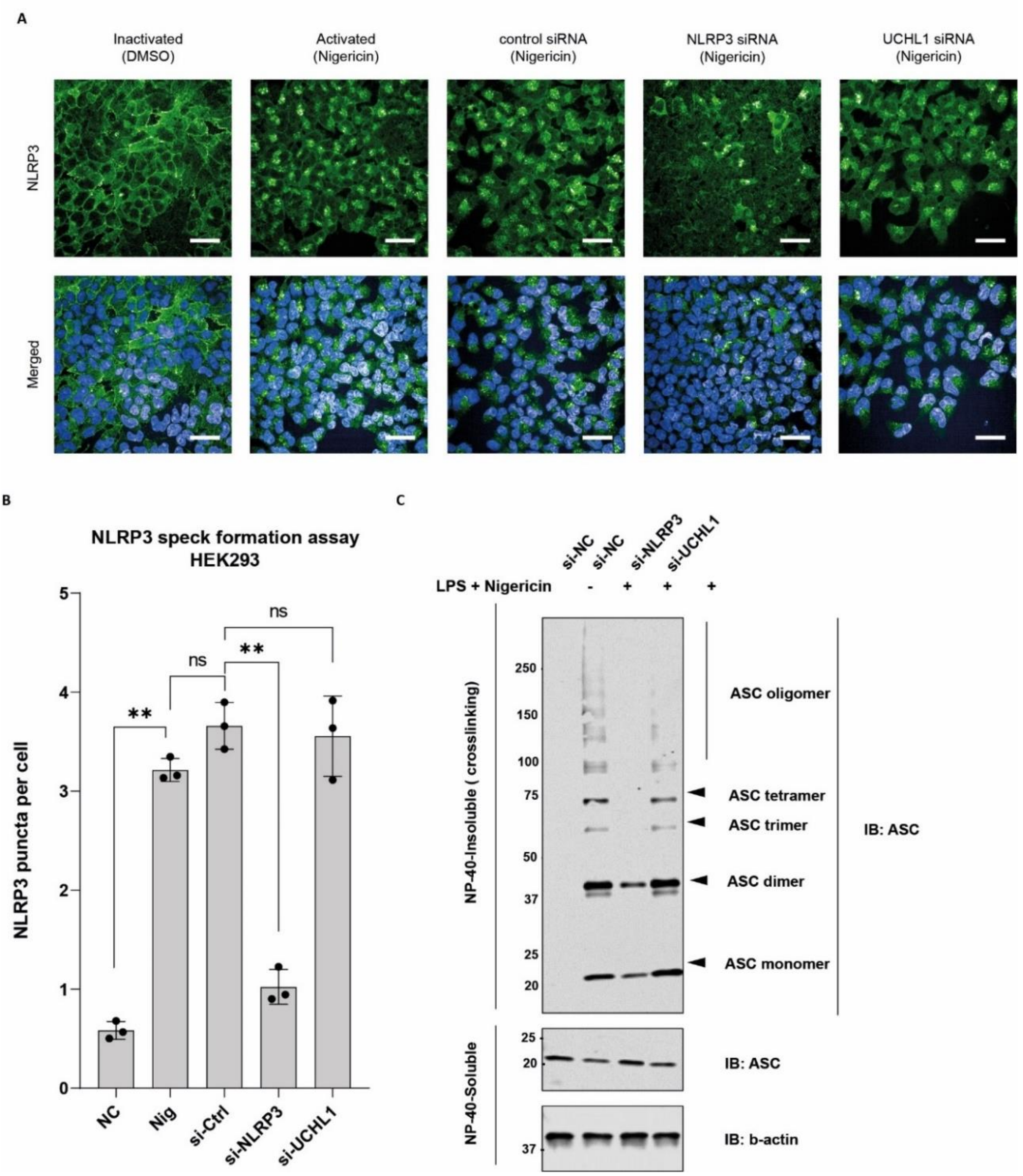

Figure S14. UCH-L1 is dispensable for NLRP3 puncta formation but partially alters ASC oligomerization

(A, B) flag-NLRP3 HEK293 stable cells were transfected with non-targeting control siRNA, NLRP3 or UCH-L1-specific siRNA. 48 hours after transfection, cells were treated with DMSO or 10 µM nigericin for 45 minutes. Subsequently, cells were stained with anti-flag antibody to measure the formation of NLRP3 puncta. (A) Representative fluorescence imaging of NLRP3 puncta using Opera Phenix Plus High-Content Screening System. Scale bars, 50 µm. (B) Quantitative analysis of the NLRP3 puncta formation (n = 3, mean ± s.d.). (C) Immunoblot analysis of ASC after DSS crosslinking in THP-1 cells transfected with non-targeting control siRNA, NLRP3 or UCH-L1-specific siRNA.

Figure S15

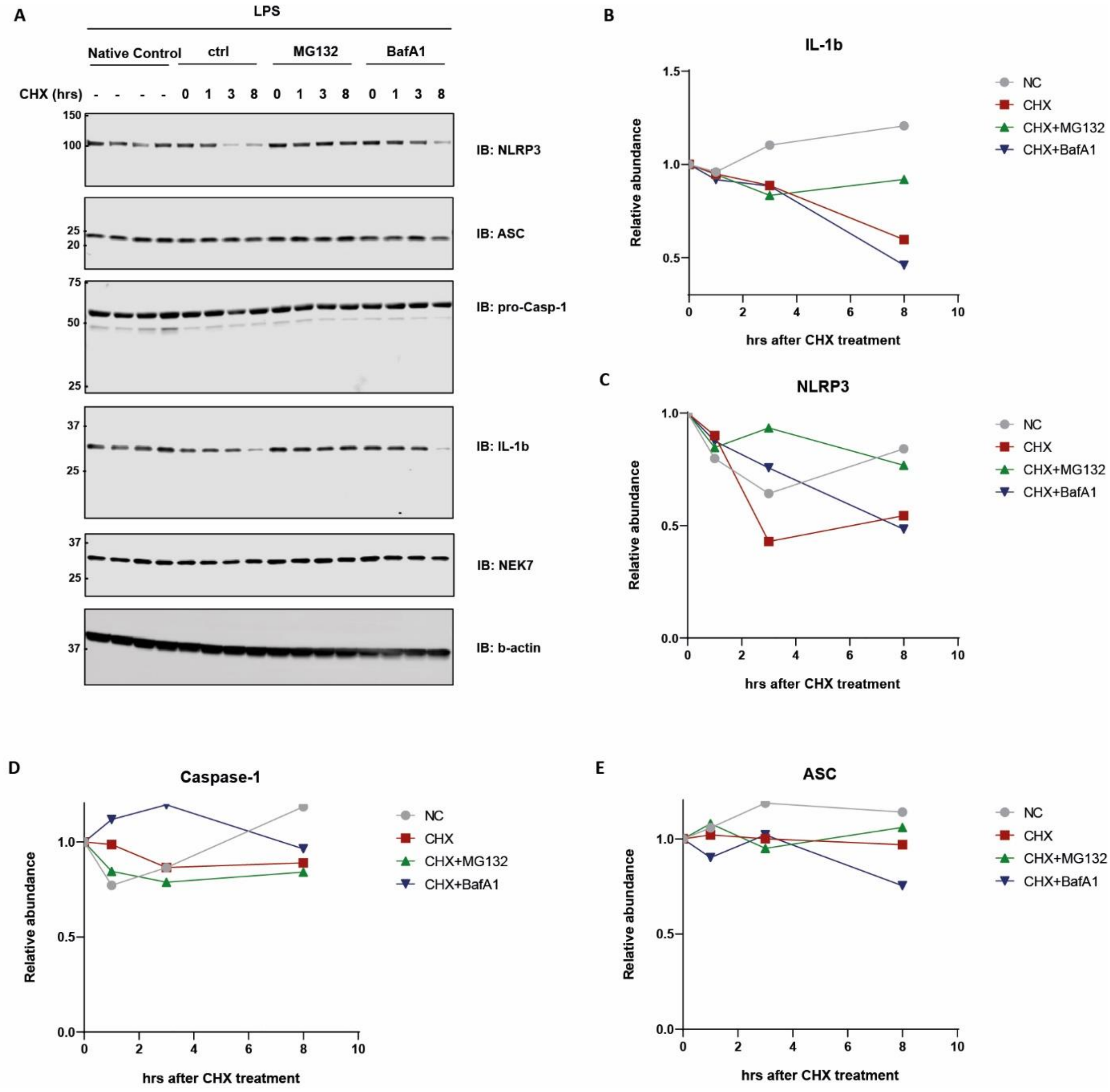

Figure S15. Protein turnover of NLRP3 and IL-1β depends on the ubiquitin proteasome pathway

(A) PMA-differentiated THP-1 cells were primed with LPS (100ng/mL) for 4 hours and followed by the treatment of MG132 (20μM) or BafA1 (300nM) as indicated, for the last 30 min. Cells were then treated with cycloheximide (50μg/mL) for 1, 3 and 8 h as indicated. Cell lysates were collected and immunoblotted for the indicated antibodies. Immunoblotting from one representative experiment of three is shown. (B-E) Quantitative analysis of the western blotting results in (A).

Figure S16

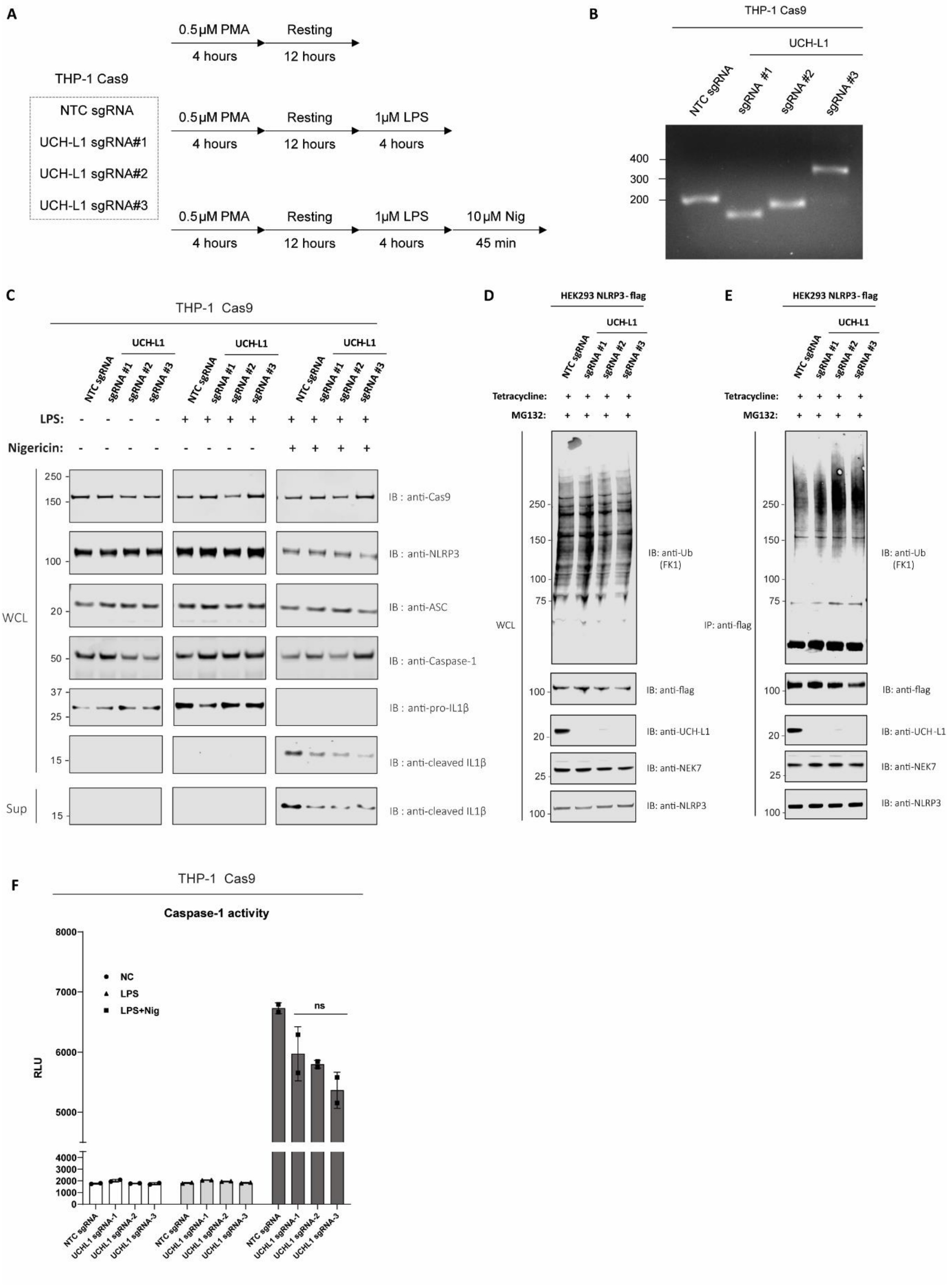

Figure S16. UCH-L1 deficiency affects IL-1β production and NLRP3 ubiquitination

(A) Experimental design and procedure. (B) 4% agarose gel electrophoresis with SYBR safe displaying PCR-amplified fragments of the UCHL1 region targeted by sgRNA1-3. Identification of the sizes of wild-type and recombinant-related bands arising from indels (insertions and deletions); high band positions relative to the wild type indicate insertions, whereas lower band positions suggest deletions. (C) THP-1 cells, transduced by lentiviruses encoding Cas9 and non-targeting control (NTC) sgRNA or sgRNA-1/2/3 targeting UCH-L1, were differentiated with PMA, primed with LPS for 4 hours and treated with nigericin for 45 minutes, as indicated. Whole cell lysates and supernatants were immunoblotted with indicated antibodies. (D-E) flag-NLRP3 HEK293 stable cell lines, transduced by lentiviruses encoding Cas9 and non-targeting control (NTC) sgRNA or sgRNA-1/2/3 targeting UCH-L1, were treated with MG132 (10 μM) for 6 hours. Whole cell lysates (D) and flag-NLRP3 immunoprecipitated in RIPA lysis buffer (E) were analysed with indicated antibodies. (F) Supernatants from (A) were collected and measured for Caspase-1 activity from 2 independent experiments. ns = not significant.

Figure S17

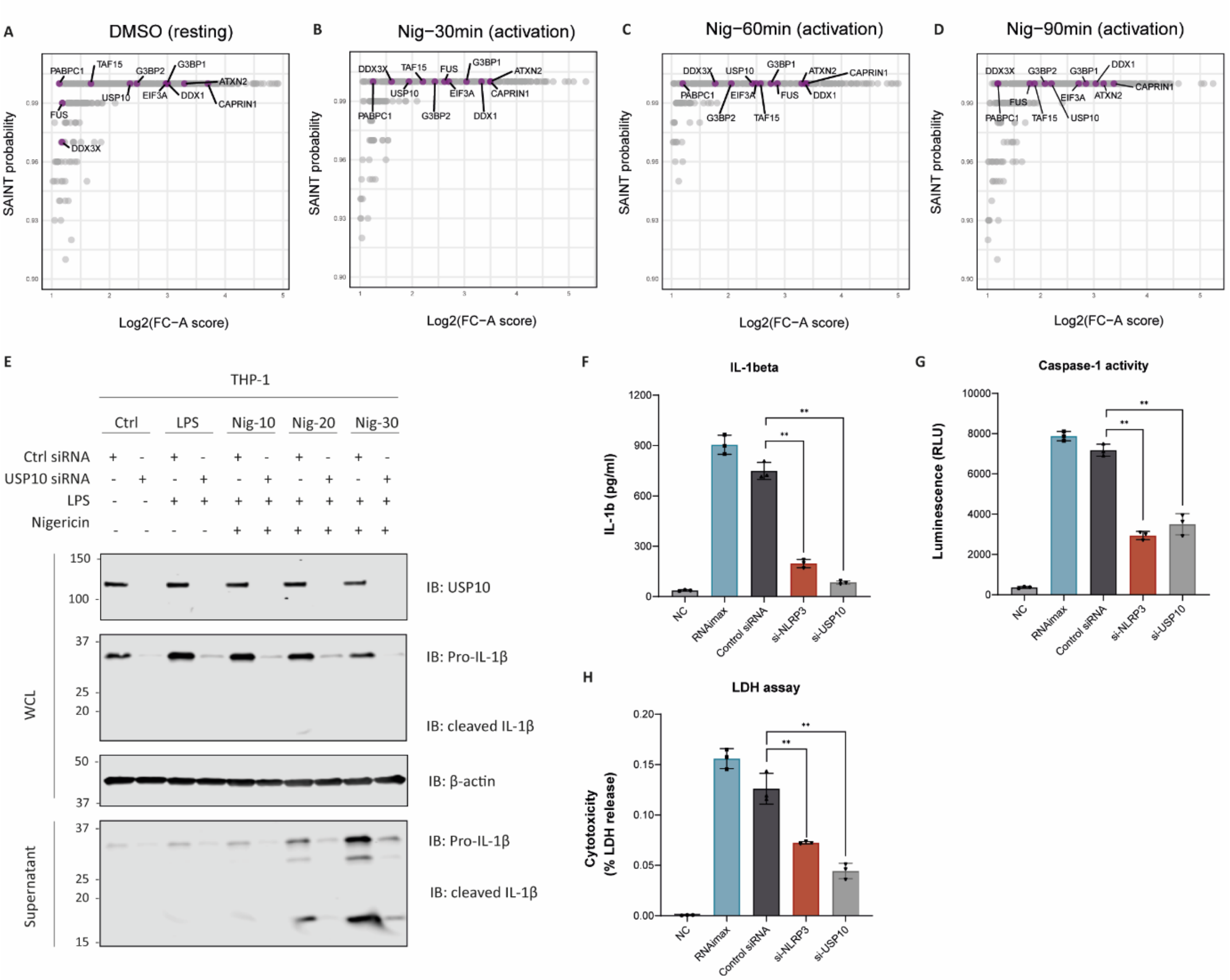

Figure S17. NLRP3-APEX2 captures stress granule components

(A-D) SAINT probability scoring of the proteomic data for NLRP3-APEX2 compared to the negative beads control. Proteins passing the cut off (SAINT probability score > 0.9 and FC-A score > 2) are considered as high confidence proximal proteins for NLRP3. The stress granule components are coloured in purple and all other proteins are shown in grey. (E) Immunoblot analysis of whole cell lysates and supernatants from THP-1 cells transfected with non-targeting control siRNA, or USP10-specific siRNA. Cells were differentiated with PMA and primed with LPS (1 µg/mL) for 4 hours, followed by the treatment of nigericin (10 µM) for different timepoints as indicated. (F-H) Supernatants were collected for the measurement of IL-1β (F), Caspase-1 activity (G) from 3 independent experiments. **$p < 0.01$, (unpaired two-sided t-test). (H) The cell viability was measured using an LDH assay.

Figure S18

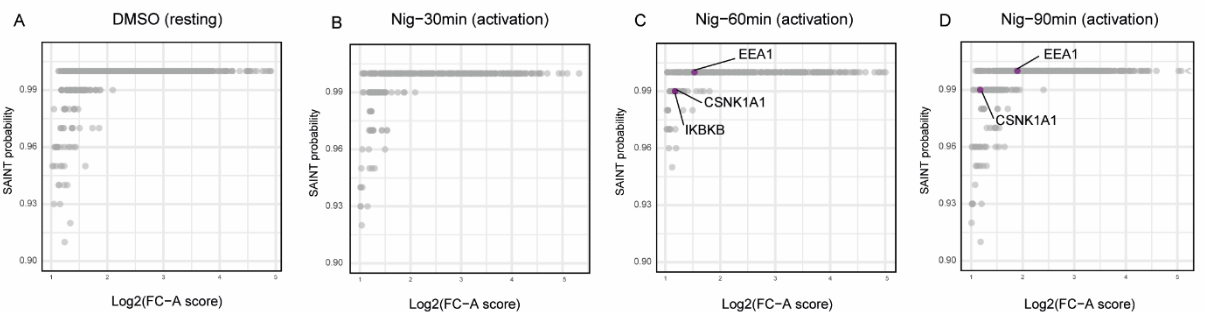

Figure S18. NLRP3-APEX2 Captures EEA1, CSNK1A1 and IKBKB upon Nigericin stimulation

(A-D) SAINT probability scoring of the proteomic data for NLRP3-APEX2 compared to the negative beads control. Proteins passing the cut off (SAINT probability score > 0.9 and FC-A score > 2) are considered as high confidence proximal proteins for NLRP3. The recently discovered NLRP3-interacting proteins (EEA1, IKKβ, and CSNK1A1) are coloured in purple and all other proteins are shown in grey.

Figure S19

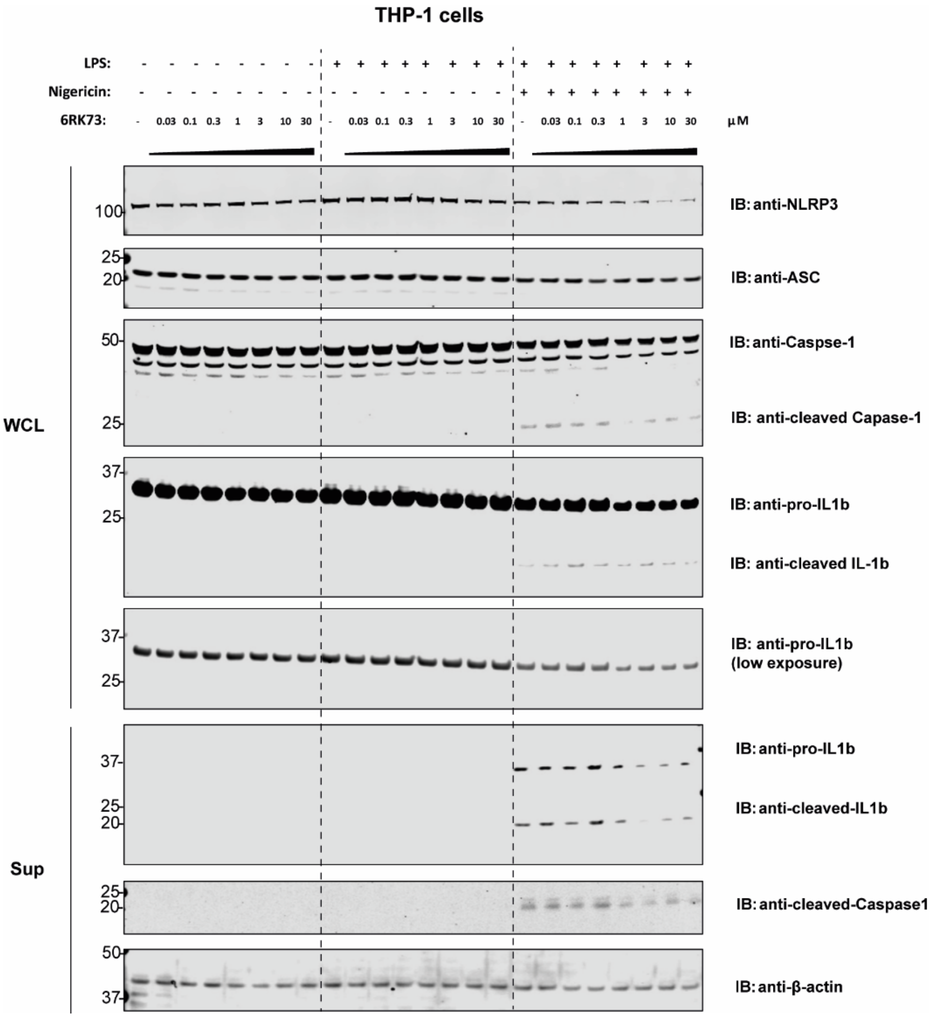

Figure S19. UCH-L1 inhibitor 6RK73 affects IL-1β production in THP-1

Immunoblot analysis of whole cell lysates and supernatants from PMA-differentiated THP-1 cells treated with DMSO or UCH-L1 inhibitor 6RK73 with indicated antibodies. THP-1 cells were differentiated with PMA and primed with LPS (1 µg/mL) for 4 hours, followed by the treatment of nigericin (10 µM) for 45 minutes. DMSO or 6RK73 (30nM, 100nM, 300nM, 1µM, 3µM, 10µM, 30µM) was added at the same time with LPS.

Figure S20

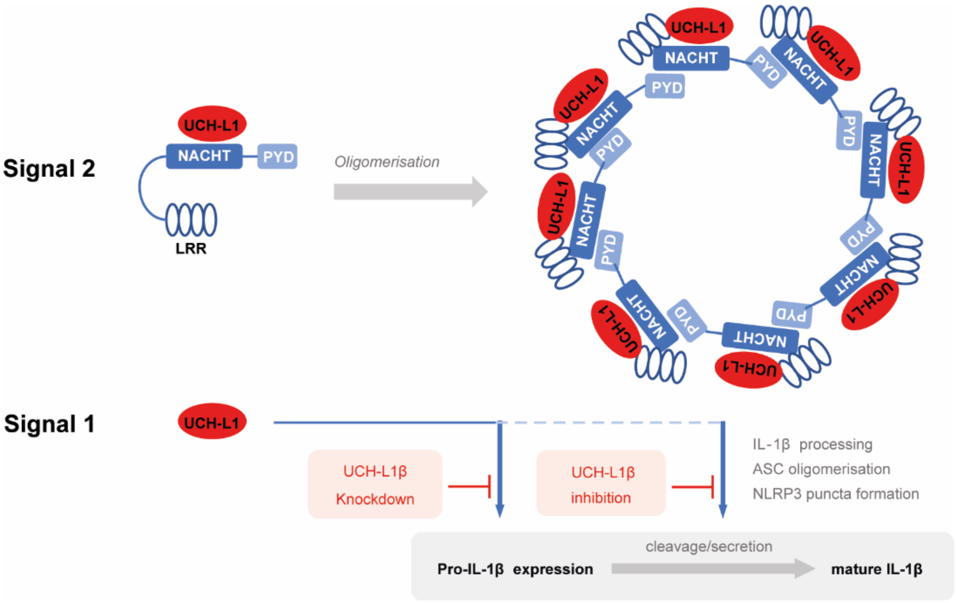

Figure S20. Model illustrating multi-functional roles of UCH-L1 in the NLRP3-mediated IL-1β expression, processing, and production

UCH-L1 was shown previously to play a role in NF-κB signalling, affecting pro-IL-1β expression [2] in the context of signal 1(priming). UCH-L1 deletion or pharmacological inhibition interferes with IL-1β production through processes of signal 2 (activation) involving ASC oligomerisation, thereby blocking IL-1β processing and secretion.

Table S2. List of the Golgi membrane proteins differentially captured by NLRP3-APEX2 during nigericin-induced inflammasome assembly

Protein IDs	Protein names	Gene names	Peptides	Unique peptides	Sequence coverage [%]
O14828	Secretory carrier-associated membrane protein 3	SCAMP3	11	11	42.1
O94979	Protein transport protein Sec31A	SEC31A	26	26	23
O95487	Protein transport protein Sec24B	SEC24B	23	23	22.7
P22059	Oxysterol-binding protein 1	OSBP	20	20	33
P53992	Protein transport protein Sec24C	SEC24C	25	24	31.9
P61019;Q8WUD1	Ras-related protein Rab-2A;Ras-related protein Rab-2B	RAB2A;RAB2B	6	6	37.7
P61106	Ras-related protein Rab-14	RAB14	12	12	65.6
Q00610	Clathrin heavy chain 1	CLTC	57	57	39.6
Q08379	Golgin subfamily A member 2	GOLGA2	22	22	28
Q10567	AP-1 complex subunit beta-1	AP1B1	19	5	21.6
Q12907	Vesicular integral-membrane protein VIP36	LMAN2	11	11	37.9
Q14789	Golgin subfamily B member 1	GOLGB1	106	106	45.4
Q15436	Protein transport protein Sec23A	SEC23A	20	17	35.7
Q15437	Protein transport protein Sec23B	SEC23B	24	21	37.2
Q86Y82	Syntaxin-12	STX12	8	8	37.7
Q8NF37	Lysophosphatidylcholine acyltransferase 1	LPCAT1	4	4	10.7
Q8TBA6	Golgin subfamily A member 5	GOLGA5	22	22	41.9
Q9BXF6	Rab11 family-interacting protein 5	RAB11FIP5	12	12	32.3
Q9H0U4;Q92928	Ras-related protein Rab-1B;Putative Ras-related protein Rab-1C	RAB1B;RAB1C	4	2	29.4
Q9NRW7	Vacuolar protein sorting-associated protein 45	VPS45	11	11	19.6
Q9NTJ5	Phosphatidylinositide phosphatase SAC1	SACM1L	11	11	19.3
Q9Y2H6	Fibronectin type-III domain-containing protein 3A	FNDC3A	7	7	8.3

Table S3. Human DUB siRNA screening in THP-1 cells

LPS

Rank	Gene	Normalized IL1b	z-score
1	TNFAIP3	2.334	3.451
2	UCHL3	2.217	2.720
3	CYLD	2.103	2.013
4	USP8	2.016	1.470
5	JOSD2	2.010	1.432
6	USP38	1.996	1.343
7	USP18	1.992	1.320
8	JOSD1	1.992	1.319
9	USP40	1.983	1.261
10	OTUD6B	1.977	1.228
11	ZRANB1	1.976	1.221
12	OTUD7A	1.967	1.162
13	OTUD7B	1.956	1.098
14	USP33	1.951	1.066
15	USP46	1.938	0.984
16	USP43	1.923	0.892
17	STAMBPL1	1.914	0.838
18	OTUB2	1.902	0.759
19	USPL1	1.900	0.746
20	OTUD5	1.898	0.736
21	USP21	1.895	0.715
22	USP48	1.893	0.704
23	USP3	1.870	0.563
24	STAMBP	1.867	0.542
25	USP45	1.863	0.518
26	USP27X	1.863	0.518
27	USP11	1.860	0.501
28	USP13	1.856	0.472
29	COPS5	1.854	0.464
30	USP6	1.848	0.422
31	MYSM1	1.845	0.403
32	USP50	1.838	0.361
33	PAN2	1.832	0.326
34	SENP2	1.832	0.323
35	USP5	1.831	0.317
36	USP24	1.831	0.315
37	PRPF8	1.821	0.259
38	UFD1L	1.816	0.226
39	USP1	1.814	0.214
40	VCPIP1	1.813	0.208
41	PSMD14	1.811	0.197
42	UBL4A	1.801	0.131
43	UCHL5	1.800	0.123

LPS + Nigericin

Rank	Gene	Normalized IL1b	z-score
1	STAMBP	3.064	2.238
2	USP39	2.966	2.015
3	ZRANB1	2.924	1.917
4	USP17L2	2.899	1.861
5	USP38	2.875	1.806
6	USP47	2.846	1.740
7	USP25	2.846	1.739
8	UBTD1	2.794	1.620
9	UCK2	2.775	1.576
10	UCHL3	2.727	1.465
11	COPS5	2.698	1.399
12	USP14	2.689	1.379
13	USP8	2.687	1.375
14	USP33	2.665	1.323
15	ATXN3	2.656	1.304
16	USP31	2.608	1.194
17	UBTD2	2.606	1.187
18	USP37	2.518	0.986
19	USP43	2.515	0.981
20	OTUD1	2.514	0.976
21	USP34	2.505	0.957
22	USP5	2.476	0.890
23	FBXO8	2.452	0.834
24	USP3	2.449	0.828
25	USP22	2.433	0.792
26	STAMBPL1	2.397	0.709
27	BRCC3	2.389	0.691
28	USP42	2.366	0.637
29	USP32	2.357	0.617
30	USP24	2.340	0.579
31	USPL1	2.320	0.532
32	YOD1	2.315	0.521
33	USP54	2.313	0.516
34	JOSD2	2.293	0.471
35	UCHL5	2.272	0.422
36	USP30	2.254	0.381
37	USP40	2.237	0.342
38	USP27X	2.233	0.332
39	USP26	2.206	0.271
40	PRPF8	2.200	0.258
41	UFD1L	2.189	0.233
42	USP35	2.184	0.220
43	OTUD4	2.153	0.150

LPS

Rank	Gene	Normalized IL1b	z-score
44	UBTD2	1.796	0.102
45	USP39	1.791	0.067
46	USP29	1.789	0.059
47	BRCC3	1.785	0.032
48	USP28	1.767	-0.077
49	USP32	1.763	-0.107
50	USP19	1.754	-0.164
51	USP7	1.752	-0.173
52	USP41	1.748	-0.200
53	MPND	1.745	-0.214
54	USP34	1.744	-0.220
55	UBTD1	1.738	-0.260
56	USP4	1.738	-0.262
57	USP10	1.736	-0.273
58	USP25	1.730	-0.307
59	USP44	1.729	-0.317
60	USP9Y	1.729	-0.317
61	FBXO8	1.722	-0.362
62	USP12	1.721	-0.368
63	YOD1	1.721	-0.369
64	USP15	1.718	-0.388
65	UBL5	1.716	-0.397
66	USP22	1.715	-0.405
67	PARP11	1.714	-0.408
68	USP30	1.713	-0.416
69	USP49	1.710	-0.436
70	UEVLD	1.710	-0.437
71	OTUB1	1.699	-0.501
72	USP17L2	1.692	-0.545
73	ATXN3	1.690	-0.557
74	UBL3	1.689	-0.563
75	USP47	1.683	-0.603
76	USP14	1.680	-0.619
77	USP42	1.680	-0.622
78	USP54	1.678	-0.634
79	FBXO7	1.672	-0.671
80	USP35	1.660	-0.743
81	USP16	1.657	-0.765
82	USP53	1.654	-0.781
83	USP2	1.654	-0.782
84	USP31	1.626	-0.956
85	BAP1	1.626	-0.959
86	USP51	1.617	-1.017
87	USP37	1.616	-1.022
88	OTUD1	1.578	-1.258

LPS + Nigericin

Rank	Gene	Normalized IL1b	z-score
44	USP15	2.146	0.133
45	USP36	2.126	0.087
46	PARP11	2.098	0.023
47	USP18	2.082	-0.014
48	USP2	2.063	-0.058
49	PAN2	1.986	-0.234
50	UBL5	1.869	-0.501
51	USP1	1.862	-0.518
52	BAP1	1.826	-0.601
53	USP48	1.822	-0.609
54	SENP2	1.814	-0.627
55	USP9Y	1.796	-0.670
56	OTUD6B	1.796	-0.670
57	FBXO7	1.792	-0.679
58	USP16	1.785	-0.694
59	USP21	1.777	-0.712
60	USP29	1.769	-0.733
61	USP50	1.753	-0.768
62	UBL4A	1.747	-0.781
63	USP46	1.741	-0.795
64	CYLD	1.739	-0.800
65	USP28	1.739	-0.801
66	USP45	1.736	-0.808
67	OTUB2	1.730	-0.820
68	MYSM1	1.726	-0.829
69	USP49	1.715	-0.855
70	USP12	1.714	-0.858
71	UBL3	1.683	-0.930
72	USP44	1.679	-0.938
73	OTUD7A	1.675	-0.948
74	TNFAIP3	1.668	-0.963
75	PSMD14	1.667	-0.965
76	USP20	1.664	-0.972
77	USP41	1.664	-0.972
78	USP4	1.664	-0.973
79	USP19	1.660	-0.981
80	MPND	1.660	-0.981
81	OTUD5	1.658	-0.987
82	USP9X	1.657	-0.989
83	USP53	1.654	-0.996
84	USP13	1.648	-1.010
85	JOSD1	1.647	-1.011
86	VCPIP1	1.640	-1.028
87	USP7	1.622	-1.068
88	UCHL1	1.617	-1.079

LPS

Rank	Gene	Normalized IL1b	z-score
89	OTUD4	1.577	-1.262
90	UBR1	1.520	-1.617
91	UCK2	1.513	-1.663
92	USP9X	1.483	-1.845
93	USP20	1.453	-2.034
94	USP36	1.447	-2.074
95	UCHL1	1.413	-2.286
96	USP26	1.316	-2.887

LPS + Nigericin

Rank	Gene	Normalized IL1b	z-score
89	UEVLD	1.617	-1.081
90	OTUB1	1.613	-1.088
91	USP11	1.605	-1.108
92	USP51	1.600	-1.118
93	OTUD7B	1.587	-1.149
94	UBR1	1.548	-1.238
95	USP6	1.547	-1.240
96	USP10	1.539	-1.259

Table S4. Analysis sequence for NLRP3 speck properties in Columbus

Steps	Building block	Method	Input	Output
1	Input image	Flatfield correction: basic Brightfield correction: yes Stack Processing: Individual plane Create Global Image: No	Channel: HOECHST 3334 Channel: Alexa 488	Output image
2	Find nuclei	Method: B Common Threshold: 0.4 Area > 30 μm2 Splitting coefficient: 7.0 Individual threshold: 0.4 Contrast > 0.1	Channel: HOECHST 3334 ROI population: None	Population: Nuclei
3	Find cytoplasm	Method: A Individual threshold: 0.15	Channel: Alexa 488 Nuclei: Nuclei	Output population: Cytoplasm
4	Find spots	Method: A Relative spot intensity > 0.18 Splitting sensitivity: 0.910 Calculate spot properties	Channel: Alexa 488 ROI population: Nuclei ROI region: Cytoplasm	Output population: NLRP3 speck
5	Define results	Standard output: spots number Formula output: spots number/nuclei number		Spots number/cell Relative spot intensity Spot Area [px2] Roundness

REFERENCE

1. Program, C.S.-C.B., Abdulla, S., Aevermann, B., Assis, P., Badajoz, S., Bell, S.M., Bezzi, E., Cakir, B., Chaffer, J., Chambers, S., et al. (2023). CZ CELL×GENE Discover: A single-cell data platform for scalable exploration, analysis and modeling of aggregated data. bioRxiv, 2023.2010.2030.563174. 10.1101/2023.10.30.563174.
2. Zhang, Z., Liu, N., Chen, X., Zhang, F., Kong, T., Tang, X., Yang, Q., Chen, W., Xiong, X., and Chen, X. (2021). UCHL1 regulates inflammation via MAPK and NF-kappaB pathways in LPS-activated macrophages. Cell Biol Int *45*, 2107-2117. 10.1002/cbin.11662.